

Draft: February 7, 2020

Wilkinson Microwave Anisotropy Probe (WMAP) Three Year Results: Implications for Cosmology

D. N. Spergel^{1,2}, R. Bean^{1,3}, O. Doré^{1,4}, M. R. Nolta^{4,5}, C. L. Bennett^{6,7}, G. Hinshaw⁶, N. Jarosik⁵, E. Komatsu^{1,8}, L. Page⁵, H. V. Peiris^{1,9,10}, L. Verde^{1,11}, C. Barnes⁵, M. Halpern¹², R. S. Hill^{6,15}, A. Kogut⁶, M. Limon⁶, S. S. Meyer⁹, N. Odegard^{6,15}, G. S. Tucker¹³, J. L. Weiland^{6,15}, E. Wollack⁶, E. L. Wright¹⁴

dns@astro.princeton.edu

ABSTRACT

A simple cosmological model with only six parameters (matter density, $\Omega_m h^2$, baryon density, $\Omega_b h^2$, Hubble Constant, H_0 , amplitude of fluctua-

¹Dept. of Astrophysical Sciences, Peyton Hall, Princeton University, Princeton, NJ 08544-1001

²Visiting Scientist, Cerro-Tololo Inter-American Observatory

³612 Space Sciences Building, Cornell University, Ithaca, NY 14853

⁴Canadian Institute for Theoretical Astrophysics, 60 St. George St, University of Toronto, Toronto, ON Canada M5S 3H8

⁵Dept. of Physics, Jadwin Hall, Princeton University, Princeton, NJ 08544-0708

⁶Code 665, NASA/Goddard Space Flight Center, Greenbelt, MD 20771

⁷Dept. of Physics & Astronomy, The Johns Hopkins University, 3400 N. Charles St., Baltimore, MD 21218-2686

⁸Department of Astronomy, University of Texas, Austin, TX

⁹Depts. of Astrophysics and Physics, KICP and EFI, University of Chicago, Chicago, IL 60637

¹⁰Hubble Fellow

¹¹Department of Physics, University of Pennsylvania, Philadelphia, PA

¹²Dept. of Physics and Astronomy, University of British Columbia, Vancouver, BC Canada V6T 1Z1

¹³Dept. of Physics, Brown University, 182 Hope St., Providence, RI 02912-1843

¹⁴UCLA Astronomy, PO Box 951562, Los Angeles, CA 90095-1562

¹⁵Science Systems and Applications, Inc. (SSAI), 10210 Greenbelt Road, Suite 600 Lanham, Maryland 20706

tions, σ_8 , optical depth, τ , and a slope for the scalar perturbation spectrum, n_s) fits not only the three year WMAP temperature and polarization data, but also small scale CMB data, light element abundances, large-scale structure observations, and the supernova luminosity/distance relationship. Using WMAP data only, the best fit values for cosmological parameters for the power-law flat Λ CDM model are $(\Omega_m h^2, \Omega_b h^2, h, n_s, \tau, \sigma_8) = (0.127^{+0.007}_{-0.013}, 0.0223^{+0.0007}_{-0.0009}, 0.73^{+0.03}_{-0.03}, 0.951^{+0.015}_{-0.019}, 0.09^{+0.03}_{-0.03}, 0.74^{+0.05}_{-0.06})$. The three year data dramatically shrinks the allowed volume in this six dimensional parameter space.

Assuming that the primordial fluctuations are adiabatic with a power law spectrum, the WMAP data *alone* require dark matter, and a spectral index that is significantly less than the Harrison-Zel'dovich-Peebles scale-invariant spectrum ($n_s = 1, r = 0$). Adding additional data sets improves the constraints on these components and the spectral slope. For power-law models, WMAP data alone puts an improved upper limit on the tensor to scalar ratio, $r_{0.002} < 0.55$ (95% CL) and the combination of WMAP and the lensing-normalized SDSS galaxy survey implies $r_{0.002} < 0.28$ (95% CL).

Models that suppress large-scale power through a running spectral index or a large-scale cut-off in the power spectrum are a better fit to the WMAP and small scale CMB data than the power-law Λ CDM model; however, the improvement in the fit to the WMAP data is only $\Delta\chi^2 = 3$ for 1 extra degree of freedom. Models with a running-spectral index are consistent with a higher amplitude of gravity waves.

In a flat universe, the combination of WMAP and the Supernova Legacy Survey (SNLS) data yields a significant constraint on the equation of state of the dark energy, $w = -0.97^{+0.07}_{-0.09}$. If we assume $w = -1$, then the deviations from the critical density, Ω_K , are small: the combination of WMAP and the SNLS data imply $\Omega_k = -0.015^{+0.020}_{-0.016}$. The combination of WMAP three year data plus the HST key project constraint on H_0 implies $\Omega_K = -0.010^{+0.016}_{-0.009}$ and $\Omega_\Lambda = 0.72 \pm 0.04$. Even if we do not include the prior that the universe is flat, by combining WMAP, large-scale structure and supernova data, we can still put a strong constraint on the dark energy equation of state, $w = -1.06^{+0.13}_{-0.08}$.

For a flat universe, the combination of WMAP and other astronomical data yield a constraint on the sum of the neutrino masses, $\sum m_\nu < 0.68$ eV (95% CL). Consistent with the predictions of simple inflationary theories, we detect no significant deviations from Gaussianity in the CMB maps using Minkowski functionals, the bispectrum, trispectrum, and a new statistic designed to detect large-scale anisotropies in the fluctuations.

Subject headings: cosmic microwave background, cosmology: observations

1. Introduction

The *power-law Λ CDM* model fits not only the Wilkinson Microwave Anisotropy Probe (WMAP) first year data, but also a wide range of astronomical data (Bennett et al. 2003; Spergel et al. 2003). In this model, the universe is spatially flat, homogeneous and isotropic on large scales. It is composed of ordinary matter, radiation, and dark matter and has a cosmological constant. The primordial fluctuations in this model are adiabatic, nearly scale-invariant Gaussian random fluctuations (Komatsu et al. 2003). Six cosmological parameters (the density of matter, the density of atoms, the expansion rate of the universe, the amplitude of the primordial fluctuations, their scale dependence and the optical depth of the universe) are enough to predict not only the statistical properties of the microwave sky, measured by WMAP at several hundred thousand points on the sky, but also the large-scale distribution of matter and galaxies, mapped by the Sloan Digital Sky Survey (SDSS) and the 2dF Galaxy Redshift Survey (2dFGRS).

With three years of integration, improved beam models, better understanding of systematic errors (Jarosik et al. 2006), temperature data (Hinshaw et al. 2006), and polarization data (Page et al. 2006), the WMAP data has significantly improved. There have also been significant improvements in other astronomical data sets: analysis of galaxy clustering in the SDSS (Tegmark et al. 2004a; Eisenstein et al. 2005) and the completion of the 2dFGRS (Cole et al. 2005); improvements in small-scale CMB measurements (Kuo et al. 2004; Readhead et al. 2004a,b; Grainge et al. 2003; Leitch et al. 2005; Piacentini et al. 2005; Montroy et al. 2005; O’Dwyer et al. 2005), much larger samples of high redshift supernova (Riess et al. 2004; Astier et al. 2005; Nobili et al. 2005; Clocchiatti et al. 2005; Krisciunas et al. 2005); and significant improvements in the lensing data (Refregier 2003; Heymans et al. 2005; Semboloni et al. 2005; Hoekstra et al. 2005).

In §2, we describe the basic analysis methodology used, with an emphasis on changes since the first year. In §3, we fit the Λ CDM model to the WMAP temperature and polarization data. With its basic parameters fixed at $z \sim 1100$, this model predicts the properties of the low redshift universe: the galaxy power spectrum, the gravitational lensing power spectrum, the Hubble constant, and the luminosity-distance relationship. In §4, we compare the predictions of this model to a host of astronomical observations. We then discuss the results of combined analysis of WMAP data, other astronomical data, and other CMB data

sets. In §5, we use the WMAP data to constrain the shape of the power spectrum. In §6, we consider the implications of the WMAP data for our understanding of inflation. In §7, we use these data sets to constrain the composition of the universe: the equation of state of the dark energy, the neutrino masses and the effective number of neutrino species. In §8, we search for non-Gaussian features in the microwave background data. The conclusions of our analysis are described in §9.

2. Methodology

The basic approach of this paper is similar to that of the first-year WMAP analysis: our goal is to find the simplest model that fits the CMB and large-scale structure data. Unless explicitly noted in §2.1, we use the methodology described in Verde et al. (2003) and applied in Spergel et al. (2003). We use Bayesian statistical techniques to explore the shape of the likelihood function, we use Monte Carlo Markov chain methods to explore the likelihood surface and we quote both our maximum likelihood parameters and the marginalized expectation value for each parameter in a given model:

$$\langle \alpha_i \rangle = \int d^N \alpha \mathcal{L}(d|\alpha) p(\alpha) \alpha_i = \frac{1}{M} \sum_{j=1}^M \alpha_i^j \quad (1)$$

where α_i^j is the value of the i -th parameter in the chain and j indexes the chain element. The number of elements (M) in the typical merged Markov Chain is at least 50,000 and is always long enough to satisfy the Gelman & Rubin (1992) convergence test with $R < 1.1$. Most merged chains have over 100,000 elements. We use a uniform prior on cosmological parameters, $p(\alpha)$ unless otherwise specified. We refer to $\langle \alpha_i \rangle$ as the best fit value for the parameter and the peak of the likelihood function as the best fit model.

The Markov chain outputs and the marginalized values of the cosmological parameters listed in Table 1 for all of the models discussed in the paper are available at <http://lambda.gsfc.nasa.gov>.

2.1. Changes in analysis techniques

We now use not only the measurements of the temperature power spectrum (TT) and the temperature polarization power spectrum (TE), but also measurements of the polarization power spectra (EE) and (BB).

At the lowest multipoles, a number of the approximations used in the first year analysis were suboptimal. Efstathiou (2004) notes that a maximum likelihood analysis is significantly

better than a quadratic estimator analysis at $\ell = 2$. Slosar et al. (2004) note that the shape of the likelihood function at $\ell = 2$ is not well approximated by the fitting function used in the first year analysis (Verde et al. 2003). More accurate treatments of the low ℓ likelihoods decrease the significance of the evidence for a running spectral index (Efstathiou 2004; Slosar et al. 2004; O’Dwyer et al. 2004). Hinshaw et al. (2006) and Page et al. (2006) describe our approach to addressing this concern: for low multipoles, we explicitly compute the likelihood function for the WMAP temperature and polarization maps. This pixel-based method is used for C_ℓ^{TT} for $2 \leq \ell \leq 12$ and polarization for $2 \leq \ell \leq 23$.

There are several improvements in our analysis of high ℓ temperature data (Hinshaw et al. 2006): better beam models, improved foreground models, and the use of maps with smaller pixels ($N_{side} = 1024$). The improved foreground model is significant at $\ell < 200$. The $N_{side} = 1024$ maps significantly reduce the effects of sub-pixel CMB fluctuations and other pixelization effects. We found that $N_{side} = 512$ maps had higher χ^2 than $N_{side} = 1024$ maps, particularly for $\ell = 600–700$, where there is significant signal-to-noise and pixelization effects are significant. Finally, an improved knowledge of the beam window functions reduces the excess variance near the first acoustic peak.

We now marginalize over the amplitude of Sunyaev-Zel’dovich (SZ) fluctuations. The expected level of SZ fluctuations (Refregier et al. 2000; Komatsu & Seljak 2001; Bond et al. 2005) is $\ell(\ell + 1)C_\ell/(2\pi) = 19 \pm 3(\mu\text{K})^2$ at $\ell = 450 – 800$ for $\Omega_m = 0.26$, $\Omega_b = 0.044$, $h = 0.72$, $n_s = 0.97$ and $\sigma_8 = 0.80$. The amplitude of SZ fluctuations is very sensitive to σ_8 (Komatsu & Kitayama 1999; Komatsu & Seljak 2001). For example at 60 GHz, $\ell(\ell + 1)C_\ell/(2\pi) = 65 \pm 15(\mu\text{K})^2$ at $\ell = 450 – 800$ for $\sigma_8 = 0.91$, which is comparable to the WMAP statistical errors at the same multipole range. Since the WMAP spectral coverage is not sufficient to be able to distinguish CMB fluctuations from SZ fluctuations (see discussion in Hinshaw et al. (2006)), we marginalize over its amplitude using the Komatsu & Seljak (2002) analytical model for the shape of the SZ fluctuations. We impose the prior that the SZ signal is between 0 and 2 times the Komatsu & Seljak (2002) value. Consistent with the analysis of Huffenberger et al. (2004), we find that the SZ contribution is not a significant contaminant to the CMB signal on the scales probed by the WMAP experiment. We report the amplitude of the SZ signal normalized to the Komatsu & Seljak (2002) predictions for the cosmological parameters listed above with $\sigma_8 = 0.80$. For the best fit ΛCDM model, $\sigma_8 = \sigma_8 = 0.744_{-0.060}^{+0.050}$ and $A_{SZ} = 0.99_{-0.99}^{+0.92}$. $A_{SZ} = 1$ implies that the SZ contribution is 8.4, 18.7 and 25.2 $(\mu\text{K})^2$ at $\ell = 220, 600$ and 1000 respectively. We discuss the effects of this marginalization in Appendix A.

We now use the CAMB code (Lewis et al. 2000) for our analysis of the WMAP power spectrum. The CAMB code is derived from CMBFAST (Zaldarriaga & Seljak 2000), but has

the advantage of running a factor of 2 faster on the Silicon Graphics, Inc. (SGI) machines used for the analysis in this paper.

2.2. Parameter choices

We consider constraints on the hot Big Bang Cosmological scenario with Gaussian, adiabatic primordial fluctuations as would arise from single field, slow-roll inflation. We do not consider the influence of isocurvature modes nor the subsequent production of fluctuations from topological defects or unstable particle decay.

We parameterize our cosmological model in terms of 15 parameters:

$$\mathbf{p} = \{\omega_b, \omega_c, \tau, \Omega_\Lambda, w, \Omega_k, f_\nu, N_\nu, \Delta_{\mathcal{R}}^2, n_s, r, dn_s/d\ln k, A_{SZ}, b_{SDSS}, z_s\} \quad (2)$$

where these parameters are defined in Table 1. For the basic power-law Λ CDM model, we use ω_b , ω_c , $\exp(-2\tau)$, Θ_s , n_s , and $C_{\ell=220}^{TT}$, as the cosmological parameters in the chain, A_{SZ} as a nuisance parameter, and assume a flat prior on these parameters. Other standard cosmological parameters (also defined in Table 1), such as σ_8 and h , are functions of these six parameters. Appendix A discusses the dependence of results on the choice of priors.

While the CMB data alone can constrain the six parameter power-law Λ CDM model, more general models, most notably those with non-flat cosmologies and with richer dark energy or matter content, have strong parameter degeneracies (see Verde et al. (2003) for further discussion). These degeneracies slow convergence as the Markov chains need to explore degenerate valleys in the likelihood surface. For each set of model and data analyzed, we use covariance matrices to calculate the steps in the Markov chain. After excising an initial burn-in phase, we take the first 4,000 elements of a preliminary chain to generate a covariance matrix from which the subsequent steps are determined.

3. Λ CDM Model: Does it still fit the data?

3.1. WMAP only

The Λ CDM model is still an excellent fit to the WMAP data. With longer integration times and smaller pixels, the errors in the temperature C_ℓ on the high ℓ multipoles have shrunk by more than a factor of three. As the data has improved, the likelihood function remains peaked around the maximum likelihood peak of the first year WMAP value. With longer integration, the most discrepant high ℓ points from the year-one data are now much

Parameter	Description	Definition
H_0	Hubble expansion factor	$H_0 = 100h \text{ Mpc}^{-1}\text{km s}^{-1}$
ω_b	Baryon density	$\omega_b = \Omega_b h^2 = \rho_b / 1.88 \times 10^{-26} \text{ kg m}^{-3}$
ω_c	Cold dark matter density	$\omega_c = \Omega_c h^2 = \rho_c / 18.8 \text{ yoctograms/ m}^{-3}$
f_ν	Massive neutrino fraction	$f_\nu = \Omega_\nu / \Omega_c$
$\sum m_\nu$	Total neutrino mass (eV)	$\sum m_\nu = 93.104 \Omega_\nu h^2$
N_ν	Effective number of relativistic neutrino species	
Ω_k	Spatial curvature	
Ω_{DE}	Dark energy density	For $w = -1$, $\Omega_\Lambda = \Omega_{DE}$
Ω_m	Matter energy density	$\Omega_m = \Omega_b + \Omega_c + \Omega_\nu$
w	Dark energy equation of state	$w = p_{DE} / \rho_{DE}$
$\Delta_{\mathcal{R}}^2$	Amplitude of curvature perturbations \mathcal{R}	$\Delta_{\mathcal{R}}^2 (k = 0.002/\text{Mpc}) \approx 29.5 \times 10^{-10} A$
A	Amplitude of density fluctuations ($k = 0.002/\text{Mpc}$)	See Spergel et al. (2003)
n_s	Scalar spectral index at $0.002/\text{Mpc}$	
α	Running in scalar spectral index	$\alpha = dn_s / dln k$ (assume constant)
r	Ratio of the amplitude of tensor fluctuations to scalar potential fluctuations at $k=0.002/\text{Mpc}$	
n_t	Tensor spectra index	Assume $n_t = -r/8$
τ	Reionization optical depth	
σ_8	Linear theory amplitude of matter fluctuations on $8h^{-1}$ Mpc	
Θ_s	Acoustic peak scale (degrees)	see Kosowsky et al. (2002)
A_{SZ}	SZ marginalization factor	see appendix A
b_{sdss}	Galaxy bias factor for SDSS sample	$b = [P_{sdss}(k, z = 0) / P(k)]^{1/2}$ (constant)
C_{220}^{TT}	Amplitude of the TT temperature power spectrum at $\ell = 220$	
z_s	Weak lensing source redshift	

Table 1: Cosmological parameters used in the analysis. <http://lambda.gsfc.nasa.gov> lists the marginalized values for these parameters for all of the models discussed in this paper.

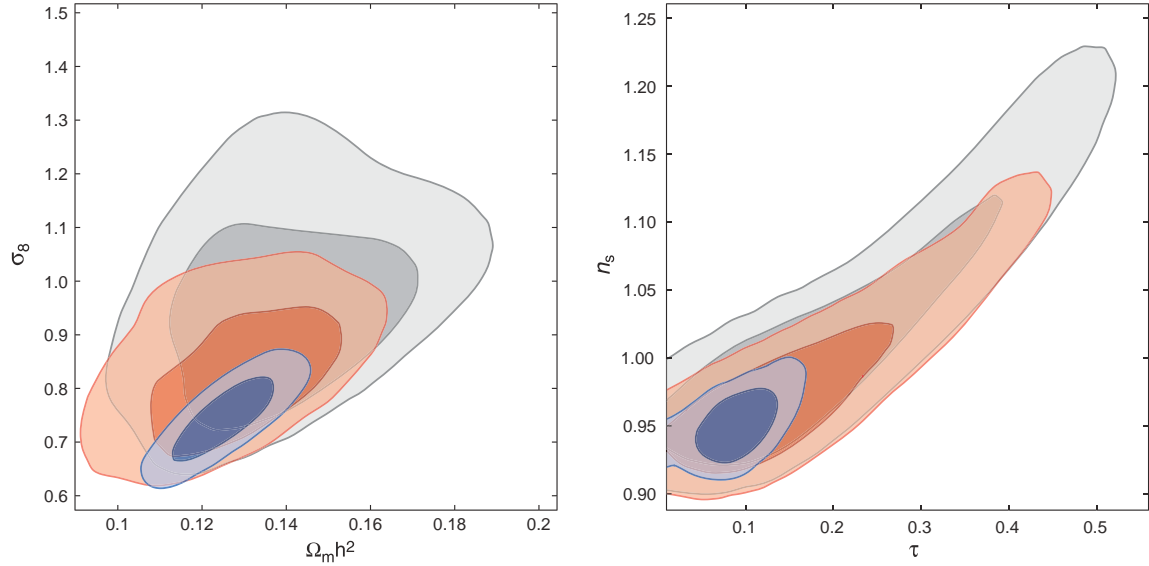


Fig. 1.— The improvement in parameter constraints for the power-law Λ CDM model (Model M5 in Table 3). The contours show the 68% and 95% joint 2-d marginalized contours for the $(\Omega_m h^2, \sigma_8)$ plane (left) and the (n_s, τ) plane (right). The black contours are for the first year WMAP data (with no prior on τ). The red contours are for the first WMAP data combined with CBI and ACBAR (WMAPext in Spergel et al. (2003)). The blue contours are for the three year WMAP data only with the SZ contribution set to 0 to maintain consistency with the first year analysis. The WMAP measurements of EE power spectrum provide a strong constraint on the value of τ . The models with no reionization ($\tau = 0$) or a scale-invariant spectrum ($n_s = 1$) are both disfavored at $\Delta\chi^2_{eff} = 8$ for 5 parameters (see Table 3). Improvements in the measurement of the amplitude of the third peak yield better constraints on $\Omega_m h^2$.

closer to the best fit model (see Figure 2). For the first year WMAP TT and TE data (Spergel et al. 2003), the reduced χ^2_{eff} was 1.09 for 893 degrees of freedom (D.O.F.) for the TT data and was 1.066 for the combined TT and TE data ($893+449=1342$ D.O.F.). For the three year data, which has much smaller error bars for $\ell > 350$, the reduced χ^2_{eff} for 982 D.O.F. ($\ell = 13 - 1000$ - 7 parameters) is now 1.068 for the TT data and 1.041 for the combined TT and TE data (1410 D.O.F., including TE $\ell = 24 - 450$), where the TE data contribution is evaluated from $\ell = 24 - 500$.

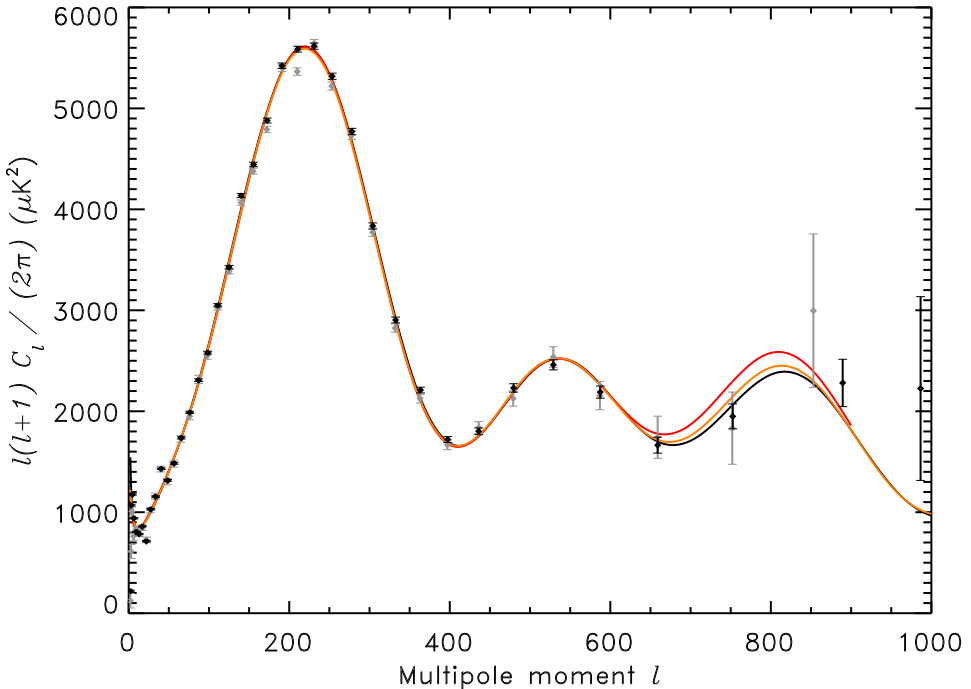


Fig. 2.— Comparison of the predictions of the different best fit models to the data. The *black* line is the angular power spectrum predicted for the best fit three-year WMAP only Λ CDM model. The *red* line is the best fit to the 1-year WMAP data. The *orange* line is the best fit to the combination of the 1-year WMAP data, CBI and ACBAR (WMAPext in Spergel et al. (2003)). The solid data points are for the 3 year data and the light gray data points are for the first year data.

For the T, Q, and U maps using the pixel based likelihood we obtain a reduced $\chi^2_{eff} = 0.981$ for 1838 pixels (corresponding to C_ℓ^{TT} for $\ell = 2 - 12$ and C_ℓ^{TE} for $\ell = 2 - 23$). The combined reduced $\chi^2_{eff} = 1.037$ for 3162 degrees of freedom for the combined fit to the TT and TE power spectrum at high ℓ and the T, Q and U maps at low ℓ .

While many of the maximum likelihood parameter values (Table 2, columns 3 and 7

and Figure 1) have not changed significantly, there has been a noticeable reduction in the marginalized value for the optical depth, τ , and a shift in the best fit value of $\Omega_m h^2$. (Each shift is slightly larger than 1σ). The addition of the EE data now eliminates a large region of parameter space with large τ and n_s that was consistent with the first year data. With only the first year data set, the likelihood surface was very flat. It covered only a ridge in $\tau - n_s$ over a region that extended from $\tau \simeq 0.07$ to nearly $\tau = 0.3$. If the optical depth of the universe were as large as $\tau = 0.3$ (a value consistent with the first year data), then the measured EE signal would have been 10 times larger than the value reported in Page et al. (2006). On the other hand, an optical depth of $\tau = 0.05$ would produce one quarter of the detected EE signal.

There has also been a significant reduction in the uncertainties in the matter density, $\Omega_m h^2$. With the first year of WMAP data, the third peak was poorly constrained (see the light gray data points in Figure 2). With three years of integration, the WMAP data better constrain the height of the third peak: WMAP is now cosmic variance limited up to $\ell = 400$ and the signal-to-noise ratio exceeds unity up to $\ell = 850$. The new best fit WMAP-only model is close to the WMAP (first year)+CBI+ACBAR model in the third peak region. As a result, the preferred value of $\Omega_m h^2$ now shifts closer to the “WMAPext” value reported in Spergel et al. (2003). Figure 1 shows the $\Omega_m h^2 - \sigma_8$ likelihood surfaces for the first year WMAP data, the first year WMAPext data and the three year WMAP data. The accurately determined peak position constrains $\Omega_m^{0.275} h$ (Page et al. 2003a), fixes the cosmological age, and determines the direction of the degeneracy surface. With 1 year data, the best fit value is $\Omega_m^{0.275} h = 0.498$. With three years of data, the best fit shifts to $0.492_{-0.017}^{+0.008}$. The lower third peak implies a smaller value of $\Omega_m h^2$ and because of the peak constraint, a lower value of Ω_m . This implies less structure growth at late times, so that the marginalized likelihood value for σ_8 in Table 2 is now noticeably smaller for the three year data, $\sigma_8 = 0.77 \pm 0.05$, than for the first-year data, 0.92 ± 0.10 .

In the first year data, we assumed that the SZ contribution to the WMAP data was negligible. Appendix A discusses the change in priors and the change in the SZ treatment and their effects on parameters: marginalizing over SZ most significantly shifts n_s and σ_8 by 1% and 3% respectively. In Table 2 and Figure 1, we assume $A_{SZ} = 0$ to make a consistent comparison between the first-year and three-year results. The first column of Table 5 list the parameters fit to the WMAP three-year data with A_{SZ} allowed to vary between 0 and 2. In the tables, the “mean” value is calculated according to equation (1) and the “Maximum Likelihood (ML)” value is the value at the peak of the likelihood function. In subsequent tables and figures, we will allow the SZ contribution to vary and quote the appropriate marginalized values. Allowing for an SZ contribution lowers the best fit primordial contribution at high ℓ , thus, the best fit models with an SZ contribution have lower n_s and

σ_8 values. In all of the Tables, we quote the 68% confidence intervals on parameters and the 95% confidence limits on bounded parameters.

Table 2: Power Law Λ CDM Model Parameters and 68% Confidence Intervals. The Three Year fits in this Table assume no SZ contribution, $A_{SZ} = 0$, to allow direct comparison with the First Year results. Fits that include SZ marginalization are given in Table 5 (first column) and represent our best estimate of these parameters.

Parameter	First Year	WMAPext	Three Year	First Year	WMAPext	Three Year
	Mean	Mean	Mean	ML	ML	ML
$100\Omega_b h^2$	$2.38^{+0.13}_{-0.12}$	$2.32^{+0.12}_{-0.11}$	2.23 ± 0.08	2.30	2.21	2.23
$\Omega_m h^2$	$0.144^{+0.016}_{-0.016}$	$0.134^{+0.006}_{-0.006}$	0.126 ± 0.009	0.145	0.138	0.128
H_0	72^{+5}_{-5}	73^{+3}_{-3}	74^{+3}_{-3}	68	71	73
τ	$0.17^{+0.08}_{-0.07}$	$0.15^{+0.07}_{-0.07}$	0.093 ± 0.029	0.10	0.10	0.092
n_s	$0.99^{+0.04}_{-0.04}$	$0.98^{+0.03}_{-0.03}$	0.961 ± 0.017	0.97	0.96	0.958
Ω_m	$0.29^{+0.07}_{-0.07}$	$0.25^{+0.03}_{-0.03}$	0.234 ± 0.035	0.32	0.27	0.24
σ_8	$0.92^{+0.1}_{-0.1}$	$0.84^{+0.06}_{-0.06}$	0.76 ± 0.05	0.88	0.82	0.77

3.2. Reionization History

Since the Kogut et al. (2003) detection of τ , the physics of reionization has been a subject of extensive theoretical study (Cen 2003; Ciardi et al. 2003; Haiman & Holder 2003; Madau et al. 2004; Oh & Haiman 2003; Ricotti & Ostriker 2004; Sokasian et al. 2004; Somerville & Livio 2003; Wyithe & Loeb 2003; Iliev et al. 2005). The EE data favors $\tau \simeq 0.1$, consistent with the predictions of a number of simulations of Λ CDM models. For example, Ciardi et al. (2003) Λ CDM simulations predict $\tau = 0.104$ for parameters consistent with the WMAP primordial power spectrum. Chiu, Fan & Ostriker (2003) found that their joint analysis of the WMAP and SDSS quasar data favored a model with $\tau_{es} = 0.11$, $\sigma_8 = 0.83$ and $n = 0.96$, very close to our new best fit values. Wyithe & Cen (2006) predict that if the product of star formation efficiency and escape fraction for Pop-III stars is comparable to that for Pop-II stars, $\tau = 0.09 - 0.12$ with reionization histories characterized by an extended ionization plateau from $z = 7 - 12$. They argue that this result holds regardless of the redshift where the intergalactic medium (IGM) becomes enriched with metals.

Measurements of the EE and TE power spectrum are a powerful probe of early star formation and an important complement to other astronomical measurements. Observations

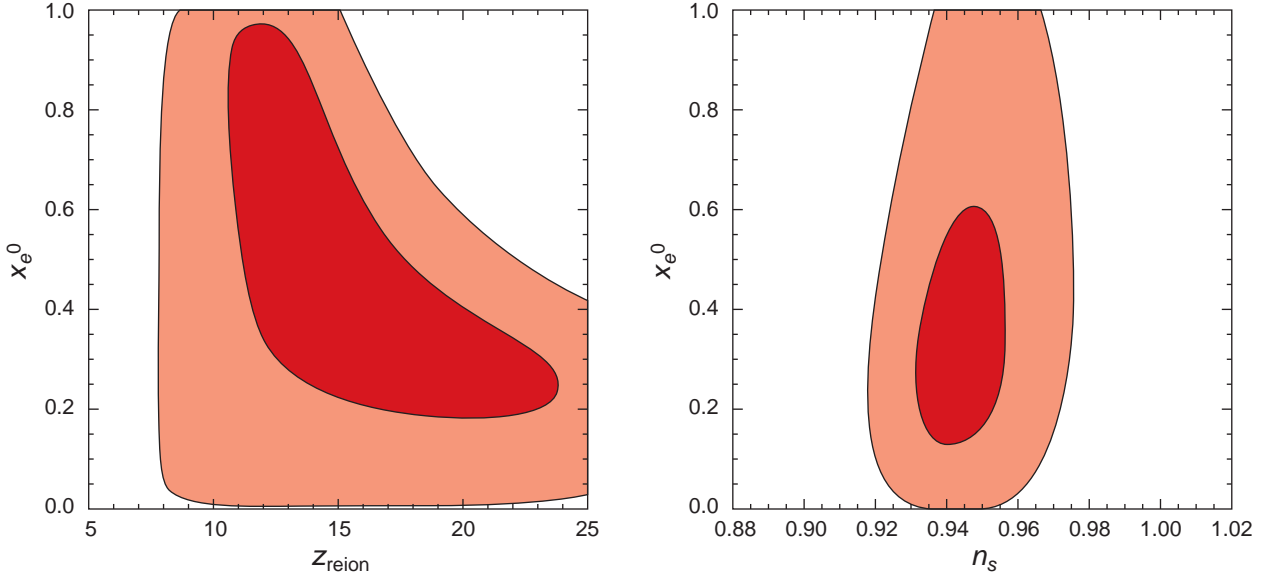


Fig. 3.— WMAP constraints on the reionization history. (Left) The 68% and 95% joint 2-d marginalized confidence level contours for $x_e^0 - z_{\text{reion}}$ for a power law Λ Cold Dark Matter (Λ CDM) model with the reionization history described by equation 3 and fit to the WMAP three year data. In equation 3 we assume that the universe was partially reionized at z_{reion} to an ionization fraction of x_e^0 , and then became fully ionized at $z = 7$. (Right) The 68% and 95% joint 2-d marginalized confidence level contours for $x_e^0 - n_s$ where τ has been fixed to be between 0.09 and 0.11. This figure shows that x_e^0 and n_s are nearly independent for a given value of τ , indicating that WMAP determinations of cosmological parameters are not affected by details of the reionization history. Note that we assume a uniform prior on z_{reion} in this calculation, which favors models with lower x_e^0 values in the right panel.

of galaxies (Malhotra & Rhoads 2004), quasars (Fan et al. 2005) and gamma ray bursts (Totani et al. 2005) imply that the universe was mostly ionized by $z = 6$. The detection of large-scale TE and EE signal (Page et al. 2006) implies that the universe was mostly reionized at even higher redshift. CMB observations have the potential to constrain some of the details of reionization, as the shape of the CMB EE power spectrum is sensitive to reionization history (Kaplinghat et al. 2003; Hu & Holder 2003). Here, we explore the ability of the current EE data to constrain reionization by postulating a two stage process as a toy model. During the first stage, the universe is partially reionized at redshift z_{reion} and complete reionization occurs at $z = 7$:

$$\begin{aligned} x_e &= 0 & z > z_{reion} \\ &= x_e^0 & z_{reion} > z > 7 \\ &= 1 & z < 7 \end{aligned} \tag{3}$$

We have modified CAMB to include this reionization history.

Figure 3 shows the likelihood surface for x_e^0 and z_{reion} . The plot shows that the data does not yet constrain x_e^0 and that the characteristic redshift of reionization is sensitive to our assumptions about reionization. If we assume that the universe is fully reionized, $x_e^0 = 1$, then the maximum likelihood peak is $z_{reion} = z_r = 10.9_{-2.3}^{+2.7}$. The maximum likelihood peak value of the cosmic age at the reionization epoch is $t_{reion} = 365 \text{ Myr}$.

Reionization alters the TT power spectrum by suppressing fluctuations on scales smaller than the horizon size at the epoch of reionization. Without strong constraints from polarization data on τ , there is a strong degeneracy between spectral index and τ in likelihood fits (Spergel et al. 2003). The polarization measurements now strongly constrain τ ; however, there is still significant uncertainty in x_e and the details of the reionization history. Fortunately, the temperature power spectrum mostly depends on the amplitude of the optical depth signal, τ , so that the other fit parameters (e.g., n_s) are insensitive to the details of the reionization history (see Figure 3). Because of this weak correlation, we will assume a simple reionization history ($x_e^0 = 1$) in all of the other analysis in this paper. Allowing for a more complex history is not likely to alter any of the conclusions of the other sections.

3.3. How Many Parameters Do We Need to Fit the WMAP Data?

In this subsection, we compare the power-law Λ CDM to other cosmological models. We consider both simpler models with fewer parameters and models with additional physics, characterized by additional parameters. We quantify the relative goodness of fit of the

models,

$$\Delta\chi_{eff}^2 \equiv -\Delta(2 \ln \mathcal{L}) = 2 \ln \mathcal{L}(\Lambda\text{CDM}) - 2 \ln \mathcal{L}(\text{model}) \quad (4)$$

A positive value for $\Delta\chi_{eff}^2$ implies the model is disfavored. A negative value means that the model is a better fit. We also characterize each model by the number of free parameters, N_{par} . There are 3162 degrees of freedom in the combination of T, Q, and U maps and high ℓ TT and TE power spectra used in the fits and 1448 independent C_l 's, so that the effective number of data degrees of freedom is between 1448 and 3162.

Table 3 shows that the power-law ΛCDM is a significantly better fit than the simpler models. If we reduce the number of parameters in the model, the cosmological fits significantly worsen:

- Cold dark matter serves as a significant forcing term that amplifies the higher acoustic oscillations. Alternative gravity models (e.g., MOND), and all baryons-only models, lack this forcing term so they predict a much lower third peak than is observed by WMAP and small scale CMB experiments (McGaugh 2004; Skordis et al. 2006). Models without dark matter (even if we allow for a cosmological constant) are very poor fits to the data.
- Positively curved models without a cosmological constant are consistent with the WMAP data alone: a model with the same six parameters and the prior that there is no dark energy, $\Omega_\Lambda = 0$, fits as well as the standard model with the flat universe prior, $\Omega_m + \Omega_\Lambda = 1$. However, if we imposed a prior that $H_0 > 40 \text{ km s}^{-1} \text{ Mpc}^{-1}$, then the WMAP data would not be consistent with $\Omega_\Lambda = 0$. Moreover, the parameters fit to the no-cosmological-constant model, ($H_0 = 30 \text{ km s}^{-1} \text{ Mpc}^{-1}$ and $\Omega_m = 1.3$) are terrible fits to a host of astronomical data: large-scale structure observations, supernova data and measurements of local dynamics. As discussed in §7.3, the combination of WMAP data and other astronomical data solidifies the evidence against these models. The detected cross-correlation between CMB fluctuations and large-scale structure provides further evidence for the existence of dark energy (see §4.1.10).
- The simple scale invariant ($n_s = 1.0$) model is no longer a good fit to the WMAP data. As discussed in the previous subsection, combining the WMAP data with other astronomical data sets further strengthens the case for $n_s < 1$.

The conclusion that the WMAP data demands the existence of dark matter and dark energy is based on the assumption that the primordial power spectrum is a power-law spectrum. By adding additional features in the primordial perturbation spectrum, these alternative models may be able to better mimic the ΛCDM model. This possibility requires further study.

The bottom half of Table 3 lists the relative improvement of the generalized models over the power-law Λ CDM. As the Table shows, the WMAP data alone does not require the existence of tensor modes, quintessence, or modifications in neutrino properties. Adding these parameters does not improve the fit. For the WMAP data, the region in likelihood space where these additional parameters are 0 is within the 1σ contour. In the §7, we consider the limits on these parameters based on WMAP data and other astronomical data sets.

If we allow for a non-flat universe, then models with small negative $i\Omega_k$ are a better fit than the power-law Λ CDM model. These models have a lower ISW signal at low l and are a better fit to the low ℓ multipoles. The best fit closed universe model has $\Omega_m = 0.415$, $\Omega_\Lambda = 0.630$ and $H_0 = 55 \text{ kms}^{-1}\text{Mpc}^{-1}$ and is a better fit to the WMAP data alone than the flat universe model ($\Delta\chi_{eff}^2 = 6$) This best fit model has a much larger SZ amplitude, $A_{SZ} = 1.4$ than expected for its small value of $\sigma_8 = 0.72$. If we had imposed the prior that the SZ signal match the KS prediction, then the expected value of A_{SZ} would be smaller and the $\Delta\chi_{eff}^2$ would drop to 2. More significantly, as discussed in §7.3, the combination of WMAP data with either SNe data, large-scale structure data or measurements of H_0 favors models with Ω_K close to 0.

In section 5, we consider several different modifications to the shape of the power spectrum. As noted in Table 3, none of the modifications lead to significant improvements in the fit. Allowing the spectral index to vary as a function of scale improves the goodness-of-fit. The low ℓ multipoles, particularly $\ell = 2$, are lower than predicted in the Λ CDM model. However, the relative improvement in fit is not large, $\Delta\chi_{eff}^2 = 3$, so the WMAP data alone do not require a running spectral index.

Measurement of the goodness of fit is a simple approach to test the needed number of parameters. These results should be confirmed by Bayesian model comparison techniques (Beltrán et al. 2005; Trotta 2005; Mukherjee et al. 2006; Bridges et al. 2005).

Table 3: Goodness of Fit, $\Delta\chi_{eff}^2 \equiv -2 \ln \mathcal{L}$, for WMAP data only relative to a Power-Law Λ CDM model. $\Delta\chi_{eff}^2 > 0$ is a worse fit to the data.

	Model	$-\Delta(2 \ln \mathcal{L})$	N_{par}
M1	Scale Invariant Fluctuations ($n_s = 1$)	8	5
M2	No Reionization ($\tau = 0$)	8	5
M3	No Dark Matter ($\Omega_c = 0, \Omega_\Lambda \neq 0$)	248	6
M4	No Cosmological Constant ($\Omega_c \neq 0, \Omega_\Lambda = 0$)	0	6
M5	Power Law ΛCDM	0	6
M6	Quintessence ($w \neq -1$)	0	7
M7	Massive Neutrino ($m_\nu > 0$)	0	7
M8	Tensor Modes ($r > 0$)	0	7
M9	Running Spectral Index ($dn_s/d \ln k \neq 0$)	-3	7
M10	Non-flat Universe ($\Omega_k \neq 0$)	-6	7
M11	Running Spectral Index & Tensor Modes	-3	8
M12	Sharp cutoff	-1	7
M13	Binned $\Delta_{\mathcal{R}}^2(k)$	-22	20

4. WMAP Λ CDM Model and Other Astronomical Data

In this paper, our approach is to show first that a wide range of astronomical data sets are consistent with the predictions of the Λ CDM model with its parameters fitted to the WMAP data (see section §4.1). We then use the external data sets to constrain extensions of the standard model.

In our analyses, we consider several different types of data sets. We consider the SDSS LRGs, the SDSS full sample and the 2dFGRS data separately, this allows a check of systematic effects. We divide the small scale CMB data sets into low frequency experiments (CBI, VSA) and high frequency experiments (BOOMERanG, ACBAR). We divide the supernova data sets into two groups as described below. The details of the data sets are also described in §4.1.

When we consider models with more parameters, there are significant degeneracies, and external data sets are essential for parameter constraints. We use this approach in §4.2 and subsequent sections.

4.1. Predictions from the WMAP Best Fit Λ CDM Model

The WMAP data alone is now able to accurately constrain the basic six parameters of the Λ CDM model. In this section, we focus on this model and begin by using only the WMAP data to fix the cosmological parameters. We then use the Markov chains (and linear theory) to predict the amplitude of fluctuations in the local universe and compare to other astronomical observations. These comparisons test the basic physical assumptions of the Λ CDM model.

4.1.1. Age of the Universe and H_0

The CMB data do not directly measure H_0 ; however, by measuring $\Omega_m H_0^2$ through the height of the peaks and the conformal distance to the surface of last scatter through the peak positions (Page et al. 2003b), the CMB data produces a determination of H_0 *if we assume the simple flat Λ CDM model*. Within the context of the basic model of adiabatic fluctuations, the CMB data provides a relatively robust determination of the age as the degeneracy in other cosmological parameters is nearly orthogonal to measurements of the age of the universe (Knox et al. 2001; Hu et al. 2001).

The WMAP Λ CDM best fit value for the age: $t_0 = 13.73^{+0.13}_{-0.17}$ Gyr, agrees with estimates

of ages based on globular clusters (Chaboyer & Krauss 2002) and white dwarfs (Hansen et al. 2004; Richer et al. 2004). Figure 4 compares the predicted evolution of $H(z)$ to the HST key project value (Freedman et al. 2001) and to values from analysis of differential ages as a function of redshift (Jimenez et al. 2003; Simon et al. 2005).

The WMAP best fit value, $H_0 = 73.4_{-3.8}^{+2.8}$ km/s/Mpc, is also consistent with HST measurements (Freedman et al. 2001), $H_0 = 72 \pm 8$ km/s/Mpc, where the error includes random and systematic uncertainties and the estimate is based on several different methods (Type Ia supernovae, Type II supernovae, surface brightness fluctuations and fundamental plane). It also agrees with detailed studies of gravitationally lensed systems such as B1608+656 (Koopmans et al. 2003), which yields 75_{-6}^{+7} km/s/Mpc and recent measurements of the Cepheid distances to nearby galaxies that host type Ia supernova (Riess et al. 2005), $H_0 = 73 \pm 4 \pm 5$ km/s/Mpc.

4.1.2. Big Bang Nucleosynthesis

Measurements of the light element abundances are among the most important tests of the standard big bang model. The WMAP estimate of the baryon abundance depends on our understanding of acoustic oscillations 300,000 years after the big bang. The BBN abundance predictions depend on our understanding of physics in the first minutes after the big bang.

Table 4 lists the primordial deuterium abundance, y_D^{FIT} , the primordial ^3He abundance, y_3 , the primordial helium abundance, Y_P , and the primordial ^7Li abundance, y_{Li} , based on analytical fits to the predicted BBN abundances (Steigman 2005) and the power-law ΛCDM 68% confidence range for the baryon/photon ratio, η_{10} . The lithium abundance is often expressed as a logarithmic abundance, $[\text{Li}]_P = 12 + \log_{10}(\text{Li}/\text{H})$.

Table 4: Primordial abundances based on using Steigman (2005) fitting formula for the ΛCDM 3-year WMAP only value for the baryon/photon ratio, $\eta_{10} = 6.0965 \pm 0.2055$.

	CMB-based BBN prediction	Observed Value
$10^5 y_D^{FIT}$	$2.58_{-0.13}^{+0.14}$	1.6 - 4.0
$10^5 y_3$	$1.05 \pm 0.03 \pm 0.03$ (syst.)	$< 1.1 \pm 0.2$
Y_P	$0.24815 \pm 0.00033 \pm 0.0006$ (syst.)	0.232 - 0.258
[Li]	2.64 ± 0.03	2.2 - 2.4

The systematic uncertainties in the helium abundances are due to the uncertainties in nuclear parameters, particularly neutron lifetime (Steigman 2005). Prior to the measure-

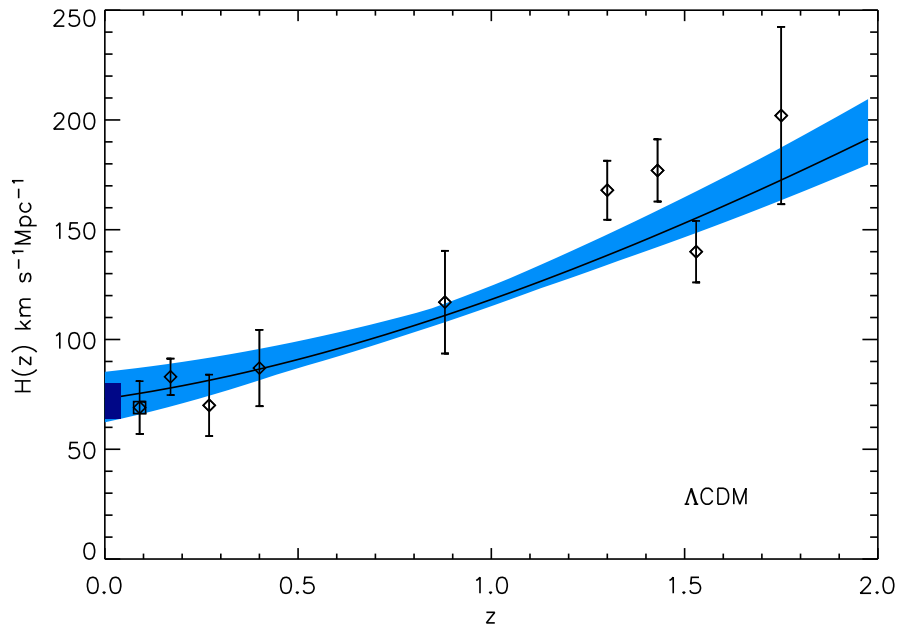


Fig. 4.— The Λ CDM model fit to the WMAP data predicts the Hubble parameter redshift relation. The blue band shows the 68% confidence interval for the Hubble parameter, H . The dark blue rectangle shows the HST key project estimate for H_0 and its uncertainties (Freedman et al. 2001). The other points are from measurements of the differential ages of galaxies, based on fits of synthetic stellar population models to galaxy spectroscopy. The squares show values from Jimenez et al. (2003) analyses of SDSS galaxies. The diamonds show values from Simon et al. (2005) analysis of a high redshift sample of red galaxies.

ments of the CMB power spectrum, uncertainties in the baryon abundance were the biggest source of uncertainty in CMB predictions. Recent measurements of the neutron lifetime (Serebrov et al. 2005) suggest that the currently accepted value, $\tau_n = 887.5$ s, should be reduced by 7.2 s, a shift of several times the reported errors. This shorter lifetime lowers the predicted best fit helium abundance, $Y_P = 0.24675$ (Mathews et al. 2005; Steigman 2005).

The deuterium abundance measurements provide the strongest test of the predicted baryon abundance. Kirkman et al. (2003) estimate a primordial deuterium abundance, $[D]/[H] = 2.78_{-0.38}^{+0.44} \times 10^{-5}$, based on five QSO absorption systems. The six systems used in the Kirkman et al. (2003) analysis show a significant range in abundances: $1.65 - 3.98 \times 10^{-5}$ and have a scatter much larger than the quoted observational errors. Recently, Crighton et al. (2004) report a deuterium abundance of $1.6_{-0.4}^{+0.5} \times 10^{-5}$ for PKS 1937-1009. Because of the large scatter, we quote the range in $[D]/[H]$ abundances in Table 4; however, note that the mean abundance is in good agreement with the CMB prediction.

It is difficult to directly measure the primordial ^3He abundance. Bania et al. (2002) argue for an upper limit on the primordial ^3He abundance of $y_3 < 1.1 \pm 0.2 \times 10^{-5}$. This limit is compatible with the BBN predictions.

Olive & Skillman (2004) have reanalyzed the estimates of primordial helium abundance based on observations of metal-poor HII regions. They conclude that the errors in the abundance are dominated by systematic errors and argue that a number of these systematic effects have not been properly included in earlier analysis. In Table 4, we quote their estimate of the allowed range of Y_P . Olive & Skillman (2004) find a representative value of 0.249 ± 0.009 for a linear fit to $[\text{O}]/[\text{H}]$ to the helium abundance, significantly above earlier estimates and consistent with WMAP-normalized BBN.

While the measured abundances of the other light elements appear to be consistent with BBN predictions, measurements of neutral lithium abundance in low metallicity stars imply values that are a factor of 2 below the BBN predictions: most recent measurements (Charbonnel & Primas 2005; Boesgaard et al. 2005) find an abundance of $[\text{Li}]_P \simeq 2.2 - 2.25$. While Meléndez & Ramírez (2004) find a higher value, $[\text{Li}]_P \simeq 2.37 \pm 0.05$, even this value is still significantly below the cosmological value, 2.64 ± 0.03 . This discrepancies could be due to systematics in the inferred lithium abundance (Steigman 2005), uncertainties in the temperature scale (Fields et al. 2005), destruction of lithium in an early generation of stars or the signature of new early universe physics (Coc et al. 2004; Richard et al. 2005; Ellis et al. 2005; Larena et al. 2005). The recent detection (Asplund et al. 2005) of ^6Li in several low metallicity stars further constrains chemical evolution models and exacerbates the tensions between the BBN predictions and observations.

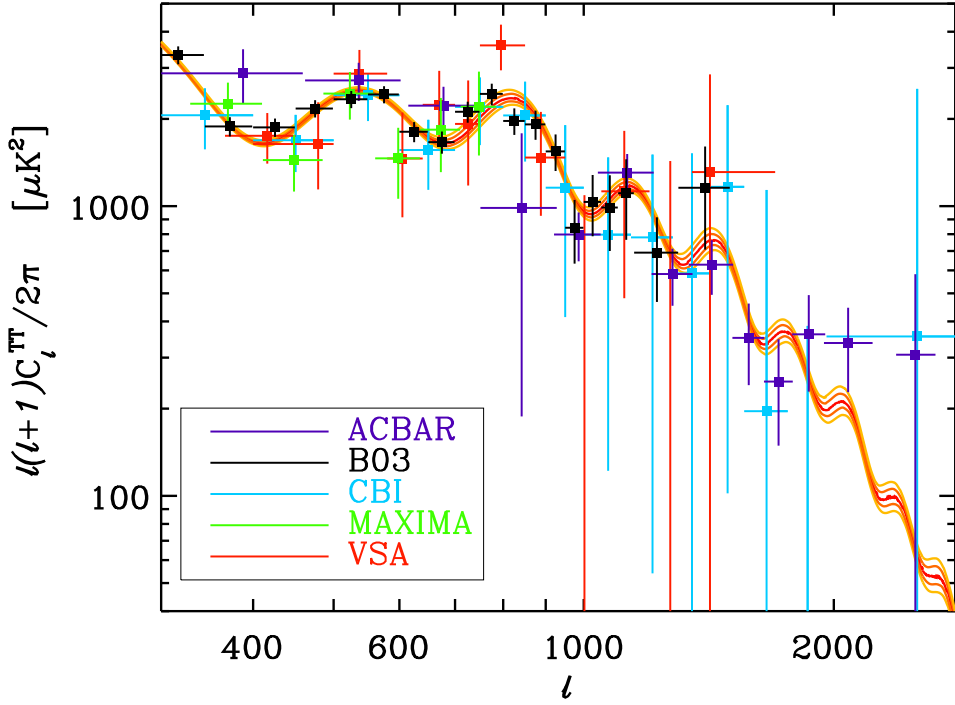


Fig. 5.— The prediction for the small-scale angular power spectrum seen by ground-based and balloon CMB experiments from the Λ CDM model fit to the WMAP data only. The colored lines show the best fit (red) and the 68% (dark orange) and 95% confidence levels (light orange) based on fits of the Λ CDM models to the WMAP data. The points in the figure show small scale CMB measurements (Grainge et al. 2003; Ruhl et al. 2003; Abroe et al. 2004; Kuo et al. 2004; Readhead et al. 2004a). The plot shows that the Λ CDM model (fit to the WMAP data alone) can accurately predict the amplitude of fluctuations on the small scales measured by ground and balloon-based experiments.

4.1.3. Small Scale CMB Measurements

With the basic parameters of the model fixed by the measurements of the first three acoustic peaks, the basic properties of the small scale CMB fluctuations are determined by the assumption of a power law for the amplitude of potential fluctuations and by the physics of Silk damping. We test these assumptions by comparing the WMAP best fit power law Λ CDM model to data from several recent small scale CMB experiments (BOOMERanG, MAXIMA, ACBAR, CBI, VSA). These experiments probe smaller angular scales than the WMAP experiment and are more sensitive to the details of recombination and the physics of acoustic oscillations. The good agreement seen in Figure (5) suggests that the standard cosmological model is accurately characterizing the basic physics at $z \simeq 1100$.

In subsequent sections, we combine WMAP with small scale experiments. We include four external CMB datasets which complement the WMAP observations at smaller scales: the Cosmic Background Imager (CBI: Mason et al. (2003); Sievers et al. (2003); Pearson et al. (2003); Readhead et al. (2004a)), the Very Small Array (VSA: Grainge et al. (2003); Slosar et al. (2003); Dickinson et al. (2004)), the Arcminute Cosmology Bolometer Array Receiver (ACBAR: Kuo et al. (2004)) and BOOMERanG (Ruhl et al. 2003; Montroy et al. 2005; Piacentini et al. 2005) We do not include results from a number of experiments that overlap in ℓ range coverage with WMAP as these experiments have non-trivial cross-correlations with WMAP that would have to be included in the analysis. We compare the angular power spectrum from based on fitting the Λ CDM model to the WMAP data alone to current experiments in Figure 5.

We do not use the small-scale polarization results for parameter determination as they do not yet noticeably improve constraints. These polarization measurements, however, already provide important tests on the basic assumptions of the model (e.g., adiabatic fluctuations and standard recombination history).

The measurements beyond the third peak improve constraints on the cosmological parameters. These observations constrict the $\{\tau, \omega_b, A_s, n_s\}$ degeneracy and provide an improved probe of a running tilt in the primordial power spectrum. In each case we only use bandpowers that do not overlap with signal-dominated WMAP observations, so that they can be treated as independent measurements.

In the subsequent sections, we perform likelihood analysis for two combinations of WMAP data with other CMB data sets: WMAP + high frequency bolometer experiments (ACBAR + BOOMERanG) and WMAP + low frequency radiometer experiments (CBI+VSA). The CBI data set is described in Readhead et al. (2004a). We use 7 bandpowers, with mean ℓ values of 948, 1066, 1211, 1355, 1482, 1692 and 1739, from the even binning

of observations rescaled to a 32 GHz Jupiter temperature of 147.3 ± 1.8 K. The rescaling reduces the calibration uncertainty to 2.6% from 10% assumed in the first year analyses; CBI beam uncertainties scale the entire power spectrum and, thus, act like a calibration error. We use a log-normal form of the likelihood as in Pearson et al. (2003). The VSA data (Dickinson et al. 2004) uses 5 bandpowers with mean ℓ -values of 894, 995, 1117, 1269 and 1407, which are calibrated to the WMAP 32 GHz Jupiter temperature measurement. The calibration uncertainty is assumed to be 3% and again we use a log-normal form of the likelihood. For ACBAR (Kuo et al. 2004), we use the same bandpowers with central ℓ values 842, 986, 1128, 1279, 1426, 1580, and 1716, and errors from the ACBAR web site¹ as in the first year analysis. We assume a calibration uncertainty of 20% in C_ℓ , and the quoted 3% beam uncertainty in Full Width Half Maximum. We use the temperature data from the 2003 flight of BOOMERanG, based on the “NA pipeline” (Jones et al. 2005) considering the 7 datapoints and covariance matrix for bins with mean ℓ values, 924, 974, 1025, 1076, 1117, 1211 and 1370.

4.1.4. Large-Scale Structure

With the WMAP polarization measurements constraining the suppression of temperature anisotropy by reionization, we now have an accurate measure of the amplitude of fluctuations at the redshift of decoupling. If the power-law Λ CDM model is an accurate description of the large-scale properties of the universe, then we can extrapolate forward the roughly 1000-fold growth in the amplitude of fluctuations due to gravitational clustering and compare the predicted amplitude of fluctuations to the large-scale structure observations. This is a powerful test of the theory as some alternative models fit the CMB data but predict significantly different galaxy power spectra (e.g., Blanchard et al. (2003)).

Using *only* the WMAP data, together with linear theory, we can predict the amplitude and shape of the matter power spectrum. The band in Figure 6 shows the 68% confidence interval for the matter power spectrum. Most of the uncertainty in the figure is due to the uncertainties in $\Omega_m h$. The points in the figure show the SDSS Galaxy power spectrum (Tegmark et al. 2004b) with the amplitude of the fluctuations normalized by the galaxy lensing measurements and the 2dFGRS data (Cole et al. 2005). The figure shows that the Λ CDM model, when normalized to observations at $z \sim 1100$, accurately predicts the large-scale properties of the matter distribution in the nearby universe. It also shows that adding the large-scale structure measurements will reduce uncertainties in cosmological parameters.

¹See <http://cosmology.berkeley.edu/group/swlh/acbar/data>

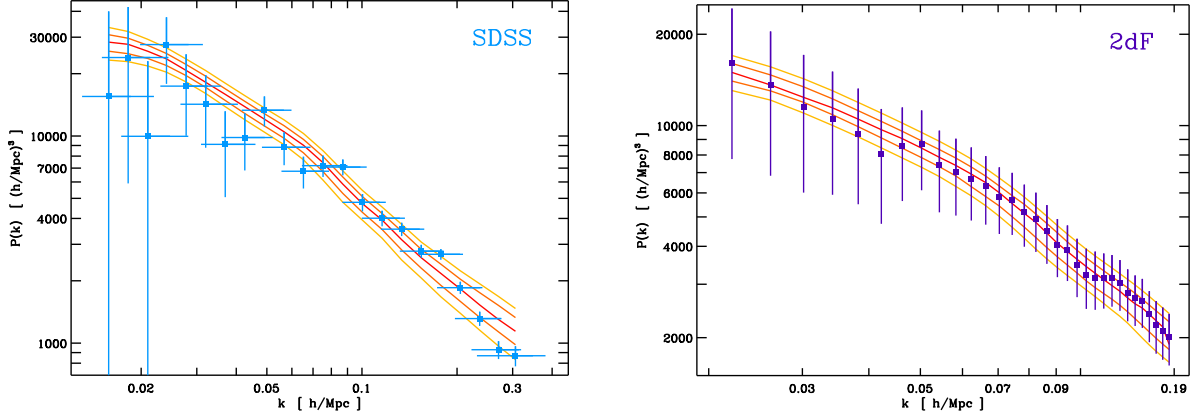


Fig. 6.— The prediction for the mass fluctuations measured by galaxy surveys from the Λ CDM model fit to the WMAP data only. (Left) The predicted power spectrum (based on the range of parameters consistent with the WMAP-only parameters) is compared to the mass power spectrum inferred from the SDSS galaxy power spectrum (Tegmark et al. 2004b) and normalized by weak lensing measurements (Seljak et al. 2005b). (Right) The predicted power spectrum is compared to the mass power spectrum inferred from the 2dFGRS galaxy power spectrum(Cole et al. 2005) with the best fit value for b_{2dFGRS} based on the fit to the WMAP model. Note that the data points shown are correlated.

When we combine WMAP with large-scale structure observations in subsequent sections, we consider the combination of WMAP with measurements of the power spectrum from the two large-scale structure surveys. Since the galaxy power spectrum does not suffer the optical depth-driven suppression in power seen in the CMB, large scale structure data gives an independent measure of the normalization of the initial power spectrum (to within the uncertainty of the galaxy biasing and redshift space distortions) and significantly truncates the $\{\tau, \omega_b, A_s, n_s\}$ degeneracy. In addition the galaxy power spectrum shape is determined by $\Omega_m h$ as opposed to the $\Omega_m h^2$ dependency of the CMB. Its inclusion therefore further helps to break the $\{\omega_m, \Omega_\Lambda, w$ or $\Omega_k\}$ degeneracy.

The 2dFGRS survey probes the universe at redshift $z \sim 0.1$ (we assume $z_{eff} = 0.17$ for the effective redshift for the survey) and probes the power spectrum on scales $0.022 \text{ hMpc}^{-1} < k < 0.19 \text{ hMpc}^{-1}$. Using the data and covariance described in Cole et al. (2005) we use 32 of the 36 bandpowers in the range $0.022 \text{ hMpc}^{-1} < k < 0.19 \text{ hMpc}^{-1}$. We correct for non-linearities and non-linear redshift space distortions using the prescription employed by the 2dF team,

$$P_{gal}^{redsh}(k) = \frac{1 + Qk^2}{1 + Ak} P_{gal}^{theory}(k) \quad (5)$$

where $P_{gal}^{redshift}$ and P_{gal}^{theory} are the redshift space and theoretical real space galaxy power spectra. with $Q = 4$. Mpc² and $A = 1.4$ Mpc. We analytically marginalize over the power spectrum amplitude, effectively applying no prior on the linear bias and on linear redshift space distortions, in contrast to our first year analyses.

The SDSS main galaxy survey measures the galaxy distribution at redshift of $z \sim 0.1$; however, as in the analysis of the SDSS team (Tegmark et al. 2004b) we assume $z_{eff} = 0.07$, and we use 14 power spectrum bandpowers between $0.016h \text{ Mpc}^{-1} < k < 0.11h \text{ Mpc}^{-1}$. We follow the approach used in the SDSS analysis in Tegmark et al. (2004a): We use the nonlinear evolution of clustering as described in Smith et al. (2003) and include a linear bias factor, b_{sdss} , and the linear redshift space distortion parameter, β .

$$P_{gal}^{redsh}(k) = (1 + \frac{2}{3}\beta + \frac{1}{5}\beta^2)P_{gal}^{theory}(k) \quad (6)$$

Following Lahav et al. (1991), we use $\beta b = d \ln \delta / d \ln a$ where $\beta \approx [\Omega_m^{4/7} + (1 + \Omega_m/2)(\Omega_\Lambda/70)]/b$. For the bias parameter, we use an estimate from weak lensing of the same SDSS galaxies used to derive the matter power spectrum to impose a Gaussian prior on the bias of $b_{SDSS} = 1.03 \pm 0.15$. This value includes a 4% calibration uncertainty in quadrature with the reported bias error.² and is a symmetrized form of the bias constraint in Table 2 of Seljak et al. (2005b). While the WMAP first year data was used in the Seljak et al. (2005b) analysis, the covariance between the data sets are small. We restrict our analysis to scales where the bias of a given galaxy population does not show significant scale dependence (Zehavi et al. 2005). Analyses that use galaxy clustering data on smaller scales require detailed modeling of non-linear dynamics and the relationship between galaxy halos and galaxy properties (see, e.g., Abazajian et al. (2005)).

The SDSS luminous red galaxy (LRG) survey uses the brightest class of galaxies in the SDSS survey (Eisenstein et al. 2005). While a much smaller galaxy sample than the main SDSS galaxy sample, it has the advantage of covering $0.72 h^{-3} \text{ Gpc}^3$ between $0.16 < z < 0.47$. Because of its large volume, this survey was able to detect the acoustic peak in the galaxy correlation, one of the distinctive predictions of the standard adiabatic cosmological model (Peebles & Yu 1970; Sunyaev & Zel'dovich 1970; Bond & Efstathiou 1984; Bond & Efstathiou 1987). We use the SDSS acoustic peak results to constrain the balance of the matter content, using the well measured combination,

$$A(z = 0.35) \equiv \sqrt{\Omega_m} E(z_{BAO})^{-1/3} \left[\frac{1}{z_{BAO}} \int_0^{z_{BAO}} \frac{dz}{E(z)} \right]^{2/3} \quad (7)$$

²M. Tegmark private communication.

where $z_{BAO} = 0.35$ and $E(z) = H(z)/H_0$. We impose a Gaussian prior of $A = 0.469 \left(\frac{n_s}{0.98}\right)^{-0.35} \pm 0.017$ based on the analysis of Eisenstein et al. (2005) .

4.1.5. Lyman α Forest

Absorption features in high redshift quasars (QSO) at around the frequency of the Lyman- α emission line are thought to be produced by regions of low-density gas at redshifts $2 < z < 4$ (Croft et al. 1998; Gnedin & Hamilton 2002). These features allow the matter distribution to be characterized on scales of $0.2 < k < 5 \text{ } h \text{ Mpc}^{-1}$ and as such extend the lever arm provided by combining large-scale structure data and CMB. These observations also probe a higher redshift range ($z \sim 2 - 3$). Thus, these observations nicely complement CMB measurements and large scale structure observations. While there has been significant progress in understanding systematics in the past few years (McDonald et al. 2005; Meiksin & White 2004), time constraints limit our ability to consider all relevant data sets.

Recent fits to the Lyman- α forest imply a higher amplitude of density fluctuations than the peak WMAP likelihood value: Jena et al. (2005) find that $\sigma_8 = 0.9, \Omega_m = 0.27, h = 0.71$ provides a good fit to the Lyman α data. Seljak et al. (2005a) combines first year WMAP data, other CMB experiments, large-scale structure and Lyman α to find: $n_s = 0.98 \pm 0.02, \sigma_8 = 0.90 \pm 0.03, h = 0.71 \pm 0.021$, and $\Omega_m = 0.281_{-0.021}^{+0.023}$. Note that if they assume $\tau = 0.09$, the best fit value drops to $\sigma_8 = 0.84$. While these models have somewhat higher amplitudes than the new best fit WMAP values, a recent analysis by Desjacques & Nusser (2005) find that the Lyman α data is consistent with σ_8 between $0.7 - 0.9$. This suggests that the Lyman α data is consistent with the new WMAP best fit values; however, further analysis is needed.

4.1.6. Galaxy Motions and Properties

Observations of galaxy peculiar velocities probe the growth rate of structure and are sensitive to the matter density and the amplitude of mass fluctuations. The Feldman et al. (2003) analysis of peculiar velocities of nearby ellipticals and spirals finds $\Omega_m = 0.30_{-0.07}^{+0.17}$ and $\sigma_8 = 1.13_{-0.23}^{+0.22}$, within 1σ of the WMAP best fit value for Ω_m and 1.5σ higher than the WMAP value for σ_8 . These estimates are based on dynamics and not sensitive to the shape of the power spectrum.

Modeled galaxy properties can be compared to the clustering properties of galaxies on smaller scales. The best fit parameters for WMAP only are consistent with the recent

Abazajian et al. (2005) analysis of the pre-three year release CMB data combined with the SDSS data. In their analysis, they fit a Halo Occupation Distribution model to the galaxy distribution so as to use the galaxy clustering data at smaller scales. Their best fit parameters ($H_0 = 70 \pm 2.6$ km/s/Mpc, $\Omega_m = 0.271 \pm 0.026$) are consistent with the results found here. Vale & Ostriker (2005) fit the observed galaxy luminosity functions with $\sigma_8 = 0.8$ and $\Omega_m = 0.25$, again consistent with the WMAP fits.

4.1.7. Weak Lensing

Over the past few years, there has been dramatic progress in using weak lensing data as a probe of mass fluctuations in the nearby universe (see Bartelmann & Schneider (2001); Van Waerbeke & Mellier (prep) for recent reviews). Lensing surveys complement CMB measurements (Contaldi et al. 2003; Tereno et al. 2005), and their dominant systematic uncertainties differ from the large-scale structure surveys.

Measurements of weak gravitational lensing, the distortion of galaxy images by the distribution of mass along the line of sight, directly probe the distribution of mass fluctuations along the line of sight (see Refregier (2003) for a recent review). Figure 7 shows that the WMAP data for the Λ CDM model predictions for σ_8 and Ω_m are lower than the amplitude found in most recent lensing surveys: Hoekstra et al. (2002) calculate $\sigma_8 = 0.94_{-0.14}^{+0.10}(\Omega_m/0.25)^{-0.52}$ (95% confidence) from the RCS survey and Van Waerbeke et al. (2005) determine $\sigma_8 = 0.91 \pm 0.08(\Omega_m/0.25)^{-0.49}$ from the VIRMOS-DESCART survey; however, Jarvis et al. (2003) find $\sigma_8 = 0.79_{-0.16}^{+0.13}(\Omega_m/0.25)^{-0.57}$ (95% confidence level) from the 75 Degree CTIO survey.

In §4.2, we use the data set provided by the first weak gravitational lensing analysis of the Canada-France-Hawaii Telescope Legacy Survey (CFHTLS)³ as conducted by Hoekstra et al. (2005) (Ho05) and Semboloni et al. (2005). Following Ho05, we use only the wide fields W1 and W3, hence a total area of 22 deg² observed in the i' band limited to a magnitude of $i' = 24.5$. We follow the same methodology as Ho05 and Tereno et al. (2005). For each given model and set of parameters, we compute the predicted shear variance at various smoothing scales, $\langle \gamma^2 \rangle$, and then evaluate its likelihood (see Ho05 equation 13).

Since we assume that the lensing data are in a noise dominated regime, we neglect the cosmological dependence of the covariance matrix. To account conservatively for a possible residual systematic contamination, we use $\langle \gamma_B^2 \rangle$ as a monitor and add it in quadrature to

³<http://www.cfht.hawaii.edu/Science/CFHTLS>

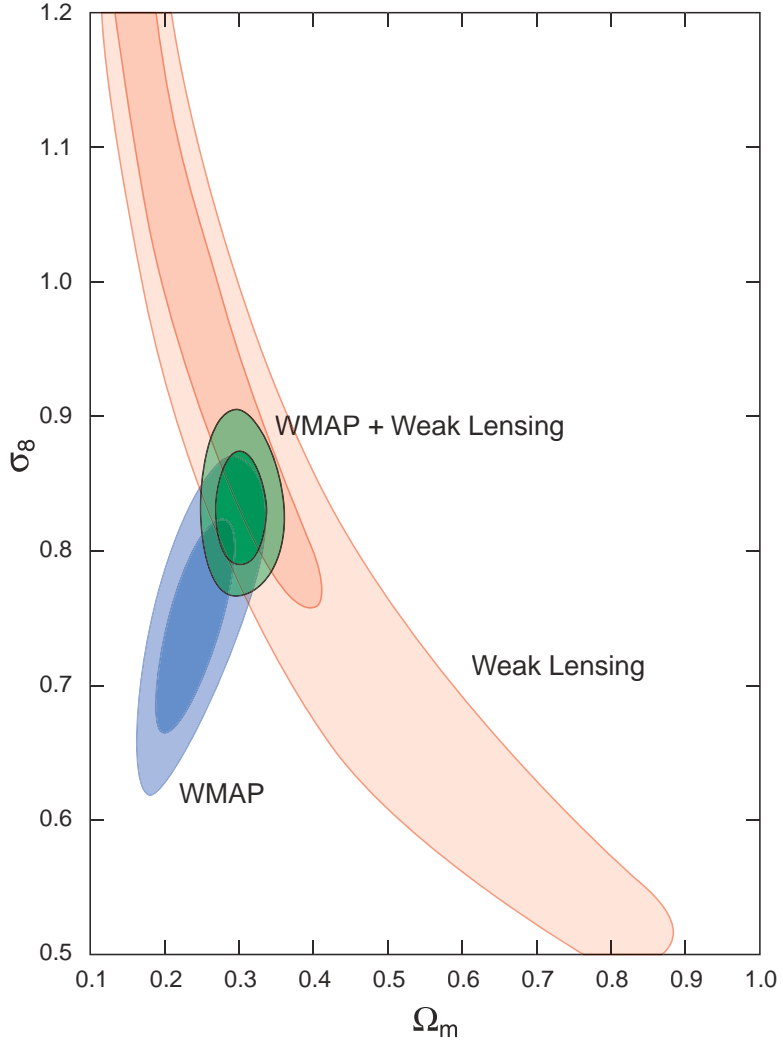


Fig. 7.— Prediction for the mass fluctuations measured by the CFTHLS weak-lensing survey from the Λ CDM model fit to the WMAP data only. The blue, red and green contours show the joint 2-d marginalized 68% and 95% confidence limits in the (σ_8, Ω_m) plane for for WMAP only, CFHTLS only and WMAP + CFHTLS, respectively, for the power law Λ CDM models. All constraints come from assuming the same priors on input parameters, with the additional marginalization over z_s in the weak lensing analysis, using a top hat prior of $0.613 < z_s < 0.721$. While lensing data favors higher values of $\sigma_8 \simeq 0.8 - 1.0$ (see §4.1.7), X-ray cluster studies favor lower values of $\sigma_8 \simeq 0.7 - 0.8$ (see §4.1.9).

the diagonal of the noise covariance matrix, as performed also by Ho05. We furthermore marginalize over the mean source redshift, z_s (defined in equation (16) of Ho05) assuming a uniform prior between 0.613 and 0.721. This marginalization is performed by including these extra parameters in the Monte Carlo Markov Chain. Our analysis differs however from the likelihood analysis of Ho05 in the choice of the transfer function. We use the Novosyadlyj et al. (1999)(NDL) CDM transfer function (with the assumptions of Tegmark et al. (2001)) rather than the Bardeen et al. (1986) (BBKS) CDM transfer function. The NDL transfer function includes more accurately baryon oscillations and neutrino effects. This modification alters the shape of the likelihood surface in the 2-dimensional (σ_8, Ω_m) likelihood space.

4.1.8. Strong Lensing

Strong lensing provides another potentially powerful probe of cosmology. The number of multiply-lensed arcs and quasars is very sensitive to the underlying cosmology. The cross-section for lensing depends on the number of systems with surface densities above the critical density, which in turn is sensitive to the angular diameter distance relation (Turner 1990). The CLASS lensing survey (Chae et al. 2002) finds that the number of lenses detected in the radio survey is consistent with a flat universe with a cosmological constant and $\Omega_m = 0.31^{+0.27}_{-0.14}$. The statistics of strong lenses in the SDSS is also consistent with the standard Λ CDM cosmology (Oguri 2004). The number and the properties of lensed arcs are also quite sensitive to cosmological parameters (but also to the details of the data analysis). Wambsganss et al. (2004) conclude that arc statistics are consistent with the concordance Λ CDM model.

Soucail et al. (2004) has used multiple lenses in Abell 2218 to provide another geometrical tests of cosmological parameters. They find that $0 < \Omega_m < 0.33$ and $w < -0.85$ for a flat universe with dark energy. This method is another independent test of the standard cosmology.

4.1.9. Clusters and the Growth of Structure

The numbers and properties of rich clusters are another tool for testing the emerging standard model. Since clusters are rare, the number of clusters as a function of redshift is a sensitive probe of cosmological parameters. Recent analyses of both optical and X-ray cluster samples yield cosmological parameters consistent with the best fit WMAP Λ CDM model (Borgani et al. 2001; Bahcall & Bode 2003; Allen et al. 2003; Vikhlinin et al. 2003;

Henry 2004). The parameters are, however, sensitive to uncertainties in the conversion between observed properties and cluster mass (Pierpaoli et al. 2003; Rasia et al. 2005).

Clusters can also be used to infer cosmological parameters through measurements of the baryon/dark matter ratio as a function of redshift (Pen 1997; Ettori et al. 2003; Allen et al. 2004). Under the assumption that the baryon/dark matter ratio is constant with redshift, the Universe is flat, and standard baryon densities, Allen et al. (2004) find $\Omega_m = 0.24 \pm 0.04$ and $w = -1.20^{+0.24}_{-0.28}$. Voevodkin & Vikhlinin (2004) determine $\sigma_8 = 0.72 \pm 0.04$ and $\Omega_m h = 0.13 \pm 0.07$ from measurements of the baryon fraction. These parameters are consistent with the values found here and in §7.1.

4.1.10. *Integrated Sachs-Wolfe (ISW) effect*

Rather than testing the Λ CDM model by comparing the matter power spectrum at different redshifts, recent analyses have tested the model by directly cross-correlating the maps. The Λ CDM model predicts a statistical correlation between the CMB temperature fluctuations and the large-scale distribution of matter (Crittenden & Turok 1996). Several groups have detected correlations between the WMAP measurements and various tracers of large-scale structure at levels consistent with the concordance Λ CDM model (Boughn & Crittenden 2004; Nolta et al. 2004; Afshordi et al. 2004; Scranton et al. 2003; Fosalba & Gaztañaga 2004; Padmanabhan et al. 2005; Corasaniti et al. 2005; Boughn & Crittenden 2005; Vielva et al. 2006). These detections are an important independent test of the effects of dark energy on the growth of structure. However, for measurements of the ISW effect, the first year WMAP data is already signal dominated on the scales probed by the ISW effect, thus, improved large-scale structure surveys are needed to improve the statistical significance of this effect (Afshordi 2004; Bean & Dore 2004; Pogosian et al. 2005).

4.1.11. *Supernova*

With the realization that their light curve shapes could be used to make SN Ia into standard candles, supernovae have become an important cosmological probe (Phillips 1993; Hamuy et al. 1996; Riess et al. 1996). They can be used to measure the luminosity distance as a function of redshift. The dimness of $z \approx 0.5$ supernova provide direct evidence for the accelerating universe (Riess et al. 1998; Schmidt et al. 1998; Perlmutter et al. 1999; Tonry et al. 2003; Knop et al. 2003; Nobili et al. 2005; Clocchiatti et al. 2005; Krisciunas et al. 2005; Astier et al. 2005). Recent HST measurements (Riess et al. 2004) trace the

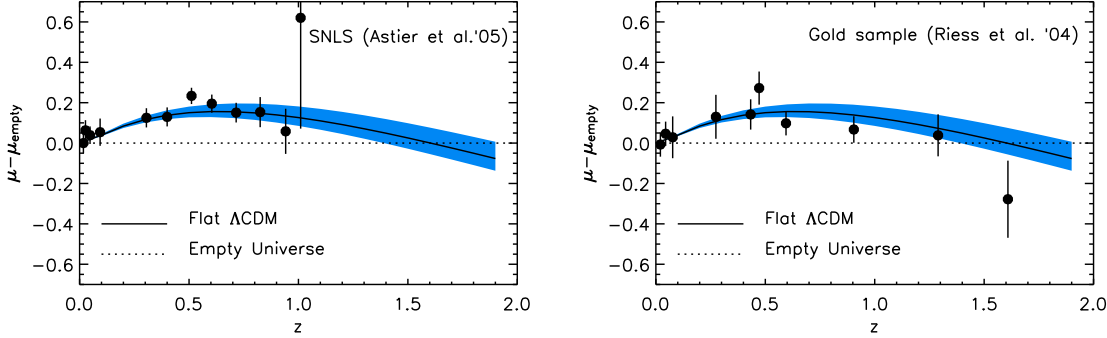


Fig. 8.— Prediction for the luminosity distance-redshift relationship measured by the supernova data from the Λ CDM model fit to the WMAP data only. The plots show the deviations of the distance measure (DM) from the empty universe model. The solid lines are the distance relationship predicted by the Λ CDM model fit to the WMAP data only. (Left) The prediction is compared to the SNLS DATA (Astier et al. 2005). (Right) The prediction is compared to the “gold” supernova data (Riess et al. 2004).

luminosity distance/redshift relation out to higher redshift and provide additional evidence for presence of dark energy. Assuming a flat Universe, the Riess et al. (2004) analysis of the supernova data alone finds that $\Omega_m = 0.29^{+0.05}_{-0.03}$ consistent with the fits to WMAP data alone (see Table 2) and to various combinations of CMB and LSS data sets (see Tables 5 and 6). Astier et al. (2005) find that $\Omega_m = 0.263^{+0.042}_{-0.042} (stat.)^{+0.032}_{-0.032} (sys.)$ from the first year supernova legacy survey.

Within the Λ CDM model, the supernovae data serve as a test of our cosmological model. Figure 8 shows the consistency between the supernova and CMB data, confirming the concordance seen in the analysis of the first-year WMAP data (Jassal et al. 2005). Using just the WMAP data and the Λ CDM model, we can predict the distance/luminosity relationship and test it with the supernova data.

In §4.2 and subsequent sections, we consider two recently published high- z supernovae datasets in combination with the WMAP CMB data, 157 supernova in the “Gold Sample” as described in Riess et al. (2004) with $0.015 < z < 1.6$ based on a combination of ground-based data and the GOODS ACS Treasury program using the Hubble Space Telescope (HST) and the second sample, 115 supernova in the range $0.015 < z < 1$ from the Supernova Legacy Survey (SNLS) (Astier et al. 2005).

Measurements of the apparent magnitude, m , and inferred absolute magnitude, M_0 , of

each SN has been used to derive the distance modulus $\mu_{obs} = m - M_0$, from which a luminosity distance is inferred, $\mu_{obs} = 5 \log[d_L(z)/\text{Mpc}] + 25$. The luminosity distance predicted from theory, μ_{th} , is compared to observations using a χ^2 analysis summing over the SN sample.

$$\chi^2 = \sum_i \frac{(\mu_{obs,i}(z_i) - \mu_{th}(z_i, M_0))^2}{\sigma_{obs,i}^2} \quad (8)$$

where the absolute magnitude, M_0 , is a “nuisance parameter”, analytically marginalized over in the likelihood analysis (Lewis & Bridle 2002), and σ_{obs} contains systematic errors related to the light curve stretch factor, K-correction, extinction and the intrinsic redshift dispersion due to SNe peculiar velocities (assumed 400 and 300 km s⁻¹ for HST/GOODS and SNLS data sets respectively).

4.2. Joint Constraints on Λ CDM Model Parameters

Table 5: Λ CDM Model: Joint Likelihoods

Parameter	WMAP Only	WMAP +CBI+VSA	WMAP+ACBAR +BOOMERanG	WMAP + 2dFGRS
$100\Omega_b h^2$	$2.233^{+0.072}_{-0.091}$	$2.212^{+0.066}_{-0.084}$	$2.231^{+0.070}_{-0.088}$	$2.223^{+0.066}_{-0.083}$
$\Omega_m h^2$	$0.1268^{+0.0072}_{-0.0095}$	$0.1233^{+0.0070}_{-0.0086}$	$0.1259^{+0.0077}_{-0.0095}$	$0.1262^{+0.0045}_{-0.0062}$
h	$0.734^{+0.028}_{-0.038}$	$0.743^{+0.027}_{-0.037}$	$0.739^{+0.028}_{-0.038}$	$0.732^{+0.018}_{-0.025}$
A	$0.801^{+0.043}_{-0.054}$	$0.796^{+0.042}_{-0.052}$	$0.798^{+0.046}_{-0.054}$	$0.799^{+0.042}_{-0.051}$
τ	$0.088^{+0.028}_{-0.034}$	$0.088^{+0.027}_{-0.033}$	$0.088^{+0.030}_{-0.033}$	$0.083^{+0.027}_{-0.031}$
n_s	$0.951^{+0.015}_{-0.019}$	$0.947^{+0.014}_{-0.017}$	$0.951^{+0.015}_{-0.020}$	$0.948^{+0.014}_{-0.018}$
σ_8	$0.744^{+0.050}_{-0.060}$	$0.722^{+0.043}_{-0.053}$	$0.739^{+0.047}_{-0.059}$	$0.737^{+0.033}_{-0.045}$
Ω_m	$0.238^{+0.030}_{-0.041}$	$0.226^{+0.026}_{-0.036}$	$0.233^{+0.029}_{-0.041}$	$0.236^{+0.016}_{-0.024}$

In the previous section, we showed that extrapolations of the power-law Λ CDM fits to the WMAP measurements to other astronomical data successfully passes a fairly stringent series of cosmological tests. Motivated by this agreement, we combine the WMAP observations with other CMB data sets and with other astronomical observations.

Table 5 and 6 show that adding external data sets has little effect on several parameters: $\Omega_b h^2$, n_s and τ . However, the various combinations do reduce the uncertainties on Ω_m and the amplitude of fluctuations. The data sets used in Table 5 favor smaller values of the matter density, higher Hubble constant values, and lower values of σ_8 . The data sets used

Table 6: Λ CDM Model

Parameter	WMAP+ SDSS	WMAP+ LRG	WMAP+ SNLS	WMAP + SN Gold	WMAP+ CFHTLS
$100\Omega_b h^2$	$2.233^{+0.062}_{-0.086}$	$2.242^{+0.062}_{-0.084}$	$2.233^{+0.069}_{-0.088}$	$2.227^{+0.065}_{-0.082}$	$2.255^{+0.062}_{-0.083}$
$\Omega_m h^2$	$0.1329^{+0.0056}_{-0.0075}$	$0.1337^{+0.0044}_{-0.0061}$	$0.1295^{+0.0056}_{-0.0072}$	$0.1349^{+0.0056}_{-0.0071}$	$0.1408^{+0.0034}_{-0.0050}$
h	$0.709^{+0.024}_{-0.032}$	$0.709^{+0.016}_{-0.023}$	$0.723^{+0.021}_{-0.030}$	$0.701^{+0.020}_{-0.026}$	$0.687^{+0.016}_{-0.024}$
A	$0.813^{+0.042}_{-0.052}$	$0.816^{+0.042}_{-0.049}$	$0.808^{+0.044}_{-0.051}$	$0.827^{+0.045}_{-0.053}$	$0.846^{+0.037}_{-0.047}$
τ	$0.079^{+0.029}_{-0.032}$	$0.082^{+0.028}_{-0.033}$	$0.085^{+0.028}_{-0.032}$	$0.079^{+0.028}_{-0.034}$	$0.088^{+0.026}_{-0.032}$
n_s	$0.948^{+0.015}_{-0.018}$	$0.951^{+0.014}_{-0.018}$	$0.950^{+0.015}_{-0.019}$	$0.946^{+0.015}_{-0.019}$	$0.953^{+0.015}_{-0.019}$
σ_8	$0.772^{+0.036}_{-0.048}$	$0.781^{+0.032}_{-0.045}$	$0.758^{+0.038}_{-0.052}$	$0.784^{+0.035}_{-0.049}$	$0.826^{+0.022}_{-0.035}$
Ω_m	$0.266^{+0.026}_{-0.036}$	$0.267^{+0.018}_{-0.025}$	$0.249^{+0.024}_{-0.031}$	$0.276^{+0.023}_{-0.031}$	$0.299^{+0.019}_{-0.025}$

in Table 6 favor higher values of Ω_m , lower Hubble constants and higher values of σ_8 . The lensing data set is most discrepant and it most strongly pulls the combined results towards higher amplitudes and higher Ω_m (see Figure 7 and 9). The overall effect of combining the data sets is shown in Figure 10.

The best fits for the data combinations shown Table 6 differ by about 1σ from the best fits for the data combinations shown in Table 5 for their predictions for the total matter density, $\Omega_m h^2$ (See Tables 5 and 6 and Figure 9). More accurate measurements of the third peak will help resolve these discrepancies.

The differences between the two sets of data may be due to statistical fluctuations. For example, the SDSS main galaxy sample power spectrum differs from the power spectrum measured from the 2dfGRS: this leads to a lower value for the Hubble constant for WMAP+SDSS data combination, $h = 0.709^{+0.024}_{-0.032}$, than for WMAP+2dFGRS, $h = 0.732^{+0.018}_{-0.025}$. Note that while the SDSS LRG data parameters values are close to those from the main SDSS catalog, they are independent determinations with mostly different systematics.

The lensing measurements are sensitive to amplitude of the local potential fluctuations, which scale roughly as $\sigma_8 \Omega_m^{0.6}$, so that lensing parameter constraints are nearly orthogonal to the CMB degeneracies (Tereno et al. 2005). The CFHTLS lensing data best fit value for $\sigma_8 \Omega_m^{0.6}$ is $1-2\sigma$ higher than the best fit three year WMAP value. As a result, the combination of CFHT and WMAP data favors a higher value of σ_8 and Ω_m and a lower value of H_0 than WMAP data alone. Appendix A shows that the amplitude of this discrepancy is somewhat sensitive to our choice of priors. Because of the small error bars in the CFHT data set

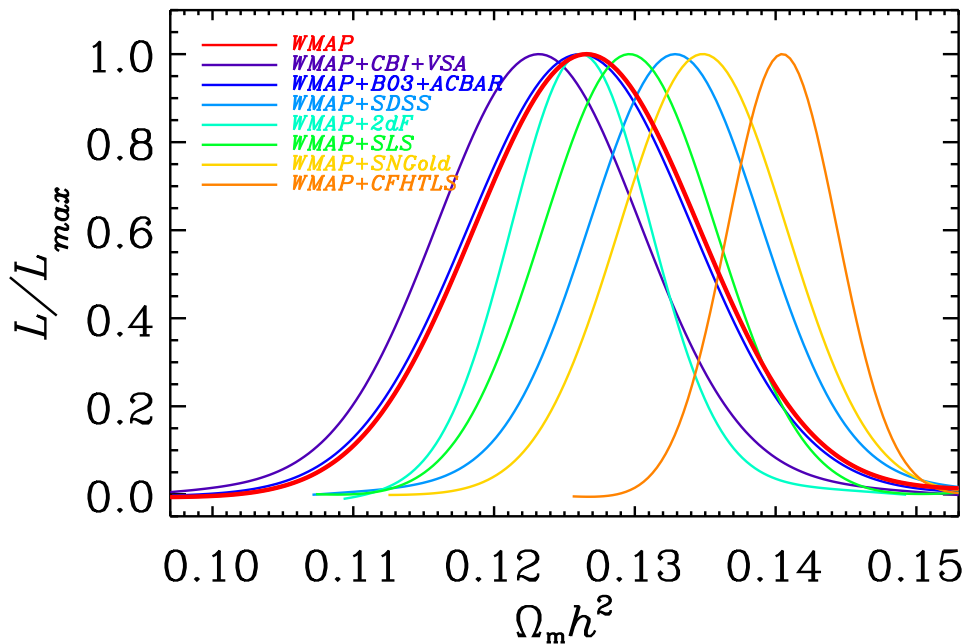


Fig. 9.— One-dimensional marginalized distribution of $\Omega_m h^2$ for WMAP, WMAP+CBI+VSA, WMAP+BOOM+ACBAR, WMAP+SDSS, WMAP+SN(SNLS), WMAP+SN(HST/GOODS), WMAP+2dFGRS and WMAP+CFHTLS for the power-law Λ CDM model.

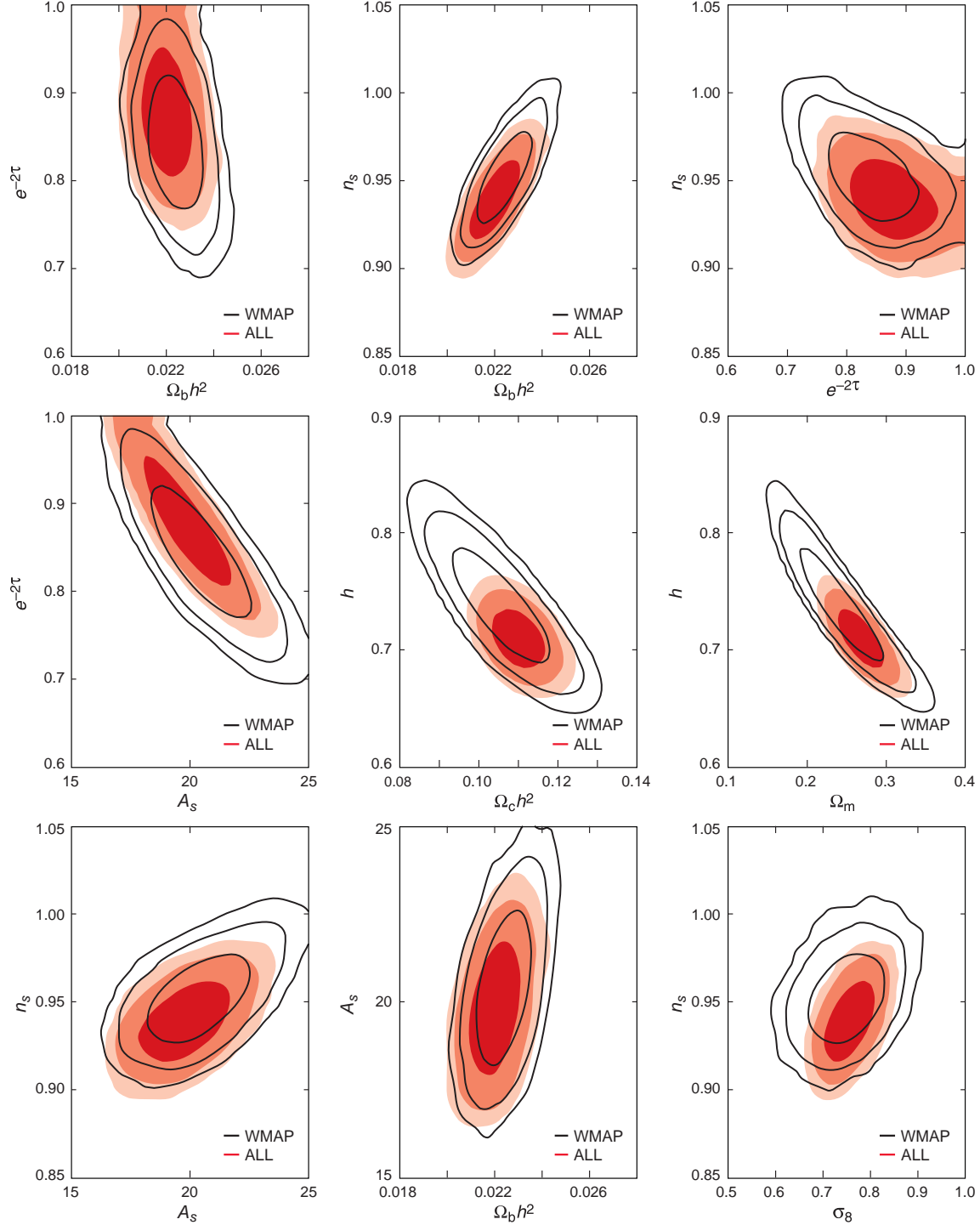


Fig. 10.— Joint two-dimensional marginalized contours (68%, and 95% confidence levels) for various combination of parameters for WMAP only (solid lines) and WMAP+2dFGRS+SDSS+ACBAR+BOOMERanG+CBI+VSA+SN(HST/GOODS)+SN(SNLS) (filled red) for the power-law Λ CDM model.

and the relatively small overlap region in parameter space, the CFHT data set has a strong influence on cosmological parameters.

For a number of models, we also compute the limits based on combining WMAP with the supernova data sets (Knop et al. 2003; Riess et al. 2004; Astier et al. 2005), the small scale CMB experiments, and the 2dFGRS and SDSS power spectrum. When used in combination with WMAP and other data sets, the lensing data tends to dominate. Because of this effect, when we do not include the lensing data in the grand combination set (WMAP+all CMB + SDSS + 2dFGRS +SN \equiv WMAP+ALL) and quote (WMAP+CFHT) as a separate column in the combined data set studies. The combined data sets place the strongest limits on cosmological parameters. Because they are based on the overlap between many likelihood functions, limits based on the WMAP+ALL data set should be treated with some caution. Figure 10 shows the 2-dimensional marginalized likelihood surface for both WMAP only and for the combination of WMAP+ALL.

5. Constraining the Shape of the Primordial Power Spectrum

5.1. Running Spectral Index Models

While the simplest inflationary models predict that the spectral index varies slowly with scale, inflationary models can produce strong scale dependent fluctuations (see e.g., Hall et al. (2004)). The first year WMAP observations provided some motivation for considering these models as the data, particularly when combined with the Lyman α forest measurements, were better fit by models with running spectral index (Spergel et al. 2003). Small scale CMB measurements (Readhead et al. 2004a) also favor running spectral index models over power law models.

Here, we consider whether a more general function for the primordial power spectrum could better fit the new WMAP data. We consider three forms for the power spectrum:

- $\Delta_{\mathcal{R}}^2(k)$ with a running spectral index: $1+d \ln \Delta_{\mathcal{R}}^2(k)/d \ln k = n(k_0) + dn_s/d \ln(k) \ln(k/k_0)$
- $\Delta_{\mathcal{R}}^2(k)$ allowed to freely vary in 15 bins in k -space, with $k_1 = 0$, $k_2 = 0.001/\text{Mpc}$, $k_{15} = 0.15/\text{Mpc}$, $k_{i+1} = 1.328k_i$ for $3 \leq i \leq 14$. $\Delta_{\mathcal{R}}^2(k)$ is given by linear interpolation within the bins and $\Delta_{\mathcal{R}}^2(k) = \Delta_{\mathcal{R}}^2(0.15/\text{Mpc})$ for $k > 0.15/\text{Mpc}$.
- $\Delta_{\mathcal{R}}^2(k)$ with a sharp k cut off at $k = k_c$,

$$\begin{aligned} \Delta_{\mathcal{R}}^2(k) &= 0, & k \leq k_c \\ &\propto \left(\frac{k}{k_0}\right)^{(n_s-1)}, & k > k_c \end{aligned} \quad (9)$$

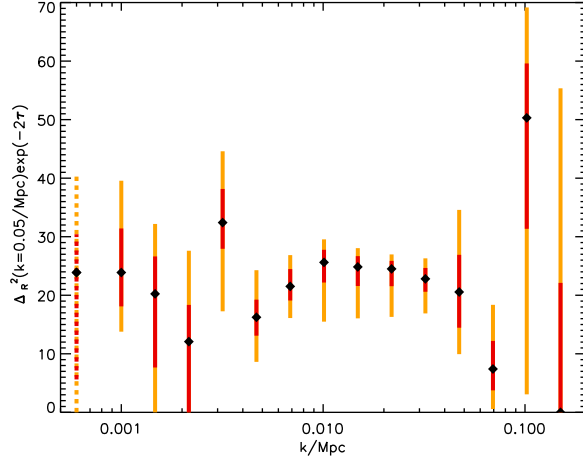


Fig. 11.— The reconstructed primordial curvature fluctuation spectrum, $\Delta_R^2(k)$, for a Λ CDM cosmology, in logarithmically spaced k bins, where k is in Mpc^{-1} . The errors show the 68% (red) and 95% (orange) constraints and the black diamonds the peak likelihood value. The dashed line show the values for $k = 0$. Consistent with the predictions of simple inflationary theories, there are no significant features in the spectrum. The data are consistent with a nearly scale-invariant spectrum.

Figure 11 shows how WMAP data alone can be used to reconstruct the primordial power spectrum as a function of scale, parameterized by logarithmically spaced bins out to $k = 0.15 \text{ Mpc}^{-1}$. Even for allowing these additional degrees of freedom, the data prefer a nearly featureless power-law power spectrum. Mukherjee & Wang (2003), Bridle et al. (2003) and Kogo et al. (2004) reach similar conclusions using different inversion methods with the first year WMAP data.

The deviation of the primordial power spectrum from a simple power law can be most simply characterized by a sharp cut-off in the primordial spectrum. Analysis of this model finds that putting in a cut off of $k_c \sim 3 \times 10^{-4}/\text{Mpc}$ improves the fit by $\Delta\chi^2 = 1.2$, not enough to justify a radical change in the primordial spectrum.

Table 3 demonstrates that, while models with reduced large scale power provide slightly improved fits to the CMB data, the improvements in fit are not such that they signal these additional parameters are required.

5.2. External Data Sets and the Running Spectral Index

Our measurements of running is slightly improved by including the small scale experiments. For models with only scalar fluctuations, the marginalized value for the derivative of the spectral index is $dn_s/d\ln k = -0.055^{+0.029}_{-0.035}$ for WMAP only, $dn_s/d\ln k = -0.066^{+0.026}_{-0.032}$ for the WMAP+CBI+VSA data and $dn_s/d\ln k = -0.058^{+0.027}_{-0.035}$ for WMAP+BOOM+ACBAR. For models with tensors, $dn_s/d\ln k = -0.102^{+0.050}_{-0.043}$ for WMAP only, $dn_s/d\ln k = -0.095^{+0.041}_{-0.037}$ for WMAP+CBI+VSA, and $dn_s/d\ln k = -0.087^{+0.041}_{-0.037}$ for WMAP+BOOM+ACBAR. As Figure 12 shows, models with negative running of the spectral indices allow large tensor amplitudes; thus, if we marginalize over r with a flat prior, these models favor a more negative running.

Figure 13 shows that both the power law Λ CDM model and the running spectral index model fit the CMB data. At present, the small scale data do not yet clearly distinguish the two models.

A large absolute value of the running spectral index would be problematic for most inflationary models, so that confirmation of this suggestive trend is important for our understanding of early universe physics. Additional WMAP data and upcoming small-scale CMB experiments will test the significance of this deviation from scale invariance. Figure 12 shows that the data favor a large running spectral index; however, the evidence is not yet compelling. By contrast, the large scale data sets do not strengthen the case for a running spectral index, nor do they strongly constrain the index. The constraints for the WMAP+lensing and WMAP+2dFGRS are similar to the WMAP+SDSS constraints shown in Figure 12. The large-scale data sets probe similar physical scales to the WMAP experiment.

5.3. Is the Power Spectrum Featureless?

Since inflation magnifies fluctuations that were once on sub-Planckian scales to scales of the observable horizon, trans-Planckian physics could potentially leave its imprint on the CMB sky. Over the past few years, there has been significant interest in the possibility of detecting the signature of trans-Planckian physics in the angular power spectrum. Several studies (Martin & Brandenberger 2001; Danielsson 2002; Easther et al. 2002; Bergström & Danielsson 2002; Kaloper et al. 2002; Martin & Brandenberger 2003; Martin & Ringeval 2004; Burgess et al. 2003; Okamoto& Lim 2003) have discussed the possible form and the expected amplitude of the trans-Planckian effects which might modify the spectrum coming from slow roll inflation. The scalar and tensor power spectra resulting from power law (PL)

slow roll inflation can be written in the terms of Hubble Flow parameters (Schwarz et al. 2001; Leach et al. 2002; Leach & Liddle 2003; Schwarz & Terrero-Escalante 2004):

$$\Delta_{\mathcal{R},PL}^2(k) = A_s \left(1 - 2(C+1)\epsilon_1 - C\epsilon_2 - (2\epsilon_1 + \epsilon_2) \ln \left(\frac{k}{k_0} \right) \right) \quad (10)$$

Here, ϵ_1 and ϵ_2 are slow roll parameters (Leach & Liddle 2003). After the release of the WMAP data, Martin & Ringeval (2004) considered a primordial power spectrum of a slightly modified form to account for additional trans-Planckian (TP) features,

$$\begin{aligned} \Delta_{\mathcal{R},TP}^2(k) &= \Delta_{\mathcal{R},PL}^2(k) [1 - 2|x|\sigma_0 \cos \theta(k)] - A_s |x|\sigma_0 \pi (2\epsilon_1 + \epsilon_2) \sin \theta(k) \\ \text{with, } \theta(k) &= \frac{1}{|x|\sigma_0} \left(1 + \epsilon_1 + \epsilon_1 \ln \left(\frac{k}{k_0} \right) \right). \end{aligned} \quad (11)$$

Here $\sigma_0 \equiv Hl_c/2\pi$ is determined by the Hubble parameter during inflation, H , and the characteristic length scale for the trans-Planckian manifestation l_c , and $|x|\sigma_0$ characterizes the amplitude of the trans-Planckian corrections to the fiducial spectrum. Martin & Ringeval (2004) report that the χ^2 for such a model could give an improvement of 15 over the power law inflationary models for an additional 2 degrees of freedom with the first year WMAP data. With three years of data, many of the glitches and bites having disappeared, the best fit trans-Planckian models of the form in equation (11) reduce the effective χ^2 by only 4 in comparison to power law inflation, a far less significant effect.

The effect of the trans-Planckian corrections can be highly model dependent (See Easther et al. (2005a) and Easther et al. (2005b) for discussions). As an alternative, we consider forms that are more general as a way of looking for oscillatory signals:

$$\Delta_{\mathcal{R},TP}^2(k) = \Delta_{\mathcal{R},PL}^2(k) [1 + \epsilon_{TP} \cos \theta(k)] \quad (12)$$

where $\theta = v \frac{k}{k_0} + \phi$ or $\theta = v \ln \left(\frac{k}{k_0} \right) + \phi$. In these models, there are three new parameters: the amplitude, ϵ_{TP} , the frequency, v , and the phase, ϕ .

Assuming the Λ CDM model, we fit these three parameters to the data and find reductions of 5 and 9.5 in the overall and TT χ_{eff}^2 . As in the Martin and Ringeval model, the improvements in the χ_{eff}^2 are driven by improvements in the fit around $\ell \sim 30 - 100$ and the first peak.

6. WMAP + Inflation

The inflationary paradigm (Guth 1981; Sato 1981; Linde 1982; Albrecht & Steinhardt 1982; Linde 1983) explains the homogeneity, isotropy and flatness of the universe by positing

an early epoch of accelerated expansion (see also Starobinsky (1980)). This accelerated period of expansion also generated superhorizon fluctuations (Guth & Pi 1982; Starobinsky 1982; Mukhanov & Chibisov 1981; Hawking 1982; Bardeen et al. 1983). In the simplest inflationary models, these fluctuations are Gaussian, random phase fluctuations with a nearly scale invariant spectrum of fluctuations.

The detailed predictions of inflationary models depend on the properties of the inflaton potential (see Linde (2005) and Lyth & Riotto (1999) for recent reviews). Simple inflationary models predict that the slope of the primordial power spectrum, n_s , differs from 1 and also predict the existence of a nearly scale-invariant spectrum of gravitational waves. In this section, we compare the simplest inflationary models to the WMAP three year data and to other cosmological data sets. We characterize these models by seven basic parameters (the six basic parameters of the Λ CDM model plus one additional parameter, r , the ratio of the tensor to scalar power spectrum). Figure 14 shows the likelihood contours for the slope of the scalar fluctuations and the amplitude of the gravitational wave signal.

Table 7: Best Fit Inflationary Parameters (WMAP data only)

Parameter	Λ CDM + Tensor	Λ CDM + Running + Tensors
$\Omega_b h^2$	$0.02336^{+0.00085}_{-0.00133}$	$0.0220^{+0.0011}_{-0.0016}$
$\Omega_m h^2$	$0.1189^{+0.0084}_{-0.0136}$	$0.1258^{+0.0070}_{-0.0162}$
h	$0.792^{+0.036}_{-0.068}$	$0.744^{+0.050}_{-0.073}$
n_s	$0.987^{+0.019}_{-0.037}$	$1.21^{+0.13}_{-0.16}$
$dn_s/d \ln k$	set to 0	$-0.102^{+0.050}_{-0.043}$
r	0.55 (95% CL)	1.5 (95% CL)
τ	$0.091^{+0.031}_{-0.037}$	$0.111^{+0.029}_{-0.037}$
σ_8	$0.700^{+0.063}_{-0.065}$	$0.716^{+0.065}_{-0.068}$
$\Delta_{\mathcal{R}}^2(k = 0.05/Mpc)$	$(19.9^{+1.3}_{-1.8}) \times 10^{-10}$	$(20.9^{+1.3}_{-1.9}) \times 10^{-10}$

The WMAP three year data place significant constraints on inflationary models. The strength of these constraints is apparent when we consider monomial models for the inflaton potential, $V(\phi) \propto \phi^\alpha$. These models (Lyth & Riotto 1999) predict

$$\begin{aligned}
 r &= 16\epsilon_1 \simeq \frac{4\alpha}{N} \\
 1 - n_s &= 2\epsilon_1 + \epsilon_2 \simeq \frac{\alpha + 2}{2N}
 \end{aligned} \tag{13}$$

where N is the number of e-folds of inflation between the epoch when the horizon scale modes left the horizon and the end of inflation. Figure 14 compares the predictions of these

monomial inflationary models to the data. For $N = 60$, $\lambda\phi^4$ predicts $r = 4/15, n_s = 0.95$, just at the outer edge of the 3σ contour. For $N = 50$, $\lambda\phi^4$ predicts $r = 0.32, n_s = 0.94$, well outside the 3σ contour. However, if we allow for non-minimal gravitational couplings, then the gravity wave predictions of these models are significantly reduced (Hwang & Noh 1998; Komatsu & Futamase 1999) and the models are consistent with the data. Alternatively, the $m^2\phi^2$ model is a good fit to the observations and its predicted level of gravitational waves, $r \simeq 0.16$, is within range of upcoming experiments.

In Peiris et al. (2003), we used the inflationary flow equations (Hoffman & Turner 2001; Kinney 2002) to explore the generic predictions of inflationary models. Here, we use the slow-roll approximation to explore the implications of the data for inflationary models. The results of the third year analysis are consistent with the conclusions from the first year data: while the data rule out large regions of parameter space, there are also wide range of possible inflationary models consistent with our current data. One of the most intriguing features of Figure 14 is that the data now disfavors the exact Peebles-Harrison-Zel'dovich spectrum ($n_s = 1, r = 0$). For power law inflationary models, this suggests a detectable level of gravity waves. There are, however, many inflationary models that predict a much smaller gravity wave amplitude. Alternative models, such as the ekpyrotic scenario (Khoury et al. 2001, 2002) also predict an undetectable level of gravity waves.

There are several different ways of expressing the constraints that the CMB data impose of inflationary models. These parameters can be directly related to observable quantities: $n_s - 1 = -2\epsilon_1 - \epsilon_2$ and $r = 16\epsilon_1$. For the power law models, the WMAP bound on r implies that $\epsilon_1 < 0.03$ (95% C.L.). An alternative slow roll representation (see Liddle & Lyth (1992, 1993)) uses

$$\epsilon_v \equiv \frac{M_{Pl}^2}{2} \left(\frac{V'}{V} \right)^2 \quad (14)$$

$$\eta_v \equiv M_{Pl}^2 \left(\frac{V''}{V} \right) \quad (15)$$

These parameters can be related directly to observables: $r = 16\epsilon_v$ and $n_s - 1 = -6\epsilon_v + 2\eta_v$. Peiris et al. (2003) discusses various classes of models in slow roll parameter space.

Models with significant gravitational wave contributions, $r \sim 0.3$, make a number of different predictions for CMB and large-scale structure observations: (a) a modified temperature spectrum with more power at low multipoles; and (b) a lower amplitude of density fluctuations (for fixed CMB fluctuations). For power law models, the strongest CMB constraints come from the shape of the temperature spectrum and the amplitude of density fluctuations. In order to fit the CMB data, models with higher r values require larger values of n_s and lower amplitude of scalar fluctuations to fit the data. Since these values con-

flict with the large-scale structure measurements, the strongest overall constraints on the tensor mode contribution comes from the combination of CMB and large-scale structure measurements (see Table 6). These strong limits rely on our assumption of a power law spectral index. If we allow for a running index, then models with large tensor components are consistent with the data

Table 8: Constraints on r , Ratio of Amplitude of Tensor Fluctuations to Scalar Fluctuations (at $k = 0.002 \text{ Mpc}^{-1}$)

Data Set	r (no running)	r (with running)
WMAP	0.55 (95% CL)	1.5 (95% CL)
WMAP+BOOM+ACBAR	0.63 (95% CL)	1.4 (95% CL)
WMAP+CBI+VSA	0.55 (95% CL)	1.1 (95% CL)
WMAP+2df	0.30 (95% CL)	1.0 (95% CL)
WMAP+SDSS	0.28 (95% CL)	0.67 (95% CL)

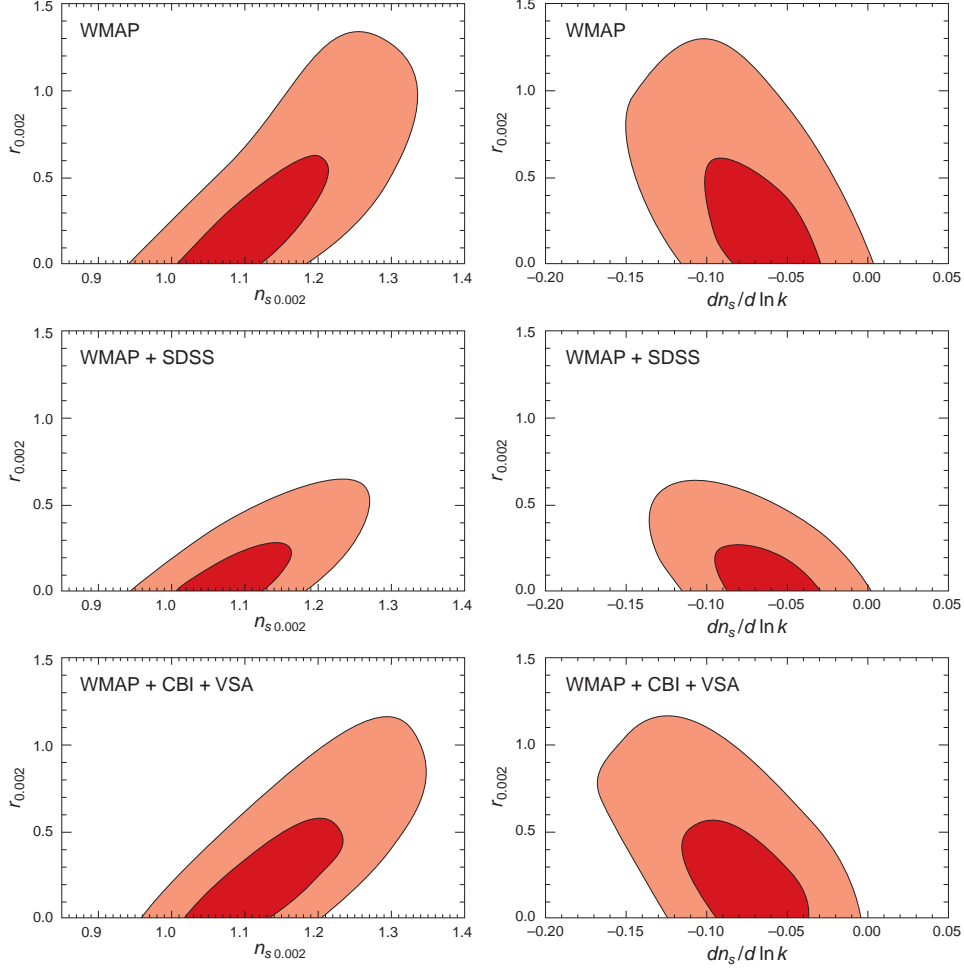


Fig. 12.— Joint two-dimensional marginalized contours (68% and 95%) for inflationary parameters, (r, n_s) (left panel) and $(r, dn_s/d \ln k)$ (right panel), for Model M11 in Table 3, with parameters defined at $k = 0.002 \text{ Mpc}^{-1}$. (Upper) WMAP only. (Middle) WMAP+SDSS. (Bottom) WMAP+CBI+VSA. Note that $n_s > 1$ is favored because r and n_s are defined at $k = 0.002 \text{ Mpc}^{-1}$. At $k = 0.05 \text{ Mpc}^{-1}$ $n_s < 1$ is favored. The data do not require the running spectral index, $dn_s/d \ln k$, at more than the 95% confidence level.

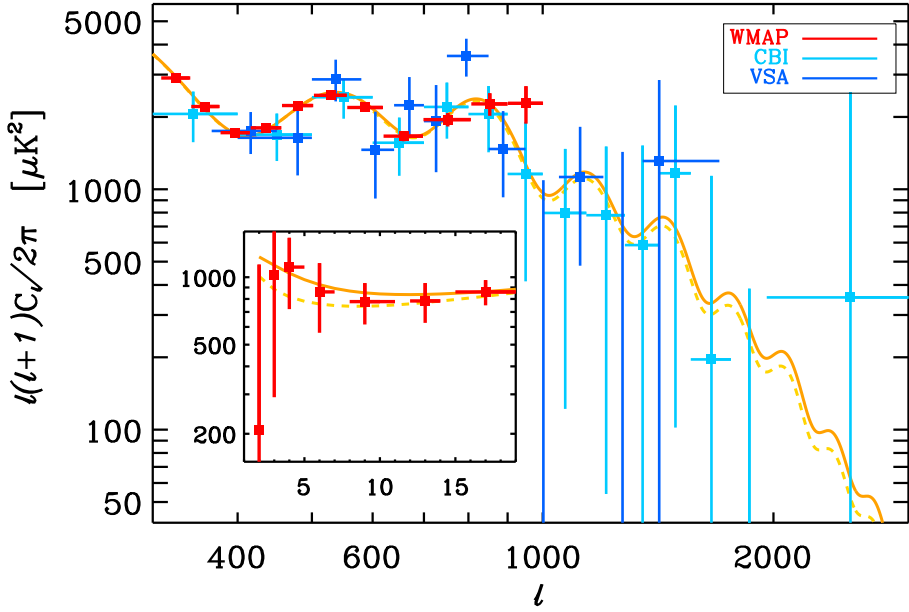


Fig. 13.— The running spectral index model provides a slightly better fit to the data than the power-law spectral index model. The solid line shows the best fit power law Λ CDM model and the dashed line shows the best fit running spectral index Λ CDM model (fit to WMAP+CBI+VSA). The insert compares the models to the WMAP $\ell < 20$ data and shows that the running spectral index model better fits the decline at $\ell = 2$; however, the improvement in χ^2 is only 3, not enough to strongly argue for the addition of a new parameter. We have also done the same analysis for BOOMERanG and ACBAR data and found similar results: the current high ℓ data are not yet able to distinguish between the running spectral index and power law models.

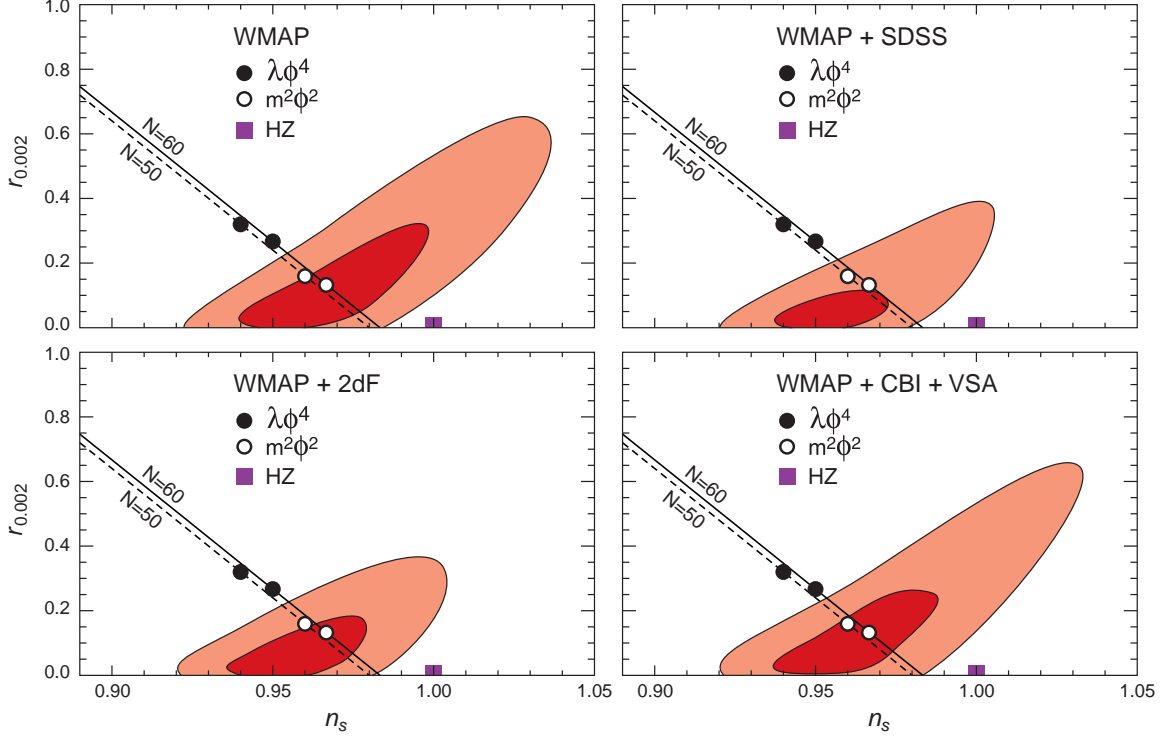


Fig. 14.— Joint two-dimensional marginalized contours (68% and 95% confidence levels) for inflationary parameters ($r_{0.002}$, n_s) predicted by monomial potential models, $V(\phi) \propto \phi^n$. We assume a power-law primordial power spectrum, $dn_s/d\ln k = 0$, as these models predict the negligible amount of running index, $dn_s/d\ln k \approx -10^{-3}$. (Upper left) WMAP only. (Upper right) WMAP+SDSS. (Lower left) WMAP+2dFGRS. (Lower right) WMAP+CBI+VSA. The dashed and solid lines show the range of values predicted for monomial inflaton models with 50 and 60 e-folds of inflation (equation (13), respectively. The open and filled circles show the predictions of $m^2\phi^2$ and $\lambda\phi^4$ models for 50 and 60 e-folds of inflation. The rectangle denotes the scale-invariant Harrison-Zel'dovich-Peebles (HZ) spectrum ($n_s = 1, r = 0$). Note that the current data prefers the $m^2\phi^2$ model over both the HZ spectrum and the $\lambda\phi^4$ model by likelihood ratios greater than 50.

7. Constraining the Composition of the Universe

7.1. Dark Energy Properties

Over the past two decades, there has been growing evidence for the existence of dark energy (Peebles 1984; Turner et al. 1984; Ostriker & Steinhardt 1995; Dunlop et al. 1996; Bahcall et al. 1999). By measuring both the acceleration (Riess et al. 1998; Perlmutter et al. 1999) and deceleration (Riess et al. 2004) of the universe, supernova observations provide the most direct evidence for the existence of dark energy.

The nature of this dark energy is a mystery. From a field theoretic perspective the most natural explanation for this would be the presence of a residual vacuum energy density or cosmological constant, Λ , (Carroll et al. 1992; Peebles & Ratra 2003). However, there are well-known fine-tuning and coincidence problems in trying to explain the 120 orders-of-magnitude discrepancy between the expected “natural” Planck-scale energy density of a cosmological constant and the observed dark energy density. These problems motivate a wide range of alternative explanations for the observations including the presence of an extra matter candidate: for example a dynamical, scalar “quintessence” field (Peebles & Ratra 1988; Wetterich 1988; Zlatev et al. 1999), minimally coupled (Caldwell et al. 1998; Ferreira & Joyce 1998) or non-minimally coupled to gravity (Amendola 1999) or other matter (Bean & Magueijo 2001). In this final case, the measured acceleration is due to underlying interactions in the matter bulk. Another alternative is that modifications to gravity (e.g., Deffayet et al. (2001)) are responsible for the observed anomalies.

The dark energy has two distinct cosmological effects: (1) through the Friedman equation, it alters the evolution of $H(z)$ and (2) through the perturbation equations, it alters the evolution of $D(z)$, the growth rate of structure. The supernova data measures only the luminosity distance, which depends on $H(z)$. The large scale structure data are sensitive to both $H(z)$ and $D(z)$.

While the presence of dark energy impacts the CMB primarily through the distance to the surface of last scatter, the dark energy clustering properties also alter the CMB properties. The dark energy response to gravitational perturbations depends upon its isotropic and anisotropic sound-speeds (Hu 1998; Bucher & Spergel 1999). This affects the CMB fluctuations through the ISW effect. If the dark energy can cluster, then it produces a smaller ISW effect and does not enhance the power spectrum at large angular scales. These effects are most dramatic for models with $w < -1$, as dark energy effects in these models turn on suddenly at late times and significantly enhance the quadrupole. This can be understood in terms of the constraints imposed by the shape of the angular power spectrum: if we assume that the dark energy properties can be described by a constant value of w , then fixed peak

Table 9: Constraints on w in Flat Cosmologies With Different Assumption About Dark Energy Clustering

Data Set	with perturbations	no perturbations
WMAP + SDSS	$-0.75^{+0.18}_{-0.16}$	$-0.69^{+0.19}_{-0.18}$
WMAP + 2dFGRS	$-0.914^{+0.193}_{-0.099}$	$-0.877^{+0.094}_{-0.110}$
WMAP + SNGold	$-0.944^{+0.076}_{-0.094}$	$-0.940^{+0.071}_{-0.092}$
WMAP + SNLS	$-0.966^{+0.070}_{-0.090}$	$-0.984^{+0.066}_{-0.085}$
CMB+ LSS+ SN	$-0.926^{+0.051}_{-0.075}$	$-0.915^{+0.049}_{-0.075}$

position and fixed peak heights (which determine $\Omega_m h^2$) confine our models to a narrow valley in the (Ω_m, w) likelihood surface as shown in Figure 15 and 16. The figures show that the 3 year data enable a more accurate determination of $\Omega_m h^2$ which narrows the width of the degeneracy valley. The pair of figures show that CMB data can place strong limits on models with $w < -1$ and non-clustering dark energy. On the other hand, if the dark energy is a matter component that can cluster, even meagerly, as is the case for scalar field theories where $c_s^2=1$, then this clustering counters the suppression of perturbation growth during the accelerative epoch and the quadrupole's magnitude is reduced. This lessens the discriminating power of the quadrupole for measuring w : while CMB data rules out the $w \ll -1$ region in Figure 15, it does not constrain models in the same region in Figure 16.

It's interesting to note that if we relax the assumption of spatial flatness allowing for $\Omega_K \neq 0$ a universe with a negative equation of state, close to $w = -1$ is still preferred by the data, as shown in figure 17.

7.2. Neutrino Properties

7.2.1. Neutrino Mass

Both atmospheric neutrino experiments and solar neutrino experiments show that neutrinos are massive and that there is significant mixing between the various neutrino interaction eigenstates (see Mohapatra et al. (2005) for a recent review). These experiments measure the difference between square of the neutrino masses, $m_{\nu_i}^2 - m_{\nu_j}^2$, rather than the mass of individual neutrino mass eigenstates. Cosmological measurements nicely complement these measurements by constraining $\sum_i m_{\nu_i}$. Since light massive neutrinos do not cluster as effectively as cold dark matter, the neutrino mass has a direct impact on the amplitude and

shape of the matter power spectrum (Bond et al. 1980; Bond & Szalay 1983; Ma 1996; Hu et al. 1998) The presence of a significant neutrino component lowers the amplitude of matter fluctuations on small scales, σ by roughly a factor of $(\sum m_\nu)/3$, where $\sum m_\nu$ is the total mass summed over neutrino species, rather than the mass of individual neutrino species. The current large-scale structure data restrict $\Delta \ln \sigma_8 < 0.2$, but they are not sensitive enough to resolve the free-streaming scale of individual neutrino species (Takada et al. 2005).

Using a combination of the first year WMAP data, small-scale CMB and large-scale structure data, Spergel et al. (2003) placed an upper limit on $\sum_i m_{\nu_i} < 0.7$ eV. While this limit does not depend on the Lyman α data, it is sensitive to the bias measurements (which normalizes the large-scale structure data) and to the addition of small scale CMB data (which improves the measurements of cosmological parameters). Over the past year, several groups obtained comparable (but slightly different) limits (Hannestad 2003; Pierpaoli 2003; Elgarøy & Lahav 2003). The differences are due to including (or removing) external data sets and priors or adding additional cosmological parameters.

The limits on neutrino masses from WMAP data alone is now very close to limits based on combined CMB data sets. Ichikawa et al. (2005) used the CMB data alone to place a limit on the neutrino mass of $\sum m_\nu < 2.0$ eV. Using WMAP data alone, we now find $\sum m_\nu < 2.11$ eV.

Since the presence of massive neutrinos slows the growth of small scale structure, the combination of CMB and large-scale structure data constrain the neutrino mass. Figure 19 shows the likelihood function as a function of neutrino mass and amplitude of mass fluctuations in the local universe, σ_8 . The 95% confidence limits on neutrino mass are given in Table 10. The combination of WMAP with SDSS and WMAP with 2dFGRS data constrain σ_8 at roughly the same level, 20% at the 95% confidence level. This constraint yields comparable limits on the neutrino mass: $\sum m_\nu < 0.72$ eV (95% C.L.) While the WMAP data have improved, the error bars on σ_8 have not significantly changed from the limits obtained from WMAPext + 2dFGRS, thus, the limit on neutrino mass is quite close to the first year limit. Note that in the first year analysis, we used the (Verde et al. 2002) measurement of bias for the 2dFGRS preliminary data as there had not been an equivalent analysis done for the full 2dFGRS data set. As discussed in §4.1.4, we now marginalize over the 2dFGRS bias and use the bias measurements of (Seljak et al. 2005b) for SDSS.

If the constraints on amplitude are robust, then small scale matter power spectrum structure data can significantly improve these neutrino constraints. Goobar et al. (2006) have recently completed a CMB + Lyman α study and place a limit of $\sum m_\nu < 0.30$ eV (95% C.L.). Similarly, cluster-based measurements of σ_8 and lensing-based measurements of σ_8 have the potential to tighten the constraint on m_ν .

Table 10: Constraints on Neutrino Properties

Data Set	$\sum m_\nu$ (95% limit for $N_\nu = 3.02$)	N_ν
WMAP	2.0 eV(95% CL)	
WMAP + SDSS	0.91 eV(95% CL)	$5.92^{+0.25}_{-3.45}$
WMAP + 2dFGRS	0.87 eV(95% CL)	$2.68^{+0.26}_{-1.67}$
CMB + LSS +SN	0.68 eV(95% CL)	$3.29^{+0.45}_{-2.18}$

7.2.2. Number of Relativistic Species

If there are other light stable neutral particles (besides the three light neutrinos and the photon), then these particles will affect the CMB angular power spectrum and the evolution of large-scale structure. Because of the details of freeze-out at electron-positron annihilation (Gnedin & Gnedin 1998), the effective number of neutrino species is slightly greater than 3. Any light particle that does not couple to electrons, ions and photons will act as an additional relativistic species. For neutrinos, we can compute their effects accurately as their temperature is $(4/11)^{1/3}$ of the CMB temperature. For other relativistic species, the limit on $N_\nu^{eff} - 3.022$ can be converted into a limit on their abundance by scaling by the temperature.

The shape of the CMB angular power spectrum is sensitive to the epoch of matter/radiation equality. If we increase N_ν , the effective number of neutrino species, then we will need to also increase the cold dark matter density, $\Omega_c h^2$, and slowly change other parameters to remain consistent with the WMAP data (Bowen et al. 2002). In addition, the presence of these additional neutrino species alters the damping tail and leaves a distinctive signature on the high ℓ angular power spectrum (Bashinsky & Seljak 2004) and on the small scale matter power spectrum.

The high matter density also alters the growth rate of structure, thus, the combination of large-scale structure and CMB data constrains the existence of any new light relativistic species. These limits constrain both the existence of new particles and the interaction properties of the neutrino (Bowen et al. 2002; Hall & Oliver 2004). Hannestad (2001) used the pre-WMAP CMB and large-scale structure data to place an upper limit of $N_\nu < 17$. After the release of the first year WMAP data, several authors (Hannestad 2003; Pierpaoli 2003; Barger et al. 2003; Crotty et al. 2003; Elgarøy & Lahav 2003; Barger et al. 2004; Hannestad 2005) used the combination of WMAP, 2dFGRS and various external data to reduce this limit by a factor of 2-3. Table 10 shows the maximum likelihood estimate of the number of neutrino species for different data set combinations using the new WMAP data. The SDSS

and 2dFGRS data differ in the shapes of the two measured power spectra: this difference leads to the disagreement in their best fit values for N_{ν}^{eff} .

7.3. Non-Flat Universe

The WMAP observations place significant constraints on the geometry of the universe through the positions of the acoustic peaks. The sound horizon size, r_s , serves as a very useful ruler for measuring the distance to the surface of last scatter. For power law open universe models, $r_s = 147.8_{-2.7}^{+2.6}$ Mpc. Figure 21 shows that this constraint confines the likelihood function to a narrow degeneracy surface in $(\Omega_m, \Omega_\Lambda)$. This degeneracy line is well fit by $\Omega_K = -0.3040 + 0.4067\Omega_\Lambda$. However, the CMB data alone does not distinguish between models along the valley: it is consistent with both flat models and models with $\Omega_\Lambda = 0$. If we allow for a large SZ signal, then the WMAP data alone favors a model with $\Omega_K = -0.04$; however, this model is not consistent with other astronomical data.

The combination of WMAP data and other astronomical data places strong constraints on the geometry of the universe (see Table 11):

- The angular scale of the baryon acoustic oscillation (BAO) peak in the SDSS LRG sample (Eisenstein et al. 2005) measures the distance to $z = 0.35$. The combination of the BAO and CMB observations strongly constrain the geometry of the universe. The position of the peak in the galaxy spectrum in the SDSS and 2dFGRS surveys provide local measurements of the angular diameter distance.
- Figure 20 shows that the Hubble constant varies along this line, so that the HST key project constraint on the Hubble constant leads to a strong bound on the curvature.
- SNe observations measure the luminosity distance to $z \sim 1$. The combination of SNe data and CMB data also favors a nearly flat universe.

The strong limits quoted in Table 11 rely on our assumption that the dark energy has the equation of state, $w = -1$. In section 7.1, we discussed relaxing this assumption and assuming that w is a constant. Figure 15 shows that by using the combination of CMB, large-scale structure and supernova data, we can simultaneously constrain both Ω_k and w . This figure confirms that our minimal model, $\Omega_k = 0$ and $w = -1$ is consistent with the current data.

Table 11: Joint Data Set Constraints on Geometry and Vacuum Energy

Data Set	Ω_K	Ω_Λ
WMAP + $h = 0.72 \pm 0.08$	$-0.003^{+0.013}_{-0.017}$	$0.758^{+0.035}_{-0.058}$
WMAP + SDSS	$-0.037^{+0.021}_{-0.015}$	$0.650^{+0.055}_{-0.048}$
WMAP + 2dFGRS	$-0.0057^{+0.0061}_{-0.0088}$	$0.739^{+0.026}_{-0.029}$
WMAP + SDSS LRG	$-0.010^{+0.011}_{-0.015}$	$0.728^{+0.020}_{-0.028}$
WMAP + SNLS	$-0.015^{+0.020}_{-0.016}$	$0.719^{+0.021}_{-0.029}$
WMAP + SNGold	$-0.017^{+0.022}_{-0.017}$	$0.703^{+0.030}_{-0.038}$

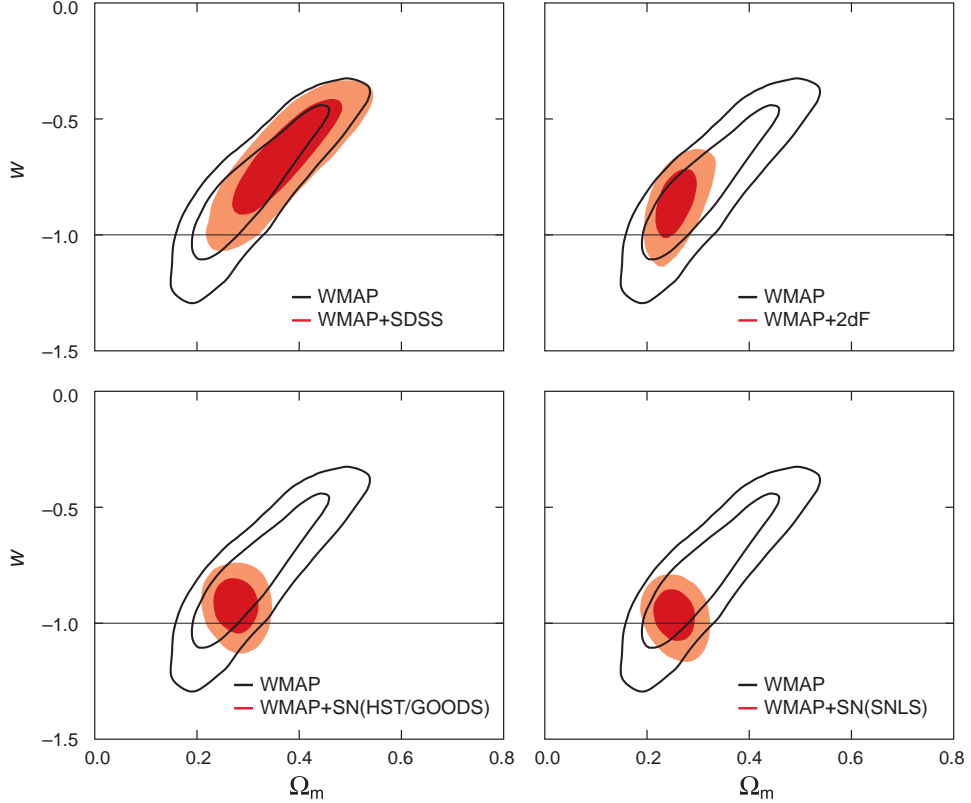


Fig. 15.— Constraints on w , the equation of state of dark energy, in a flat universe model based on the combination of WMAP data and other astronomical data. We assume that w is independent of time, and ignore density or pressure fluctuations in dark energy. In all of the figures, WMAP data only constraints are shown in blue and WMAP + astronomical data set in red. The contours show the joint 2-d marginalized contours (68% and 95% confidence levels) for Ω_m and w . (Upper left) WMAP only and WMAP + SDSS. (Upper right) WMAP only and WMAP + 2dFGRS. (Lower left) WMAP only and WMAP+SN(HST/GOODS). (Lower right) WMAP only and WMAP+SN(SNLS). In the absence of dark energy fluctuations, the excessive amount of ISW effect at $\ell < 10$ places significant constraints on the models with $w < -1$.

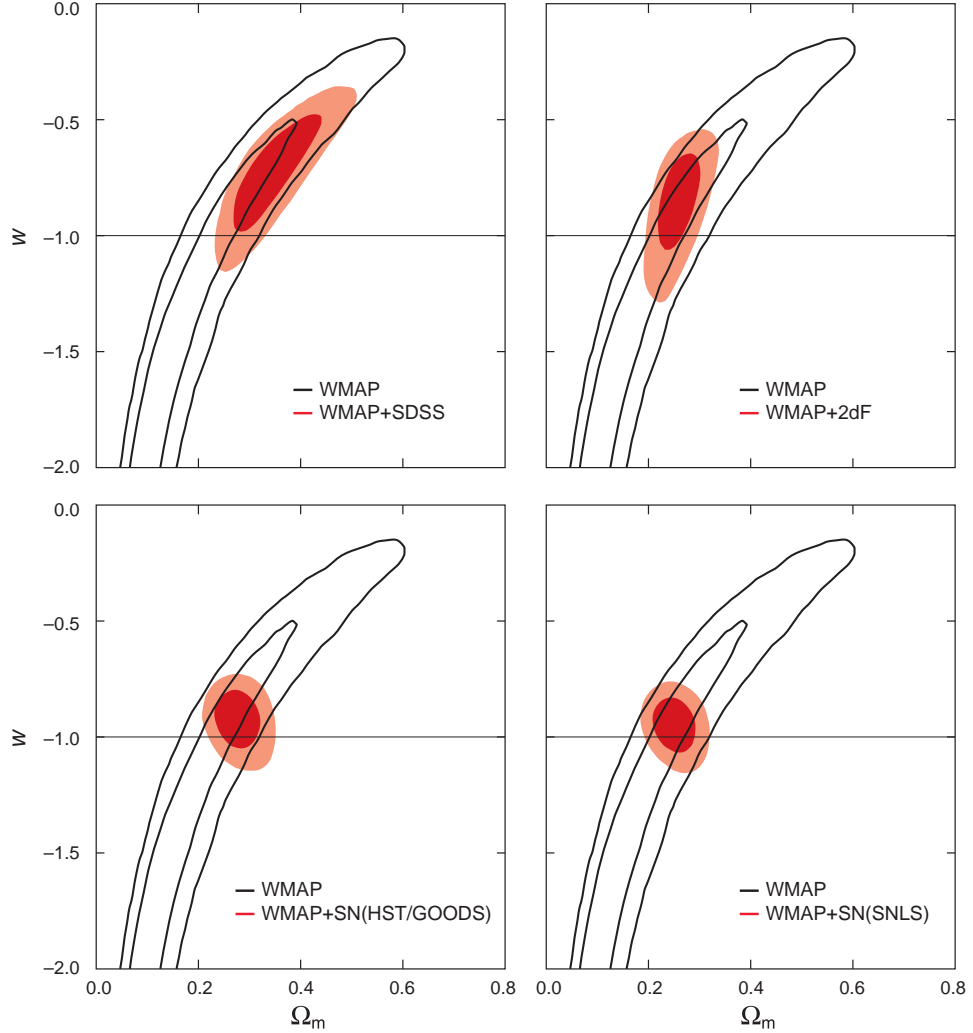


Fig. 16.— Constraints on w , the equation of state of dark energy, in a flat universe, Model M6 in Table 3, based on the combination of WMAP data and other astronomical data. We assume that w is independent of time, but include density and pressure fluctuations in dark energy with the speed of sound in the comoving frame equal to the speed of light, $c_s^2 = 1$. In all of the figures, WMAP data only constraints are shown in black solid lines and WMAP + astronomical data set in red. The contours show the joint 2-d marginalized contours (68% and 95% confidence levels) for Ω_m and w . (Upper left) WMAP only and WMAP + SDSS. (Upper right) WMAP only and WMAP + 2dFGRS. (Lower left) WMAP only and WMAP+SNgold. (Lower right) WMAP only and WMAP+SNLS. In the presence of dark energy fluctuations, the ISW effect at $\ell < 10$ is nearly canceled by dark energy fluctuations and thus the WMAP data alone do not place significant constraints on w .

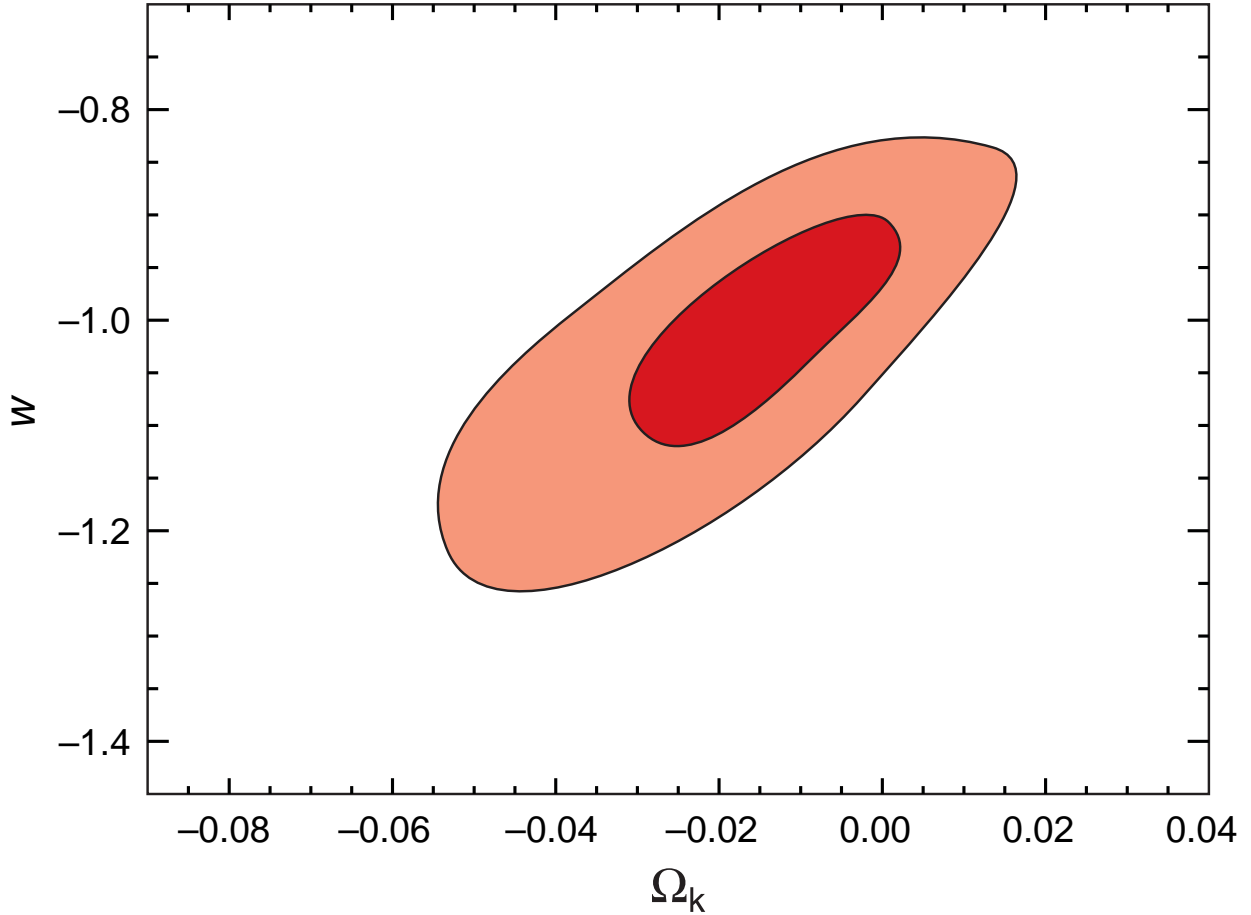


Fig. 17.— Constraints on a non-flat universe with quintessence-like dark energy with constant w (Model M10 in Table 3). The contours show the 2-d marginalized contours for w and Ω_k based on the the CMB+2dFGRS+SDSS+supernova data sets. This figure shows that with the full combination of data sets, there are already strong limits on w without the need to assume a flat universe prior. The marginalized best fit values for the equation of state and curvature are $w = -1.062^{+0.128}_{-0.079}$ and $\Omega_k = -0.024^{+0.016}_{-0.013}$ at the 68% confidence level.

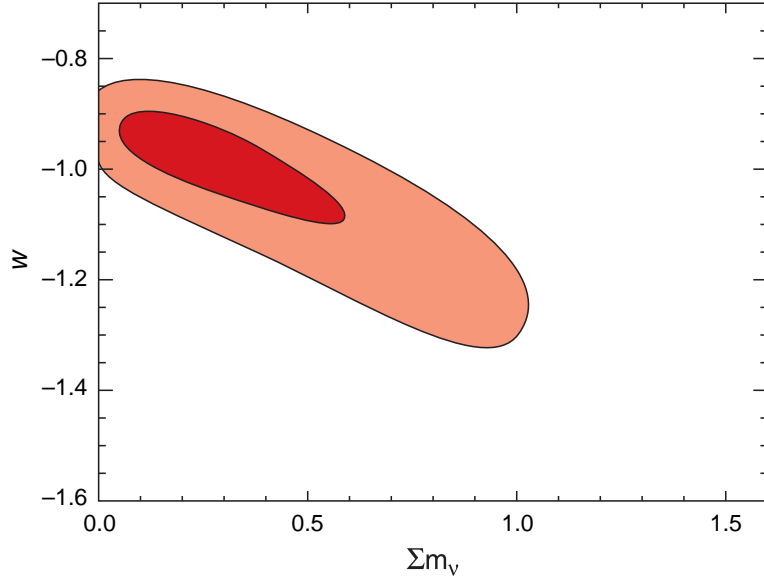


Fig. 18.— Constraints on a flat universe with quintessence-like dark energy and non-relativistic neutrinos. The contours show the 2-d marginalized contours for the mass of non-relativistic neutrinos, m_ν , and the dark energy equation of state, w , assumed constant, based on the the CMB+2dFGRS+SDSS+supernova data sets. The figure shows that with the combination of CMB+2dFGRS+SDSS+supernova data sets, there is not a strong degeneracy between neutrino and dark energy properties. Even in this more general model, we still have an interesting constraint on the neutrino mass and equation of state: $\sum m_\nu < 1.0$ eV(95% CL) and $w = -1.06^{+0.13}_{-0.10}$ (68% CL). This suggests that the astronomical dark energy and neutrino limits are robust even when we start to consider more baroque models.

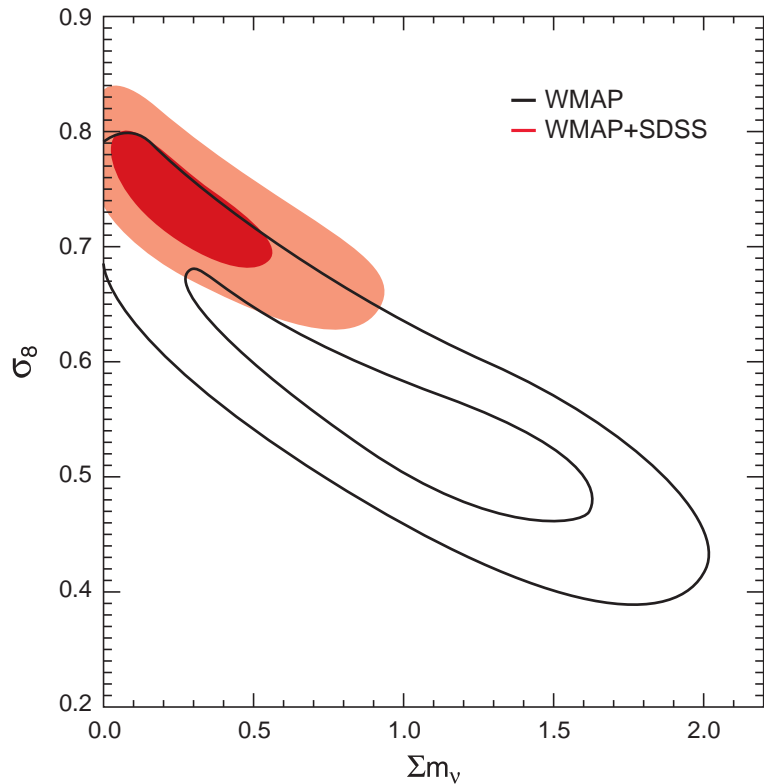


Fig. 19.— Joint two-dimensional marginalized contours (68% and 95% confidence levels) of (σ_8, m_ν) for WMAP only (left panel), Model M7 in Table 3, and WMAP+SDSS (right panel). By measuring the growth rate of structure from $z = 1088$ to $z \simeq 0$, these observations constrain the contribution of non-relativistic neutrinos to the energy density of the universe.

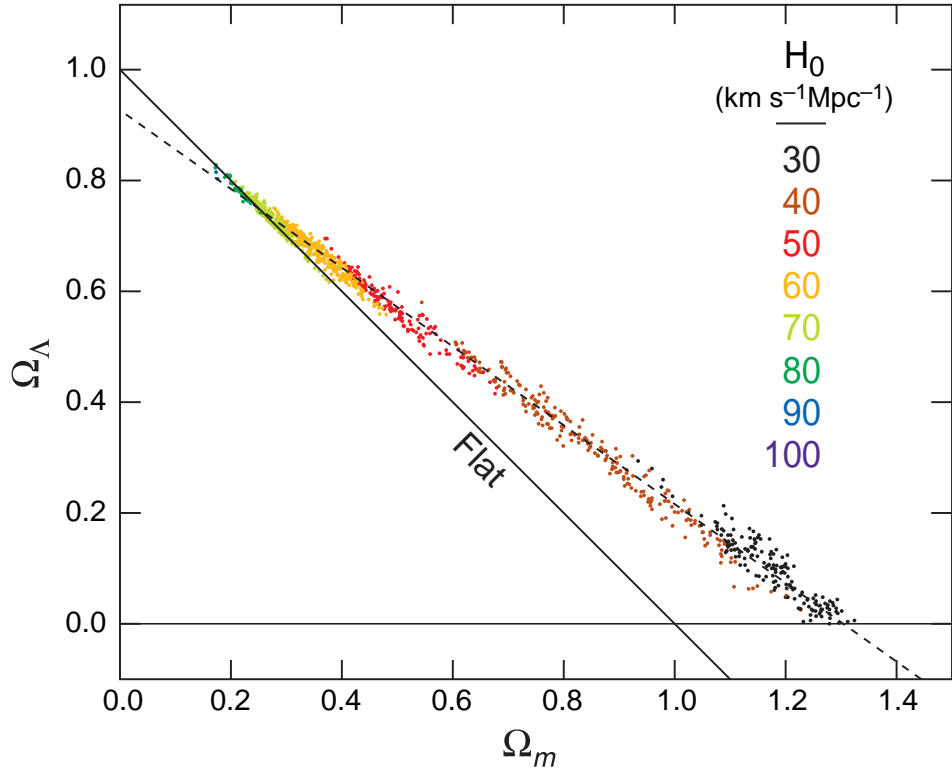


Fig. 20.— Range of non-flat cosmology models consistent with the WMAP data only. The models in the figure are all power-law CDM models with dark energy and dark matter, but without the constraint that $\Omega_m + \Omega_\Lambda = 1$ (model M10 in Table 3). The different colors correspond to values of the Hubble constant as indicated in the figure. While models with $\Omega_\Lambda = 0$ are not disfavored by the WMAP data only ($\Delta\chi^2_{eff} = 0$; Model M4 in Table 3), the combination of WMAP data plus measurements of the Hubble constant strongly constrain the geometry and composition of the universe within the framework of these models. The dashed line shows an approximation to the degeneracy track: $\Omega_K = -0.3040 + 0.4067\Omega_\Lambda$.

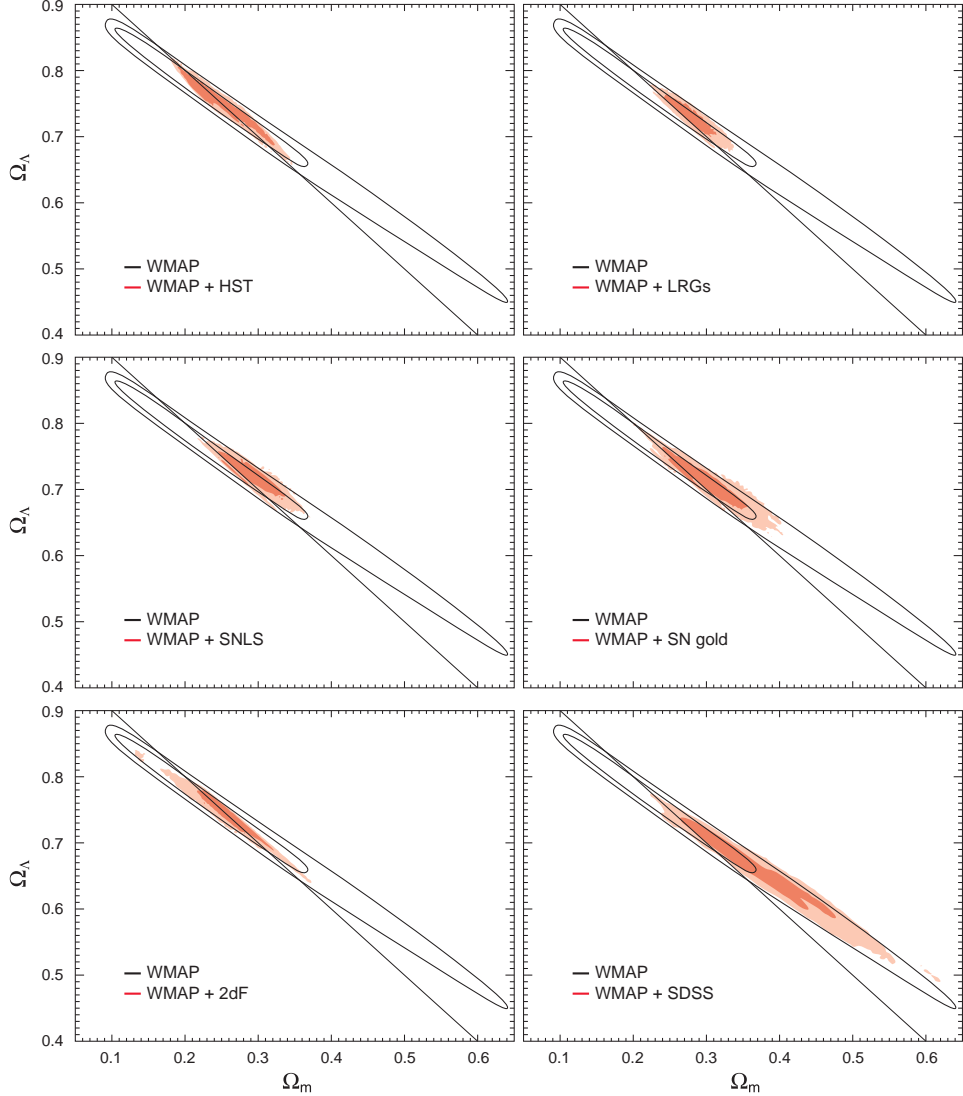


Fig. 21.— Joint two-dimensional marginalized contours (68% and 95%) for matter density, Ω_m , and vacuum energy density, Ω_Λ for power-law CDM models with dark energy and dark matter, but without the constraint that $\Omega_m + \Omega_\Lambda = 1$ (model M10 in Table 3). The panels show various combinations of WMAP and other data sets. While models with $\Omega_m = 0.415$ and $\Omega_\Lambda = 0.630$ are a better fit to the WMAP three year data alone than the flat model, the combination of WMAP three year data and other astronomical data favors nearly flat cosmologies. (Upper left) WMAP+HST key project measurement of H_0 . (Upper right) WMAP+SDSS LRG measurement of the angular diameter distance to $z = 0.35$. (Middle left) WMAP+SNLS data. (Middle right) WMAP+SNGold. (Lower left) WMAP+2dFGRS. (Lower right) WMAP+SDSS. Note that for this figure we assume a flat prior on H_0 .

8. Are CMB Fluctuations Gaussian?

The detection of primordial non-Gaussian fluctuations in the CMB would have a profound impact on our understanding of the physics of the early universe. While the simplest inflationary models predict only mild non-Gaussianities that should be undetectable in the WMAP data, there are a wide range of plausible mechanisms for generating significant and detectable non-Gaussian fluctuations (Bartolo et al. (2004a) for a recent review). There are a number of plausible extensions of the standard inflationary model (Lyth et al. 2003; Dvali et al. 2004; Bartolo et al. 2004b) or alternative early universe models (Arkani-Hamed et al. 2004; Alishahiha et al. 2004) that predict skewed primordial fluctuations at a level detectable by WMAP.

There are other cosmological mechanisms for generating non-Gaussianity. The smallness of the CMB quadrupole seen by both WMAP and COBE has stimulated interest in the possibility that the universe may be finite (Luminet et al. 2003; Aurich et al. 2005). If the universe were finite and had a size comparable to horizon size today, then the CMB fluctuations would be non-Gaussian (Cornish et al. 1996; Levin et al. 1997; Bond et al. 2000; Inoue et al. 2000). While analysis of the first year data did not find any evidence for a finite universe (Phillips & Kogut 2004; Cornish et al. 2004), these searches were non-exhaustive so the data rule out most but not all small universes.

Using an analysis of Minkowski functionals, Komatsu et al. (2003) did not find evidence for statistically isotropic but non-Gaussian fluctuations in the first year sky maps. The Colley & Gott (2003) reanalysis of the maps confirmed the conclusion that there was no evidence of non-Gaussianity.

For a broad class of theories, we can parameterize the effects of non-linear physics by a simple coupling term that couples a Gaussian random field, ψ , to the Bardeen curvature potential, Φ :

$$\Phi(\vec{x}) = \psi(\vec{x}) + f_{NL}\psi^2(\vec{x}) \quad (16)$$

Simple inflationary models based on a single slowly-rolling scalar field with the canonical kinetic Lagrangian predict $|f_{NL}| < 1$ (Maldacena 2003; Bartolo et al. 2004a); however, curvaton inflation (Lyth et al. 2003), ghost inflation (Arkani-Hamed et al. 2004), and Dirac-Born-Infeld (DBI) inflation models (Alishahiha et al. 2004) can generate much larger non-Gaussianity, $|f_{NL}| \sim 100$. Using the WMAP first year data, Komatsu et al. (2003) constrained $-54 < f_{NL} < 134$ at the 95% confidence level. Several different groups (Gaztañaga & Wagg 2003; Mukherjee & Wang 2004; Cabella et al. 2004; Phillips & Kogut 2004; Creminelli et al. 2005) have applied alternative techniques to measure f_{NL} from the maps and have similar limits on f_{NL} . Babich et al. (2004) note that these limits are sensitive to the

physics that generated the non-Gaussianity as different mechanisms predict different forms for the bispectrum.

Since the release of the WMAP data, several groups have claimed detections of significant non-Gaussianities (Tegmark et al. 2003; Eriksen et al. 2004b; Copi et al. 2003; Vielva et al. 2004; Hansen et al. 2004; Park 2004; Cruz et al. 2005). Almost all of these claims imply that the CMB fluctuations are not stationary and claim a preferred direction or orientation in the data. Hajian et al. (2005) argue that these detections are based on *a posteriori* selection of preferred directions and do not find evidence for preferred axes or directions. Because of the potential revolutionary significance of these detections, they must be treated with some caution. Galactic foregrounds are non-Gaussian and anisotropic, and even low level contamination in the maps can produce detectable non-Gaussianities (Chiang et al. 2003; Naselsky et al. 2005), but have only minimal effects on the angular power spectrum (Hinshaw et al. 2003). Because of the WMAP scan pattern, the variance in the noise in the maps is spatially variable. There is significant $1/f$ noise in several of the Difference Assemblies (DAs) (particularly W4)— which leads to anisotropies in the two-point function of the noise. Finally, most of the claimed detections of significant non-Gaussianities are based on *a posteriori* statistics. Many of the claimed detections of non-Gaussianity can be tested with the three year WMAP data (available at lambda.gsfc.nasa.gov). Future tests should use the simulated noise maps, Monte Carlo simulations and the difference maps (year 1 – year 2, year 2 – year 3, etc.) to confirm that the tests are not sensitive to noise statistics and the multi-frequency data to confirm that any claimed non-Gaussianity has a thermal spectrum. Claims of non-Gaussianity incorporating data close to the galactic plane (within the Kp2 cut) should be treated with caution, as the foreground corrections near the plane are large and uncertain.

The following subsections describe a number of statistical tests designed to search for non-Gaussianities in the microwave sky. All of these analyses use three year maps cleaned with the KKHaDust templates (Hinshaw et al. 2006). We refer to these maps as the “template-cleaned maps”. In the first subsection, we show that the probability distribution function of the cleaned CMB maps is consistent with Gaussianity. In the second subsection, we show that the Minkowski functionals are consistent with expectations for Gaussian fluctuations. Next, we compute the bispectrum of the cleaned maps. The final subsection describes measurements of the four point function.

8.1. One Point Distribution Function

One of the simplest tests of non-Gaussianity is a measurement of the one point probability function. However, because the detector noise in the map is inhomogeneous (higher in the ecliptic plane and lower near the poles), this test is non-trivial. We account for the spatial variations in noise by computing a variance-normalized temperature for each pixel in a given map:

$$u_i = \frac{T_i}{\sqrt{\sigma_{noise}^2/N_{obs} + \sigma_{CMB}^2}} \quad (17)$$

where T_i is the measured temperature signal, the detector noise depends on the number of observations of a given pixel, N_{obs} . Here, we apply the analysis to template-cleaned maps outside the Kp2 skycut. For this analysis, we compute σ_{noise} , the noise per observation, from the year 1 – year 2 difference maps and fit σ_{CMB} , the CMB signal, to the sum of the year one and year two maps. With $N_{side} = 1024$, the computed σ_{noise} value is within 0.5% of the value of σ_0 estimated from the time series (Jarosik et al. 2006). As we lower the resolution, the value of σ_{noise} slowly drops with pixel size. For W4, the channel with the large $1/f$ noise, this change is most dramatic; the value of σ_0 at resolution $N_{side} = 32$ is 6% higher than the value computed for $N_{side} = 1024$.

Figures 22 and 23 shows the one-point distribution function of the cleaned sky maps as a function of resolution. At the level of the one point function, the CMB sky appears to be Gaussian. This result is consistent with that from the area of hot and cold spots (one of the Minkowski functionals), which measures the cumulative one point probability function.

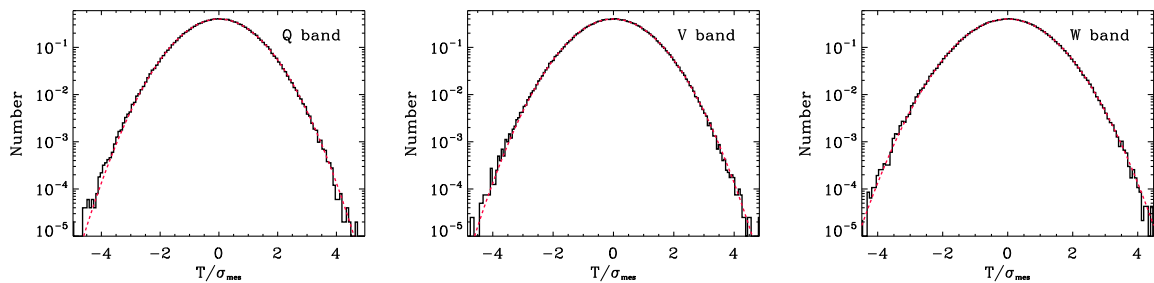


Fig. 22.— Normalized one point distribution function of temperature anisotropy, defined in equation (17), for the template-cleaned Q (left), V (middle) and W (right) band maps outside the Kp2 cut. The sky maps have been degraded to $N_{side} = 256$ for this figure. The red line shows a Gaussian distribution, which is an excellent fit to the one point distribution function.

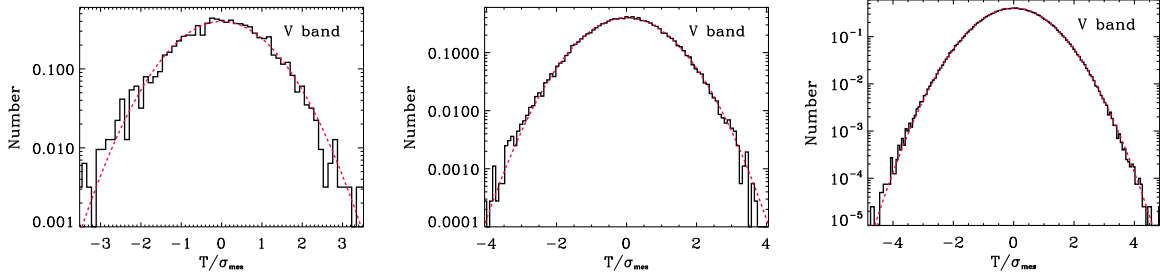


Fig. 23.— Normalized one point distribution function of temperature anisotropy, defined in equation (17), for the template-corrected V band data maps outside the Kp0 cut. The sky maps have been degraded to $N_{side} = 16$ (left), 64(middle) and 256(right) for this figure. The red line shows the best fit Gaussian, which is an excellent fit to the one point distribution function.

8.2. Size and Shape of Hot and Cold Spots

Minkowski functionals (Minkowski 1903; Gott et al. 1990; Schmalzing & Gorski 1998; Winitzki & Kosowsky 1998) measure the contour length, area, and number of hot and cold spots. Following the approach used in the first year analysis, we compute the Minkowski functionals as a function of temperature threshold, $\nu = \Delta T/\sigma$, where σ is the standard deviation of the map. For a two dimensional map, we measure three Minkowski functionals, the genus, $G(\nu)$, of the maps, the contour length, $C(\nu)$ and the area within the contours, $A(\nu)$.

We compare the measured values of the Minkowski functionals to their expected amplitude for a Gaussian sky. We simulate a series of maps based on the best fit parameters for Λ CDM and the WMAP noise patterns. For the analysis, we use the template-cleaned V+W maps outside the Kp0 sky mask region. Following the approach used in Komatsu et al. (2003), we compute the Minkowski functionals at 15 thresholds from -3.5σ to $+3.5\sigma$ and compare each functional to the simulations using a goodness of fit statistic,

$$\chi^2 = \sum_{\nu_1 \nu_2} [F_{WMAP}^i - \langle F_{sim}^i \rangle]_{\nu_1} \Sigma_{\nu_1 \nu_2}^{-1} [F_{WMAP}^i - \langle F_{sim}^i \rangle]_{\nu_2} \quad (18)$$

where F_{WMAP}^i is the Minkowski functional computed from the WMAP data, F_{sim}^i is the Minkowski functional computed from the simulated data, and $\Sigma_{\nu_1 \nu_2}$ is the bin-to-bin covariance from the simulations. Figure 24 shows the Minkowski functionals as a function of threshold for a map with $N_{side} = 128$ (28' pixels). These pixels are small enough to resolve the acoustic spots, but not so small as to be noise dominated. The figure shows that the contour length, area, and number of spots is consistent with expectations for a Gaussian theory.

Table 12 lists the probability of measuring the observed values of the Minkowski functionals as a function of pixel size. At all resolutions, the maps are consistent with Gaussian simulations.

We have also simulated non-Gaussian sky with non-Gaussian signals generated according to equation (16). By comparing these simulations to the data, we can constrain $f_{NL} = 7 \pm 66$ at the 68% confidence level, consistent with the bispectrum measurement (§8.3).

Table 12: χ^2 for Minkowski Functionals for 15 thresholds for the template-cleaned VW

Pixels	Minkowski	χ^2	DOF	$\langle Sim \rangle$	$F > WMAP$
128	Genus	20.9	15	15.4	0.17
128	Contour	19.2	15	15.1	0.19
128	Spot Area	14.0	15	15.3	0.54
128	Combined	51.6	45	47.2	0.31
64	Genus	18.3	15	14.9	0.24
64	Contour	19.3	15	14.9	0.19
64	Spot Area	8.4	15	15.5	0.93
64	Combined	50.0	45	47.2	0.36
32	Genus	17.3	15	15.4	0.31
32	Contour	27.8	15	15.8	0.04
32	Spot Area	8.5	15	15.8	0.89
32	Combined	43.8	45	49.1	0.61
16	Genus	28.2	15	15.8	0.05
16	Contour	19.0	15	15.7	0.29
16	Spot Area	14.1	15	15.6	0.47
16	Combined	84.6	45	49.4	0.03
8	Genus	10.8	15	15.5	0.62
8	Contour	24.3	15	16.0	0.09
8	Spot Area	28.8	15	15.0	0.05
8	Combined	100.5	45	49.0	0.03

8.3. Bispectrum

The bispectrum is sensitive to both primordial non-Gaussianity and various sources of secondary anisotropy (Spergel & Goldberg 1999; Goldberg & Spergel 1999; Komatsu & Spergel 2001). Here, we use the WMAP 3 year data to constrain the amplitude of primordial

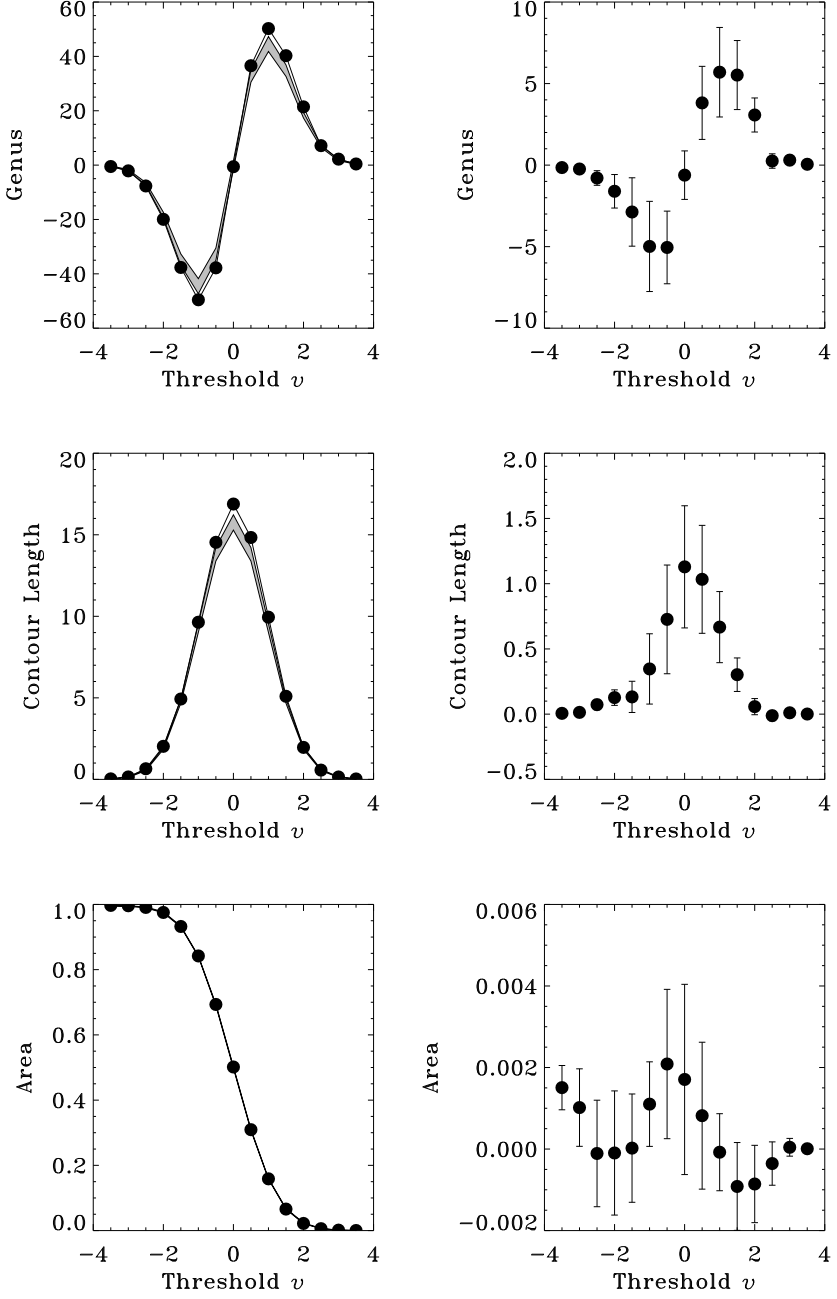


Fig. 24.— The WMAP data are in excellent agreement with the Gaussian simulations based on the analysis of the Minkowski functionals for the three year WMAP data outside the Kp0 cut. The filled circles in the left panel shows the values for the data at $N_{\text{side}} = 128$ (28' pixels). The gray band shows the 68% confidence interval for the Gaussian Monte Carlo simulations. The right panels show the residuals between the mean of the Gaussian simulations and the WMAP data. Note that the residuals are highly correlated from bin to bin, so the χ^2 are consistent with Gaussianity.

non-Gaussianity and to detect the amplitude of the point source signal in the cleaned Q, V and W band maps.

The amplitude of the primordial non-Gaussian signal can be found by computing a cubic statistic on the map (Komatsu et al. 2005):

$$S_{\text{primordial}} = \frac{1}{f_{\text{sky}}} \int 4\pi r^2 dr \int \frac{d^2\hat{n}}{4\pi} A(r, \hat{n}) B^2(r, \hat{n}) \quad (19)$$

where f_{sky} is the fraction of the sky used in the analysis, $B(r, \hat{n})$ is a Weiner filtered map of the primordial fluctuations and A is optimized to detect the form of the non-linearities. The amplitude of $S_{\text{primordial}}$ can be related directly to f_{NL} . Here, we use A and B as defined in (Komatsu et al. 2005). While we used $\ell_{\text{max}} = 265$ for the first-year analysis, we use $\ell_{\text{max}} = 350$ for the present analysis, as noise is significantly lower with three years of data. The error on f_{NL} begins to increase at $\ell_{\text{max}} > 350$ due to the presence of inhomogeneous noise. Note that Creminelli et al. (2005) argue that the optimal estimator for $S_{\text{primordial}}$ should include a term that is linear in temperature anisotropy as well as a cubic term that we already have in equation (19). They claim that their estimator could reduce the error on f_{NL} by about 20%. While their result is attractive, we shall not include the linear term in our analysis, as their estimator has not been tested against non-Gaussian simulations and thus it is not yet clear if it is unbiased.

Point sources are an expected cause of non-Gaussianity. Because point sources are not very correlated on the angular scales probed by WMAP, the point sources make a constant contribution to the bispectrum, b_{src} . Komatsu et al. (2005) develops a cubic statistic approach for computing b_{src} :

$$S_{ps} = \frac{1}{m_3} \int \frac{d^2\hat{n}}{4\pi} D^3(\hat{n}) \quad (20)$$

where $m_3 = (4\pi)^{-1} \int d^2\hat{n} M^3(\hat{n})$, $M(\hat{n}) = [\sigma_{\text{CMB}}^2 + N(\hat{n})]^{-1}$, and $D(\hat{n})$ is a match filter optimized for point source detection:

$$D(\hat{n}) = \sum_{\ell,m} \frac{b_\ell}{\tilde{C}_\ell} a_{lm} Y_{lm}(\hat{n}) \quad (21)$$

where b_ℓ is a beam transfer function and $\tilde{C}_\ell = C_\ell^{\text{cmb}} b_\ell^2 + N_\ell$. We weighted the temperature maps by $M(\hat{n})$ before we calculate a_{lm} . We use $\ell_{\text{max}} = 1024$ for calculating $D(\hat{n})$. (See § 3.2 of Komatsu et al. (2003) for details of weighting method.) Given the uncertainties in the source cut-off and the luminosity function, the values for b_{src} in Table 13 are consistent with the values of c_{ps} in Hinshaw et al. (2006).

Table 13 lists the measured amplitude of the non-Gaussian signals in the 3 year maps. The values are computed for template-cleaned Q, V and W band maps. With three years

of data, the limits on primordial non-Gaussianity have improved from $-58 < f_{NL} < 137$ to $-54 < f_{NL} < 114$ at the 95% confidence level. The improvement in limit on f_{NL} is roughly consistent with the expectation in the signal-dominated regime, $\Delta f_{NL} \propto l_{max}^{-1}$ (Komatsu & Spergel 2001). The level of point source non-Gaussianity in the 3 year maps is lower than in the first year maps. This drop is due to the more sensitive 3 year masks removing additional sources.

8.4. Trispectrum

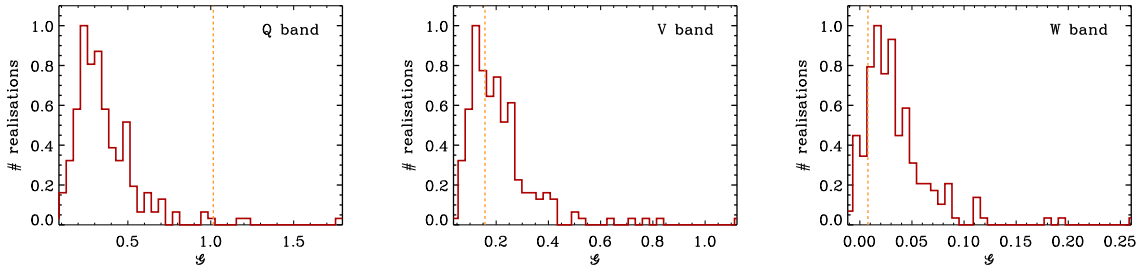


Fig. 25.— Constraints on the amplitude of four point function. The measured amplitude of the four point function (expressed in terms of a non-Gaussian amplitude defined in equation (23)) is compared to the same statistic computed for simulated Gaussian random fields. The yellow line shows the results for Q, V and W bands and the red histogram shows the distribution of the results of the Monte-Carlo realizations. Note that in both the simulations and the data A is greater than 0 due to the inhomogeneous noise. The excess in Q is may be due to point source contamination.

Table 13: Amplitude of Non-Gaussianity

	f_{NL}	b_{src} [$10^{-5} \mu\text{K}^3 \text{ sr}^2$]
Q	41 ± 55	4.8 ± 2.0
V	25 ± 50	0.12 ± 0.52
W	11 ± 50	-0.21 ± 0.34
V+W	18 ± 46	0.25 ± 0.26
Q+V+W	30 ± 42	0.73 ± 0.36

Motivated by claims that there are large scale variations in the amplitude of fluctuations, we consider a non-Gaussian model that generates a non-trivial four point function for the curvature (and temperature) fluctuations, but does not produce a three-point function. This model describes a cosmology where the value of one field modulates the amplitude of fluctuations in a second field:

$$\Phi(\vec{x}) = \phi(\vec{x})[1 + g_{NL}\psi(\vec{x})] \quad (22)$$

where ϕ and ψ are Gaussian random fields and Φ is the Bardeen curvature potential. The presence of such a term would generate variations in the amplitude of fluctuations across the sky.

Appendix B derives an estimator for the amplitude of non-Gaussian term, $g_{NL}^2|\psi|^2$. This estimator is based on approximating the CMB fluctuations as arising from an infinitely thin surface of last scatter. We measure the amplitude of the four point function by computing

$$\mathcal{G} = \sum_i (T_i^f \nabla^2 T_i^f - N_i^2)^2, \quad (23)$$

where T^f is a smoothed map (e.g., an $N_{side} = 128$ map), T_i is an unsmoothed map, and N_i is the expected value of $T_f \nabla^2 T_i$ for a map without any signal.

Figure 25 shows measurements of \mathcal{G} from the Q, V and W band data. V and W bands show any evidence for a non-trivial four point function, while Q band may show the contamination from point sources. At the S/N level of the 3 year data, there are no significant cosmological and systematic effects modulating the amplitude of the fluctuations as a function of scale.

8.5. CMB Modulation by Arbitrary Function

Among the many possibilities, we choose to address in a unifying manner the large scale “asymmetry”, “alignment” and low ℓ power issues discussed in the literature after the first year release (see for example Tegmark et al. (2003); de Oliveira-Costa et al. (2004); Eriksen et al. (2004b,a); Land & Magueijo (2005a,b)). We do so by testing the hypothesis that the observed temperature fluctuations, \tilde{T} , can be described as a Gaussian and isotropic random field modulated on large scales by an arbitrary function, namely

$$\tilde{T}(\hat{\mathbf{n}}) = T(\hat{\mathbf{n}})[1 + f(\hat{\mathbf{n}})] \quad (24)$$

where $f(\hat{\mathbf{n}})$ is a real and arbitrary modulation function and T is an isotropic Gaussian random field. If the observed sky is Gaussian and isotropic then f is equals to 0. If f were

a dipolar function, it would entail an isotropy breaking on large scales and an asymmetry along the dipole direction. If f were a quadrupolar function, then the quadrupolar and octopolar modes in the observed field would be aligned and the value of the lowest ℓ of the Gaussian field T would be influenced (Gordon et al. 2005). Note however that although those properties are interesting by themselves, the physical motivations for such a modulation are currently unclear. Modulation on large scales has been studied in great analytical details in Hajian & Souradeep (2003); Hajian et al. (2005); Prunet et al. (2005) and its physics and phenomenology investigated in Tomita (2005, 2006) and Gordon et al. (2005).

To test this hypothesis, we first expand $f(\hat{\mathbf{n}})$ in spherical harmonics

$$f(\hat{\mathbf{n}}) = \sum_{\ell=1}^{\ell_{max}} \sum_{m=-m}^m f_{\ell m} Y_{\ell m}(\hat{\mathbf{n}}) \quad (25)$$

with either $\ell_{max} = 1$ or $\ell_{max} = 2$. We then study the probability that f is different from 0 in a Bayesian framework. To do so we consider the likelihood function $L(\tilde{T}|f_{\ell m}, C_{\ell})$, where C_{ℓ} is the angular power spectrum of the Gaussian field T , and solve for the maximum of this likelihood using a Markov Chain Monte Carlo solver. The likelihood is computed exactly in pixel space. We restrict ourselves to the region outside the Kp2 mask to avoid any spurious galactic contamination and we work at res 3 ($N_{side} = 8$). Details of the likelihood computation are presented in the Appendix C. We use as inputs the template-cleaned Q, V and W maps.

We tested this approach on simulations by studying either a pure Gaussian field or a Gaussian field modulated by a field of the above form with power up to $\ell_{max} = 1$ or $\ell_{max} = 2$ set to a realistic amplitude. We checked that in both cases our maximum likelihood estimator recovers the input $f_{\ell m}$ and C_{ℓ} , whether the ℓ_{max} assumed in the measurement is higher or lower than the input ones.

We then applied to the data our method and the results are the following. We quote here numbers coming from the maps combining the three years of data from V band only, but similar results were obtained using either the Q or W band. The maximum likelihood peaks as well as marginalized values for the $f_{\ell m}$ s with 95% error values are given in Table 14. Note that some important degeneracies are observed between $C_{1,2,3}$ and the $f_{\ell m}$ s.

Whereas mild deviations from 0 are observed, the change in $\ln L$ when compared to the case where $f = 0$ and only C_{ℓ} s are varied is $\Delta \ln L = -1.7$ for $\ell_{max} = 1$ (*i.e.* , 3 extra parameters) and $\Delta \ln L = -3.98$ for $\ell_{max} = 2$ (*i.e.* , 8 extra parameters.)

Figure 26 shows the best fit form for f : an axis lying near the ecliptic plane. This is the same feature that has been identified in a number of papers on non-Gaussianity. If

Table 14: Maximum likelihood peak values and 1D marginalized values for the $f_{\ell m}$ s for $\ell_{max} = 1$ and $\ell_{max} = 2$ using the V band only.

$\ell_{max} = 1$	f_{10}	f_{11}
	$(-0.104, 0.000)$	$(0.117, 0.054)$
	$(-0.057_{-0.225}^{+0.119}, 0.000)$	$(0.127_{-0.268}^{+0.014}, -0.053_{-0.087}^{+0.185})$
$\ell_{max} = 2$	f_{10}	f_{11}
	$(-0.032, 0.0)$	$(0.141, -0.068)$
	$(-0.020_{-0.201}^{+0.133}, 0.0)$	$(0.145_{-0.264}^{-0.002}, -0.061_{-0.068}^{+0.179})$
	f_{20}	f_{21}
	$(-0.0283, 0.00)$	$(-0.0570, -0.089)$
	$(-0.028_{-0.214}^{+0.172}, 0.0)$	$(0.129, -0..036)$ $(0.105_{-0.002}^{+0.242}, -0.045_{-0.098}^{+0.165})$
	f_{21}	f_{22}

instead of trying to fit all 8 modes, we had chosen to look for a preferred axis, then we would have made the *a posteriori* choice to search for non-Gaussianity with a $\delta\chi^2$ of 8. If we were eager to claim evidence of strong non-Gaussianity, we could quote the probability of this occurring randomly as less than 2%. We, however, do not interpret the improvement of $\Delta\chi^2 = 8$ with 8 additional parameters as evidence against the hypothesis that the primordial fluctuations are Gaussian. Since the existence of non-Gaussian features in the CMB would require dramatic reinterpretation of our theories of primordial fluctuations, more compelling evidence is required.

9. Conclusions

The standard model of cosmology has survived another rigorous set of tests. The errors on the WMAP data at large ℓ are now three times smaller and there has been significant improvements in other cosmological measurements. Despite the overwhelming force of the data, the model continues to thrive.

The data are so constraining that there is little room for significant modifications of the basic Λ CDM model. The combination of WMAP measurements and other astronomical measurements place significant limits on the geometry of the universe, the nature of dark energy, and even neutrino properties. While allowing for a running spectral index slightly improves the fit to the WMAP data, the improvement in the fit is not significant enough to require a new parameter.

Cosmology requires new physics beyond the standard model of particle physics: dark matter, dark energy and a mechanism to generate primordial fluctuations. The WMAP data provides insights into all three of these fundamental problems:

- The clear detection of the predicted acoustic peak structure implies that the dark matter is non-baryonic.
- The WMAP data are consistent with nearly flat universe in which the dark energy has an equation of state close to that of a cosmological constant, $w = -1$. The combination of WMAP data with measurements of the Hubble Constant, baryon oscillations, supernova data and large-scale structure observations all reinforces the evidence for dark energy.
- The simplest model for structure formation, a scale-invariant spectrum of fluctuations, is not a good fit to the WMAP data. The WMAP data requires either tensor modes or a spectral index with $n_s < 1$ to fit the angular power spectrum. These observations match the basic inflationary predictions and are well fit by the predictions of the simple $m^2\phi^2$ model.

Further WMAP observations and future analyses will test the inflationary paradigm. While we do not find convincing evidence for significant non-Gaussianities, an alternative model that better fits the low ℓ data would be an exciting development. Within the context of the inflationary models, measurements of the spectral index as a function of scale and measurements of tensor modes directly will provide a direct probe into the physics of the first moments of the big bang.

10. Acknowledgments

The WMAP mission is made possible by the support of the Office of Space Sciences at NASA Headquarters and by the hard and capable work of scores of scientists, engineers, technicians, machinists, data analysts, budget analysts, managers, administrative staff, and reviewers. We thank Joanna Dunkley for comments on the draft, Henk Hoekstra, Yannick Mellier and Ludovic Van Waerbeke for providing the CFHTLS data and discussions of the lensing data, John Sievers for discussions of small-scale CMB experiments, Adam Riess and Kevin Krisciunis for discussion of supernova data, Daniel Eisenstein for discussion of the SDSS LRG data, Max Tegmark for discussions of SDSS P(k) data, and John Peacock for discussions about the 2dFGRS data. EK acknowledges support from an Alfred P. Sloan Research Fellowship. HVP is supported by NASA through Hubble Fellowship grant

#HF-01177.01-A awarded by the Space Telescope Science Institute which is operated by the Association of Universities for Research in Astronomy, Inc., for NASA under contract NAS 5-26555. This research has made use of NASA’s Astrophysics Data System Bibliographic Services, the HEALPix software, CAMB software, and the CMBFAST software. CosmoMC (Lewis & Bridle 2002) was used to produce Figures 1 and 27. We also used and CMBWARP software (Jimenez et al. 2004) for initial investigations of the parameter space. This research was additionally supported by NASA LTSA03-000-0090, NASA ATPNNG04GK55G, and NASA ADP03-0000-092 awards.

REFERENCES

Abazajian, K., et al. 2005, *ApJ*, 625, 613

Abroe, M. E., et al. 2004, *ApJ*, 605, 607

Afshordi, N. 2004, *Phys. Rev. D*, 70, 083536

Afshordi, N., Lin, Y.-T., & Sanderson, A. J. R. 2005, *ApJ*, 629, 1

Afshordi, N., Loh, Y.-S., & Strauss, M. A. 2004, *Phys. Rev.*, D69, 083524

Albrecht, A. & Steinhardt, P. J. 1982, *Phys. Rev. Lett.*, 48, 1220

Alishahiha, M., Silverstein, E., & Tong, D. 2004, *Phys. Rev. D*, 70, 123505

Allen, S. W., Schmidt, R. W., Ebeling, H., Fabian, A. C., & van Speybroeck, L. 2004, ArXiv Astrophysics e-prints

Allen, S. W., Schmidt, R. W., Fabian, A. C., & Ebeling, H. 2003, *MNRAS*, 342, 287

Amendola, L. 1999, *Phys. Rev. D*, 60, 043501

Arkani-Hamed, N., Creminelli, P., Mukohyama, S., & Zaldarriaga, M. 2004, *Journal of Cosmology and Astro-Particle Physics*, 4, 1

Asplund, M., Nissen, P. E., Lambert, D. L., Primas, F., & Smith, V. V. 2005, in IAU Symposium, ed. V. Hill, P. François, & F. Primas, 53–58

Astier, P., et al. 2005, ArXiv Astrophysics e-prints

Aurich, R., Lustig, S., Steiner, F., & Then, H. 2005, *Physical Review Letters*, 94, 021301

Babich, D., Creminelli, P., & Zaldarriaga, M. 2004, Journal of Cosmology and Astro-Particle Physics, 8, 9

Bahcall, N. A. & Bode, P. 2003, ApJ, 588, L1

Bahcall, N. A., Ostriker, J. P., Perlmutter, S., & Steinhardt, P. J. 1999, Science, 284, 1481

Bania, T. M., Rood, R. T., & Balser, D. S. 2002, Nature, 415, 54

Bardeen, J. M., Bond, J. R., Kaiser, N., & Szalay, A. S. 1986, ApJ, 304, 15

Bardeen, J. M., Steinhardt, P. J., & Turner, M. S. 1983, Phys. Rev. D, 28, 679

Barger, V., Kneller, J. P., Lee, H.-S., Marfatia, D., & Steigman, G. 2003, Phys. Lett., B566, 8

Barger, V., Marfatia, D., & Tregre, A. 2004, Phys. Lett., B595, 55

Bartelmann, M. & Schneider, P. 2001, Phys. Rep., 340, 291

Bartolo, N., Komatsu, E., Matarrese, S., & Riotto, A. 2004a, ArXiv Astrophysics e-prints

Bartolo, N., Matarrese, S., & Riotto, A. 2004b, Journal of High Energy Physics, 4, 6

Bashinsky, S. & Seljak, U. 2004, Phys. Rev. D, 69, 083002

Bean, R. & Dore, O. 2004, Phys. Rev., D69, 083503

Bean, R. & Magueijo, J. 2001, Phys. Lett., B517, 177

Beltrán, M., García-Bellido, J., Lesgourgues, J., Liddle, A. R., & Slosar, A. 2005, Phys. Rev. D, 71, 063532

Bennett, C. L., et al. 2003, ApJS, 148, 1

Bergström, L. & Danielsson, U. H. 2002, Journal of High Energy Physics, 12, 38

Blanchard, A., Douspis, M., Rowan-Robinson, M., & Sarkar, S. 2003, Astron. Astrophys., 412, 35

Boesgaard, A. M., Stephens, A., & Deliyannis, C. P. 2005, ApJ, 633, 398

Bond, J. R. & Efstathiou, G. 1984, ApJ, 285, L45

Bond, J. R. & Efstathiou, G. 1987, MNRAS, 226, 655

Bond, J. R., Efstathiou, G., & Silk, J. 1980, Physical Review Letters, 45, 1980

Bond, J. R., Pogosyan, D., & Souradeep, T. 2000, Phys. Rev. D, 62, 043005

Bond, J. R. & Szalay, A. S. 1983, ApJ, 274, 443

Bond, J. R., et al. 2005, ApJ, 626, 12

Borgani, S., et al. 2001, ApJ, 561, 13

Boughn, S. & Crittenden, R. 2004, Nature, 427, 45

Boughn, S. P. & Crittenden, R. G. 2005, MNRAS, 360, 1013

Bowen, R., Hansen, S. H., Melchiorri, A., Silk, J., & Trotta, R. 2002, MNRAS, 334, 760

Bridle, S. L., Lewis, A. M., Weller, J., & Efstathiou, G. P. 2003,, New Astronomy Reviews, 47, 787

Bridges, M., Lasenby, A. N., & Hobson, M. P. 2005, ArXiv Astrophysics e-prints

Bucher, M. & Spergel, D. 1999, Phys. Rev. D, 60, 043505

Burgess, C. P., Cline, J. M., Lemieux, F., & Holman, R. 2003, Journal of High Energy Physics, 2, 48

Cabella, P., Hansen, F., Marinucci, D., Pagano, D., & Vittorio, N. 2004, Phys. Rev. D, 69, 063007

Caldwell, R. R., Dave, R., & Steinhardt, P. J. 1998, Phys. Rev. Lett., 80, 1582

Carroll, S. M., Press, W. H., & Turner, E. L. 1992, ARA&A, 30, 499

Cen, R. 2003, Astrophys. J., 591, L5

Chaboyer, B. & Krauss, L. M. 2002, ApJ, 567, L45

Chae, K.-H., et al. 2002, Physical Review Letters, 89, 151301

Charbonnel, C. & Primas, F. 2005, A&A, 442, 961

Chiang, L., Naselsky, P. D., Verkhodanov, O. V., & Way, M. J. 2003, ApJ, 590, L65

Chiu, W. A., Fan, X. & Ostriker, J. P. 2003, ApJ, 599, 759.

Ciardi, B., Ferrara, A., & White, S. D. M. 2003, Mon. Not. Roy. Astron. Soc., 344, L7

Clocchiatti, A., et al. 2005, ArXiv Astrophysics e-prints

Coc, A., Vangioni-Flam, E., Descouvemont, P., Adahchour, A., & Angulo, C. 2004, ApJ, 600, 544

Cole, S., et al. 2005, MNRAS, 362, 505

Colley, W. N. & Gott, J. R. 2003, MNRAS, 344, 686

Contaldi, C. R., Hoekstra, H., & Lewis, A. 2003, Phys. Rev. Lett., 90, 221303

Copi, C. J., Huterer, D., & Starkman, G. D. 2003, ArXiv Astrophysics e-prints

Corasaniti, P.-S., Giannantonio, T., & Melchiorri, A. 2005, Phys. Rev. D, 71, 123521

Cornish, N. J., Spergel, D. N., & Starkman, G. D. 1996, Physical Review Letters, 77, 215

Cornish, N. J., Spergel, D. N., Starkman, G. D., & Komatsu, E. 2004, Physical Review Letters, 92, 201302

Creminelli, P., Nicolis, A., Senatore, L., Tegmark, M., & Zaldarriaga, M. 2005, ArXiv Astrophysics e-prints

Crighton, N. H. M., Webb, J. K., Ortiz-Gil, A., & Fernández-Soto, A. 2004, MNRAS, 355, 1042

Crittenden, R. G. & Turok, N. 1996, Physical Review Letters, 76, 575

Croft, R. A. C., Weinberg, D. H., Katz, N., & Hernquist, L. 1998, ApJ, 495, 44

Crotty, P., Lesgourgues, J., & Pastor, S. 2003, Phys. Rev., D67, 123005

Cruz, M., Martínez-González, E., Vielva, P., & Cayón, L. 2005, MNRAS, 356, 29

Danielsson, U. H. 2002, Phys. Rev. D, 66, 023511

Desjacques, V. & Nusser, A. 2005, MNRAS, 361, 1257

de Oliveira-Costa, A., Tegmark, M., Zaldarriaga, M., & Hamilton, A. 2004, Phys. Rev. D, 69, 063516

Deffayet, C., Dvali, G., Gabadadze, G., & Lue, A. 2001, Phys. Rev. D, 64, 104002

Dickinson, C., et al. 2004, MNRAS, 353, 732

Dunlop, J., Peacock, J., Spinrad, H., Dey, A., Jimenez, R., Stern, D., & Windhorst, R. 1996, *Nature*, 381, 581

Dvali, G., Gruzinov, A., & Zaldarriaga, M. 2004, *Phys. Rev. D*, 69, 083505

Easther, R., Greene, B. R., Kinney, W. H., & Shiu, G. 2002, *Phys. Rev. D*, 66, 023518

Easther, R., Kinney, W. H., & Peiris, H. 2005a, *Journal of Cosmology and Astro-Particle Physics*, 8, 1

—. 2005b, *Journal of Cosmology and Astro-Particle Physics*, 5, 9

Efstathiou, G. 2004, *MNRAS*, 348, 885

Eisenstein, D. J., et al. 2005, *ApJ*, 633, 560

Elgarøy, Ø. & Lahav, O. 2003, *Journal of Cosmology and Astro-Particle Physics*, 4, 4

Ellis, J., Olive, K. A., & Vangioni, E. 2005, *Physics Letters B*, 619, 30

Eriksen, H. K., Banday, A. J., Górski, K. M., & Lilje, P. B. 2004a, *ApJ*, 612, 633

Eriksen, H. K., Hansen, F. K., Banday, A. J., Górski, K. M., & Lilje, P. B. 2004b, *ApJ*, 605, 14

Ettori, S., Tozzi, P., & Rosati, P. 2003, *A&A*, 398, 879

Fan, X., et al. 2005, ArXiv Astrophysics e-prints

Feldman, H., et al. 2003, *ApJ*, 596, L131

Ferreira, P. G. & Joyce, M. 1998, *Phys. Rev. D*, 58, 023503

Fields, B. D., Olive, K. A., & Vangioni-Flam, E. 2005, *ApJ*, 623, 1083

Fosalba, P. & Gaztañaga, E. 2004, *MNRAS*, 350, L37

Freedman, W. L., et al. 2001, *ApJ*, 553, 47

Gaztañaga, E. & Wagg, J. 2003, *Phys. Rev. D*, 68, 021302

Gelman, A. & Rubin, D. 1992, *Statistical Science*, 7, 457

Gnedin, N. Y. & Gnedin, O. Y. 1998, *ApJ*, 509, 11

Gnedin, N. Y. & Hamilton, A. J. S. 2002, *MNRAS*, 334, 107

Goldberg, D. M. & Spergel, D. N. 1999, Phys. Rev. D, 59, 103002

Goobar, A., Hannestad, S., Mortsell, E., & Tu, H. 2006, ArXiv Astrophysics e-prints

Gordon, C., Hu, W., Huterer, D., & Crawford, T. 2005, Phys. Rev. D, 72, 103002

Gott, J. R. I., Park, C., Juszkiewicz, R., Bies, W. E., Bennett, D. P., Bouchet, F. R., & Stebbins, A. 1990, ApJ, 352, 1

Grainge, K., et al. 2003, MNRAS, 341, L23

Guth, A. H. 1981, Phys. Rev. D, 23, 347

Guth, A. H. & Pi, S. Y. 1982, Phys. Rev. Lett., 49, 1110

Haiman, Z. & Holder, G. P. 2003, Astrophys. J., 595, 1

Hajian, A. & Souradeep, T. 2003, Astrophys. J., 597, L5

Hajian, A., Souradeep, T., & Cornish, N. 2005, ApJ, 618, L63

Hall, L. J. & Oliver, S. 2004, Nuclear Physics B Proceedings Supplements, 137, 269

Hall, L. M. H., Moss, I. G., & Berera, A. 2004, Phys. Rev., D69, 083525

Hamuy, M., Phillips, M. M., Suntzeff, N. B., Schommer, R. A., Maza, J., & Aviles, R. 1996, AJ, 112, 2391

Hannestad, S. 2001, Phys. Rev. D, 64, 083002

—. 2003, Journal of Cosmology and Astro-Particle Physics, 5, 4

—. 2005, ArXiv Astrophysics e-prints

Hansen, F. K., Cabella, P., Marinucci, D., & Vittorio, N. 2004, ApJ, 607, L67

Hansen, B. M. S., et al. 2004, ApJS, 155, 551

Hawking, S. W. 1982, Phys. Lett., B115, 295

Henry, J. P. 2004, ApJ, 609, 603

Heymans, C., et al. 2005, MNRAS, 361, 160

Hinshaw, G., et al. 2003, ApJS, 148, 135

Hinshaw, G. et al. 2006, ApJ, submitted

Hoekstra, H., Yee, H. K. C., & Gladders, M. D. 2002, ApJ, 577, 595

Hoekstra, H., et al. 2005, ArXiv Astrophysics e-prints

Hoffman, M. B. & Turner, M. S. 2001, Phys. Rev., D64, 023506

Hu, W. 1998, ApJ, 506, 485

Hu, W. 2001, in RESCEU: 1999: Birth and Evolution of the Universe, 131

Hu, W., Eisenstein, D. J., & Tegmark, M. 1998, Phys. Rev. Lett., 80, 5255

Hu, W., Fukugita, M., Zaldarriaga, M., & Tegmark, M. 2001, ApJ, 549, 669

Hu, W. & Holder, G. P. 2003, Phys. Rev., D68, 023001

Huffenberger, K. M., Seljak, U., & Makarov, A. 2004, Phys. Rev. D, 70, 063002

Hwang, J. & Noh, H. 1998, Physical Review Letters, Volume 81, Issue 24, December 14, 1998, pp.5274-5277, 81, 5274

Ichikawa, K., Fukugita, M., & Kawasaki, M. 2005, Phys. Rev. D, 71, 043001

Iliev, I. T., Mellema, G., Pen, U.-L., Merz, H., Shapiro, P. R., & Alvarez, M. A. 2005, ArXiv Astrophysics e-prints

Inoue, K. T., Tomita, K., & Sugiyama, N. 2000, MNRAS, 314, L21

Jarosik, N. et al. 2006, ApJ, submitted

Jarvis, M., Bernstein, G. M., Fischer, P., Smith, D., Jain, B., Tyson, J. A., & Wittman, D. 2003, AJ, 125, 1014

Jassal, H. K., Bagla, J. S., & Padmanabhan, T. 2005, Phys. Rev. D72, 103503 (2005).

Jena, T., et al. 2005, MNRAS, 361, 70

Jimenez, R., Verde, L., Peiris, H., & Kosowsky, A. 2004, Phys. Rev., D70, 023005

Jimenez, R., Verde, L., Treu, T., & Stern, D. 2003, Astrophys. J., 593, 622

Jones, W. C., et al. 2005, ArXiv Astrophysics e-prints

Kaloper, N., Kleban, M., Lawrence, A., Shenker, S., & Susskind, L. 2002, Journal of High Energy Physics, 11, 37

Kaplinghat, M., Chu, M., Haiman, Z., Holder, G. P., Knox, L., & Skordis, C. 2003, ApJ, 583, 24

Khoury, J., Ovrut, B. A., Seiberg, N., Steinhardt, P. J., & Turok, N. 2002, Phys. Rev., D65, 086007

Khoury, J., Ovrut, B. A., Steinhardt, P. J., & Turok, N. 2001, Phys. Rev., D64, 123522

Kinney, W. H. 2002, Phys. Rev., D66, 083508

Kirkman, D., Tytler, D., Suzuki, N., O'Meara, J. M., & Lubin, D. 2003, ApJS, 149, 1

Knop, R. A., et al. 2003, ApJ, 598, 102

Knox, L., Christensen, N., & Skordis, C. 2001, ApJ, 563, L95

Kogo, N., Matsumiya, M., Sasaki, M., & Yokoyama 2004, ApJ, 607, 32

Kogo, N. & Komatsu, E. 2006, ArXiv Astrophysics e-prints

Kogut, A., et al. 2003, ApJS, 148, 161

Komatsu, E. 2001, ArXiv Astrophysics e-prints, ph.D. thesis at Tohoku University (astro-ph/0206039)

Komatsu, E. & Futamase, T. 1999, Phys. Rev., D59, 064029

Komatsu, E. & Kitayama, T. 1999, ApJ, 526, L1

Komatsu, E. & Seljak, U. 2001, MNRAS, 327, 1353

—. 2002, MNRAS, 336, 1256

Komatsu, E. & Spergel, D. N. 2001, Phys. Rev. D, 63, 63002

Komatsu, E., Spergel, D. N., & Wandelt, B. D. 2005, ApJ, 634, 14

Komatsu, E., et al. 2003, ApJS, 148, 119

Koopmans, L. V. E., Treu, T., Fassnacht, C. D., Blandford, R. D., & Surpi, G. 2003, ApJ, 599, 70

Kosowsky, A., Milosavljevic, M., & Jimenez, R. 2002, Phys. Rev. D, 66, 63007

Krisciunas, K., et al. 2005, AJ, 130, 2453

Kuo, C. L., et al. 2004, ApJ, 600, 32

Lahav, O., Rees, M. J., Lilje, P. B., & Primack, J. R. 1991, MNRAS, 251, 128

Land, K. & Magueijo, J. 2005a, Phys. Rev. D, 72, 101302

—. 2005b, MNRAS, 362, L16

Larena, J., Alimi, J.-M., & Serna, A. 2005, ArXiv Astrophysics e-prints

Leach, S. M., Liddle, A. R., Martin, J., & Schwartz, D. J. 2002, Phys. Rev. D, 66, 023515

Leach, S. M. & Liddle, A. R. 2003, Phys. Rev. D, 68, 123508

Leitch, E. M., Kovac, J. M., Halverson, N. W., Carlstrom, J. E., Pryke, C., & Smith, M. W. E. 2005, ApJ, 624, 10

Levin, J. J., Barrow, J. D., Bunn, E. F., & Silk, J. 1997, Physical Review Letters, 79, 974

Lewis, A. & Bridle, S. 2002, Phys. Rev. D, 66, 103511

Lewis, A., Challinor, A., & Lasenby, A. 2000, ApJ, 538, 473

Liddle, A. R. & Lyth, D. H. 1992, Phys. Lett., B291, 391

—. 1993, Phys. Rept., 231, 1

Linde, A. D. 1982, Phys. Lett., B108, 389

Linde, A. D. 1983, Phys. Lett., B129, 177

Linde, A. 2005, New Astronomy Review, 49, 35

Luminet, J., Weeks, J. R., Riazuelo, A., Lehoucq, R., & Uzan, J. 2003, Nature, 425, 593

Lyth, D. H. & Riotto, A. 1999, Phys. Rept., 314, 1

Lyth, D. H., Ungarelli, C., & Wands, D. 2003, Phys. Rev. D, 67, 23503

Ma, C.-P. 1996, ApJ, 471, 13

Madau, P., Rees, M. J., Volonteri, M., Haardt, F., & Oh, S. P. 2004, Astrophys. J., 604, 484

Maldacena, J. 2003, Journal of High Energy Physics, 5, 13

Malhotra, S. & Rhoads, J. E. 2004, ApJ, 617, L5

Martin, J. & Brandenberger, R. 2003, Phys. Rev. D, 68, 063513

Martin, J. & Brandenberger, R. H. 2001, Phys. Rev. D, 63, 123501

Martin, J. & Ringeval, C. 2004, Phys. Rev. D, 69, 083515

Mason, B. S., et al. 2003, ApJ, 591, 540

Mathews, G. J., Kajino, T., & Shima, T. 2005, Phys. Rev. D, 71, 021302

McDonald, P., et al. 2005, ApJ, 635, 761

McGaugh, S. S. 2004, ApJ, 611, 26

Meiksin, A. & White, M. 2004, MNRAS, 350, 1107

Meléndez, J. & Ramírez, I. 2004, ApJ, 615, L33

Minkowski, H. 1903, Mathematische Annalen, 57, 447

Mohapatra, R. N., et al. 2005, hep-ph

Montroy, T. E., et al. 2005, ApJ

Mukhanov, V. F. & Chibisov, G. V. 1981, JETP Letters, 33, 532

Mukherjee, P., Parkinson, D., & Liddle, A. R. 2006, ApJ, 638, L51

Mukherjee, P. & Wang, Y. 2003, ApJ, 599, 1

Mukherjee, P. & Wang, Y. 2003, ApJ, 613, 51

Nagai, D. 2005, ArXiv Astrophysics e-prints

Naselsky, P. D., Chiang, L.-Y., Novikov, I. D., & Verkhodanov, O. V. 2005, International Journal of Modern Physics D, 14, 1273

Nobili, S., et al. 2005, A&A, 437, 789

Nolta, M. R., et al. 2004, Astrophys. J., 608, 10

Novosyadlyj, B., Durrer, R., & Lukash, V. N. 1999, A&A, 347, 799

O'Dwyer, I. J. et al. 2004, Astrophys. J., 617, L99

O'Dwyer, I. J., et al. 2005, ApJS, 158, 93

Oguri, M. 2004, ArXiv Astrophysics e-prints

Oh, S. P. & Haiman, Z. 2003, Mon. Not. Roy. Astron. Soc., 346, 456

Okamoto, T. & Lim, E. A. 2004, Phys. Rev. D, 69, 083519.

Olive, K. A. & Skillman, E. D. 2004, ApJ, 617, 29

Ostriker, J. P. & Steinhardt, P. J. 1995, Nature, 377, 600

Padmanabhan, N., Hirata, C. M., Seljak, U., Schlegel, D. J., Brinkmann, J., & Schneider, D. P. 2005, Phys. Rev. D, 72, 043525

Page, L., et al. 2003a, ApJS, 148, 39

—. 2003b, ApJS, 148, 233

Page, L. et al. 2006, ApJ, submitted

Park, C. 2004, MNRAS, 349, 313

Pearson, T. J., et al. 2003, ApJ, 591, 556

Peebles, P. J. & Ratra, B. 2003, Reviews of Modern Physics, 75, 559

Peebles, P. J. E. 1984, ApJ, 284, 439

Peebles, P. J. E. & Ratra, B. 1988, ApJ, 325, L17

Peebles, P. J. E. & Yu, J. T. 1970, ApJ, 162, 815

Peiris, H. V., et al. 2003, ApJS, 148, 213

Pen, U. 1997, New Astronomy, 2, 309

Perlmutter, S., et al. 1999, ApJ, 517, 565

Phillips, M. M. 1993, ApJ, 413, L105

Phillips, N. G. & Kogut, A. 2004, ArXiv Astrophysics e-prints

Piacentini, F., et al. 2005, ArXiv Astrophysics e-prints

Pierpaoli, E. 2003, Mon. Not. Roy. Astron. Soc., 342, L63

Pierpaoli, E., Borgani, S., Scott, D., & White, M. 2003, MNRAS, 342, 163

Pogosian, L., Corasaniti, P. S., Stephan-Otto, C., Crittenden, R., & Nichol, R. 2005, Phys. Rev. D, 72, 103519

Prunet, S., Uzan, J.-P., Bernardeau, F., & Brunier, T. 2005, Phys. Rev. D, 71, 083508

Rasia, E., Mazzotta, P., Borgani, S., Moscardini, L., Dolag, K., Tormen, G., Diaferio, A., & Murante, G. 2005, ApJ, 618, L1

Readhead, A. C. S., et al. 2004a, ApJ, 609, 498

—. 2004b, Science, 306, 836

Refregier, A. 2003, ARA&A, 41, 645

Refregier, A., Komatsu, E., Spergel, D. N., & Pen, U. 2000, Phys. Rev. D, 61, 123001

Reid, B. A. & Spergel, D. N. 2006, ArXiv Astrophysics e-prints

Richard, O., Michaud, G., & Richer, J. 2005, ApJ, 619, 538

Richer, H. B., et al. 2004, AJ, 127, 2771

Ricotti, M. & Ostriker, J. P. 2004, MNRAS, 352, 547

Riess, A. G., Press, W. H., & Kirshner, R. P. 1996, ApJ, 473, 88

Riess, A. G., et al. 1998, AJ, 116, 1009

—. 2004, ApJ, 607, 665

Riess, A. G. et al. 2004, Astrophys. J., 607, 665

Riess, A. G., et al. 2005, ApJ, 627, 579

Ruhl, J. E., et al. 2003, ApJ, 599, 786

Sato, K. 1981, MNRAS, 195, 467

Schmalzing, J. & Gorski, K. M. 1998, MNRAS, 297, 355

Schmidt, B. P., et al. 1998, ApJ, 507, 46

Schwarz, D. J., Terrero-Escalante, C. A., & Garcia, A. A. 2001, Physics Letters B, 517, 243

Schwarz, D. J., & Terrero-Escalante, C. A. 2004, JCAP, 0408, 003

Scranton, R. et al. 2003, ArXiv Astrophysics e-prints

Seljak, U., et al. 2005a, Phys. Rev. D, 71, 103515

—. 2005b, Phys. Rev. D, 71, 043511

Semboloni, E., et al. 2005, ArXiv Astrophysics e-prints

Serebrov, A., et al. 2005, Physics Letters B, 605, 72

Sievers, J. L., et al. 2003, ApJ, 591, 599

Simon, J., Verde, L., & Jimenez, R. 2005, Phys. Rev. D, 71, 123001

Skordis, C., Mota, D. F., Ferreira, P. G., & Boehm, C. 2006, Physical Review Letters, 96, 011301

Slosar, A., Seljak, U., & Makarov, A. 2004, Phys. Rev., D69, 123003

Slosar, A., et al. 2003, MNRAS, 341, L29

Smith, R. E., et al. 2003, MNRAS, 341, 1311

Sokasian, A., Yoshida, N., Abel, T., Hernquist, L., & Springel, V. 2004, MNRAS, 350, 47

Somerville, R. S. & Livio, M. 2003, Astrophys. J., 593, 611

Soucail, G., Kneib, J.-P., & Golese, G. 2004, A&A, 417, L33

Spergel, D. N. & Goldberg, D. M. 1999, Phys. Rev. D, 59, 103001

Spergel, D. N., et al. 2003, ApJS, 148, 175

Starobinsky, A. A. 1980, Phys. Lett., B 91, 99

Starobinsky, A. A. 1982, Phys. Lett., B117, 175

Steigman, G. 2005, ArXiv Astrophysics e-prints

Sunyaev, R. A. & Zel'dovich, Y. B. 1970, Ap&SS, 7, 3

Takada, M., Komatsu, E., & Futamase, T. 2005, ArXiv Astrophysics e-prints

Tegmark, M., de Oliveira-Costa, A., & Hamilton, A. J. 2003, Phys. Rev. D, 68, 123523

Tegmark, M., Zaldarriaga, M., & Hamilton, A. J. 2001, Phys. Rev. D, 63, 043007

Tegmark, M., et al. 2004a, Phys. Rev. D, 69, 103501

—. 2004b, *ApJ*, 606, 702

Tereno, I., Doré, O., van Waerbeke, L., & Mellier, Y. 2005, *A&A*, 429, 383

Tomita, K. 2005, *Phys. Rev. D*, 72, 103506

—. 2006, *Phys. Rev. D*, 73, 029901

Tonry, J. L., et al. 2003, *ApJ*, 594, 1

Totani, T., Kawai, N., Kosugi, G., Aoki, K., Yamada, T., Iye, M., Ohta, K., & Hattori, T. 2005, ArXiv Astrophysics e-prints

Trotta, R. 2005, ArXiv Astrophysics e-prints

Turner, E. L. 1990, *ApJ*, 365, L43

Turner, M. S., Steigman, G., & Krauss, L. M. 1984, *Physical Review Letters*, 52, 2090

Vale, A. & Ostriker, J. P. 2005, ArXiv Astrophysics e-prints

Van Waerbeke, L. & Mellier, Y. prep, ArXiv Astrophysics e-prints

Van Waerbeke, L., Mellier, Y., & Hoekstra, H. 2005, *A&A*, 429, 75

Verde, L., et al. 2002, *MNRAS*, 335, 432

—. 2003, *ApJS*, 148, 195

Vielva, P., Martínez-González, E., Barreiro, R. B., Sanz, J. L., & Cayón, L. 2004, *ApJ*, 609, 22

Vielva, P., Martínez-González, E., & Tucci, M. 2006, *MNRAS*, 365, 891

Vikhlinin, A., et al. 2003, *ApJ*, 590, 15

Voevodkin, A. & Vikhlinin, A. 2004, *ApJ*, 601, 610

Wambsganss, J., Bode, P., & Ostriker, J. P. 2004, *ApJ*, 606, L93

Wetterich, C. 1988, *Nucl. Phys.*, B302, 668

Winitzki, S. & Kosowsky, A. 1998, *New Astronomy*, 3, 75

Wyithe, J. S. B. & Cen, R. 2006, ArXiv Astrophysics e-prints

Wyithe, J. S. B. & Loeb, A. 2003, *ApJ*, 588, L69

Zaldarriaga, M. & Seljak, U. 2000, ApJS, 129, 431

Zehavi, I., et al. 2005, ApJ, 630, 1

Zlatev, I., Wang, L., & Steinhardt, P. J. 1999, Physical Review Letters, 82, 896

A. SZ Marginalization and Priors

The analysis now includes marginalization over the amplitude of the SZ contribution, normalizing to the expected SZ C_l^{TT} spectrum predicted by Komatsu & Seljak (2002) for a model with $\Omega_m = 0.26$, $\Omega_b = 0.044$, $h = 0.72$, $n_s = 0.97$ and $\sigma_8 = 0.8$. We define the amplitude of the signal (relative to this model with A_{SZ}) and marginalize over this parameter with a flat prior, $0 < A_{SZ} < 2$. This range is based on the assumption that the Komatsu & Seljak (2002) (KS) approach estimates the SZ signal with an order unity uncertainty.

Numerical simulations (Nagai 2005) and analytical studies (Reid & Spergel 2006) find a tight correlation between mass and SZ signal, with the largest uncertainties associated with the cluster gas fraction. These results support the KS approach and suggest that the range of the prior is generous. Afshordi et al. (2005) analysis of the SZ signal from 116 nearby clusters in the WMAP data finds that the signal from nearby clusters is 30-40% weaker than expected. Since these nearby clusters are the dominant source of fluctuations in the WMAP angular power spectrum, this implies that $A_{SZ} < 1$.

We have also made a number of changes in the priors and the analysis techniques from the first year analysis. We are now using the amplitude of the angular power spectrum peak, C_{220} , rather than A as a parameter in the Markov Chain. This choice of prior leads to a slightly lower best fit amplitude.

Figure 27 shows how the change in priors and the SZ treatment alters our estimates of cosmological parameters. Except for changes σ_8 , the effects are all relatively small. We have estimated that roughly half of the change in the best fit σ_8 value is due to the change in the form of priors and half is due to the SZ marginalization. The spectral slope also has a weak dependence on A_{SZ} (see Figure 28).

When we are comparing results directly to the first year analysis, we use the same set of priors as used in the first year analysis (Table 2 and Figure 2). Otherwise, we use the approach outlined in §2.

In §7.3, the use of a flat prior on H_0 favors flat models over models with $\Omega_m = 1.3$ and $\Omega_\Lambda = 0$ as $dH/d\Omega_\Lambda$ decreases as Ω_Λ decreases. When WMAP is combined with other data sets, the prior choice is much less important.

B. Trispectrum methodology

B.1. Predicted Trispectrum Signal

We consider here a model that generates a non-trivial trispectrum, but no bispectrum signal. We assume that the gravitational potential Φ , is a product of two independent Gaussian fields, ϕ and ψ :

$$\Phi(\vec{x}) = \phi(\vec{x})[1 + g_{NL}\psi(\vec{x})] \quad (B1)$$

where g_{NL} characterizes the strength of the non-linear term.

Following Komatsu et al. (2005) approach for the bispectrum, extended recently to the trispectrum in Kogo & Komatsu (2006), the observed temperature multipoles are:

$$a_{\ell m} = b_\ell \int r^2 dr \Phi_{\ell m}(r) \alpha_\ell(r) + n_{\ell m} \quad (B2)$$

where b_ℓ is the beam, $n_{\ell m}$ is the noise and $\alpha_\ell(r)$ is the radiation transfer function:

$$\alpha_\ell(r) = \frac{2}{\pi} \int k^2 dk g_{T\ell}(k) j_\ell(kr) \quad (B3)$$

The non-linear coupling term generates a second order term:

$$a_{\ell m} = n_{\ell m} + b_\ell \int r^2 dr \alpha_\ell(r) \left[\phi_{\ell m}(r) + \phi_{\ell' m'}(r) \psi_{\ell'' m''}(r) C_{\ell m}^{\ell' m' \ell'' m''} \right] \quad (B4)$$

where

$$C_{\ell m}^{\ell' m' \ell'' m''} = \sqrt{\frac{4\pi}{(2\ell+1)(2\ell'+1)(2\ell''+1)}} \begin{pmatrix} \ell & \ell' & \ell'' \\ 0 & 0 & 0 \end{pmatrix} \begin{pmatrix} \ell & \ell' & \ell'' \\ m & m' & m'' \end{pmatrix}. \quad (B5)$$

This term does not have any effect on the bispectrum as $\langle \phi^3 \rangle = 0$ and $\langle \psi^3 \rangle = 0$. However, it does have a non-trivial effect on the trispectrum.

As with gravitational lensing (see Hu (2001)), the largest trispectrum term is the diagonal term, $T_{\ell\ell}^{\ell\ell}(0) = \langle C_\ell C_\ell \rangle - 3 \langle C_\ell \rangle^2$. This term would generate an excess in the χ^2 of

the fit of the model to the data:

$$T_{\ell\ell}^{\ell\ell}(0) = g_{NL}^2 C_\ell \int r^2 dr \int \tilde{r}^2 d\tilde{r} \alpha_\ell(r) \alpha_\ell(\tilde{r}) \sum_{m\ell'm'\ell''m''} \sum_{\tilde{\ell}'\tilde{m}'\tilde{\ell}''\tilde{m}''} \langle \phi_{\ell'm'}(r) \phi_{\tilde{\ell}'\tilde{m}'}(\tilde{r}) \rangle \langle \psi_{\ell''m''}(r) \psi_{\tilde{\ell}''\tilde{m}''}(\tilde{r}) \rangle C_{\ell m}^{\ell'm'\ell''m''} C_{\ell m}^{\tilde{\ell}'\tilde{m}'\tilde{\ell}''\tilde{m}''} \tilde{\mathbb{B}}_6''$$

We can then use

$$\langle \phi_{\ell'm'}(r) \phi_{\tilde{\ell}'\tilde{m}'}(\tilde{r}) \rangle = \delta_{\ell\tilde{\ell}'} \delta_{m'\tilde{m}'} \int k^2 dk P_\phi(k) j_{\ell'}(kr) j_{\ell'}(k\tilde{r}) \quad (B7)$$

and the equivalent relationship for ψ to rewrite the trispectrum as

$$T_{\ell\ell}^{\ell\ell}(0) = g_{NL}^2 \xi_\ell C_\ell^2 \quad (B8)$$

where

$$\xi_\ell = \frac{4\pi}{C_\ell} \int k^2 dk P_\phi(k) \int (k')^2 dk' P_\psi(k') \begin{pmatrix} \ell & \ell' & \ell'' \\ 0 & 0 & 0 \end{pmatrix}^2 \int r^2 dr \int \tilde{r}^2 d\tilde{r} \alpha_\ell(r) \alpha_\ell(\tilde{r}) j_{\ell'}(kr) j_{\ell''}(k'r) j_{\ell'}(k\tilde{r}) j_{\ell''}(k\tilde{r}). \quad (B9)$$

While this full integral is numerically intractable, we approximate the surface of last scatter as a thin screen so that

$$a_{\ell m} = b_\ell \Phi_{\ell m}(r_*) \alpha_\ell + n_{\ell m} \quad (B10)$$

then, the trispectrum coupling term reduces to

$$\xi_\ell = \frac{4\pi \alpha_\ell^2}{C_\ell} \int k^2 dk P_\phi(k) j_{\ell'}^2(kr_*) \int k'^2 dk' P_\psi(k') j_{\ell''}^2(k'r_*) \begin{pmatrix} \ell & \ell' & \ell'' \\ 0 & 0 & 0 \end{pmatrix}^2. \quad (B11)$$

Recall that in this limit,

$$C_\ell = \alpha_\ell^2 \int k^2 dk P_\phi(k) j_\ell^2(kr_*) \quad (B12)$$

Thus,

$$\xi_\ell = \frac{4\pi \alpha_\ell^2 C_{\ell'}}{\bar{\alpha}_{\ell'}^2 C_\ell} \int k'^2 dk' P_\psi(k') j_{\ell''}^2(k'r_*) \begin{pmatrix} \ell & \ell' & \ell'' \\ 0 & 0 & 0 \end{pmatrix}^2 \quad (B13)$$

The amplitude of ξ_ℓ is, thus, roughly the variance in the ψ field on the scale r_*/ℓ . Note that ξ_ℓ is a positive definite quantity so that $T_{\ell\ell}^{\ell\ell}(0)$ should be always positive.

B.2. Detecting the Non-Gaussian Signal

If we assume that ξ_ℓ is constant, then we can follow Hu (2001) and compute an optimal quadratic statistic. We approximate the optimal statistic as $\sum_i (T_i^f \nabla^2 T_i^f - N_i^2)^2$, where T^f is a smoothed map (e.g., a res 7 map) and we use the approximation that $C_\ell = A/\ell(\ell+1)$. This has the advantage that we can easily compute it and has well-defined noise properties.

B.2.1. Practical implementations

We define for this purpose the dimensionless \mathcal{G} statistic as

$$\begin{aligned} \mathcal{G} = & \sum_{p,b_1,b_2,b_3,b_4} w_{p,b_1} \hat{T}_{p,b_1} w_{p,b_2} \hat{T}_{p,b_2} w_{p,b_3} \hat{T}_{p,b_3} w_{p,b_4} \hat{T}_{p,b_4} \\ & - \sum_{b_1,b_2,b_3,b_4} \left(\sum_{p_1} w_{p_1,b_1} \hat{T}_{p_1,b_1} w_{p_1,b_2} \hat{T}_{p_1,b_2} \right) \left(\sum_{p_2} w_{p_2,b_1} \hat{T}_{p_2,b_1} w_{p_2,b_2} \hat{T}_{p_2,b_2} \right) \end{aligned} \quad (B14)$$

where b_i refers to various bands (Q, V, and W for yr1, yr2 and yr3) that are all distinct for a single term so that the noise bias is null for this statistic, w_{p,b_i} is a particular pixel weight (we will consider it equal unity first) and \hat{T}_b is a filtered map defined as

$$\hat{T}_{pb} = \frac{T_{pb}}{\sqrt{\sum_q T_{qb}^2}} \quad (B15)$$

$$T_{pb} = \sum_{\ell m} f_{\ell b} \tilde{a}_{\ell m b}^M Y_{\ell m}(\hat{\mathbf{n_p}}) \quad (B16)$$

where $\tilde{a}_{\ell m}^M$'s are the spherical harmonic coefficients of the masked sky. We use at this level the Kp12 mask to hide the brighter part of the galaxy (and potentially the brighter point sources) and ignore cut sky effects in considering those pseudo- $a_{\ell m}$ s. But when computing the sum over pixels in \mathcal{G} , we consider only pixels outside the Kp2 area. The obvious advantage of this simple real space statistic is its ability to handle inhomogeneous noise and to localize its various contributions in real space. The second term in the definition of \mathcal{G} aims at subtracting off the Gaussian unconnected part, so that if the \hat{T} fields are homogeneous Gaussian fields, we obtain $\langle \mathcal{G}^{ps} \rangle = 0$.

The exact nature of f_ℓ will depend on the source of the signal. For example, point sources do contribute to all n -points functions in real or harmonic space and are as such visible in the power spectrum, bispectrum and trispectrum. The first two have been used to set limits and corrections.

Should we want to isolate the point sources contribution with the \mathcal{G} statistic, we would proceed in the following manner. The point sources power spectrum is well approximated by a constant, white noise like, power spectrum C_ℓ^{ps} (see Komatsu et al. (2003)). Given the measured power spectrum, $\tilde{C}_\ell = C_\ell b_\ell^2 + C_\ell^{ps} b_\ell^2 + N_\ell$, the Wiener like filter to reconstruct point sources is to $f_\ell^{ps} = b_\ell^2 / \tilde{C}_\ell$. Note that this filter would be optimal only if point sources were drawn from a Gaussian distribution, which is not true. We can however expect it to be close to optimal.

In order to constrain the CMB contribution to the trispectrum and constrain g_{NL} close to optimality, we will set $f_{\ell 1}$ and $f_{\ell 2}$ to the Wiener filter for the CMB field, $f_{\ell 1} = f_{\ell 3} = C_\ell^{theory} b_\ell^2 / C_\ell^{measured}$ and $f_{\ell 2} = f_{\ell 4} = \ell(\ell+1)f_{\ell 1}$, where C_ℓ^{theory} is the best fit model angular power spectrum and $C_\ell^{measured}$ is the measured raw power spectrum including the signal and the noise and not corrected for the beam window function.

We restrict ourselves to a unit weighting which is nearly optimal in the signal dominated regime where we draw our conclusions from, *i.e.* at resolution lower than 6.

B.2.2. Explicit relation to the trispectrum

Ignoring the weights, it is easy to show using the relation recalled in the next section that

$$\langle T_1(\hat{\mathbf{n}}) T_2(\hat{\mathbf{n}}) T_3(\hat{\mathbf{n}}) T_4(\hat{\mathbf{n}}) \rangle_c = \sum_p T_{1p} T_{2p} T_{3p} T_{4p} \quad (B17)$$

$$= \sum_{\ell_1 m_1 \ell_2 m_2 \ell_3 m_3 \ell_4 m_4} \langle t_{\ell_1 m_1} t_{\ell_2 m_2} t_{\ell_3 m_3}^* t_{\ell_4 m_4}^* \rangle_c \int d\Omega(\hat{\mathbf{n}}) Y_{\ell_1 m_1}(\hat{\mathbf{n}}) Y_{\ell_2 m_2}(\hat{\mathbf{n}}) Y_{\ell_3 m_3}^*(\hat{\mathbf{n}}) Y_{\ell_4 m_4}^*(\hat{\mathbf{n}}) \quad (B18)$$

$$= \sum_{\ell_1 m_1 \ell_2 m_2 \ell_3 m_3 \ell_4 m_4 LM} \sqrt{\frac{(2\ell_1+1)(2\ell_2+1)}{4\pi(2L+1)}} \sqrt{\frac{(2\ell_3+1)(2\ell_4+1)}{4\pi(2L+1)}} C_{\ell_1 0 \ell_2 0}^{L0} C_{\ell_3 0 \ell_4 0}^{L0} C_{\ell_1 m_1 \ell_2 m_2}^{LM} C_{\ell_3 m_3 \ell_4 m_4}^{LM} \times \langle t_{\ell_1 m_1} t_{\ell_2 m_2} t_{\ell_3 m_3}^* t_{\ell_4 m_4}^* \rangle_c. \quad (B19)$$

It is then easy to relate to standard expression for the connected part of the trispectrum as in Hu (2001) and Komatsu (2001).

C. Computing the likelihood of a modulated Gaussian field

To recall the previous notations, we write the temperature modulated field as

$$\tilde{T}(\hat{\mathbf{n}}) = T(\hat{\mathbf{n}}) [1 + f(\hat{\mathbf{n}})] \quad (\text{C1})$$

where $T(\hat{\mathbf{n}})$ is a statistically isotropic random Gaussian field whose angular power spectrum we note C_ℓ , while $f(\hat{\mathbf{n}})$ is some arbitrary mathematical function. Therefore, $\tilde{T}(\hat{\mathbf{n}})$ is still a Gaussian field but whose statistical isotropy is violated. f is an arbitrary function that we expand in spherical harmonic

$$f(\hat{\mathbf{n}}) = \sum_{\ell=1}^{\ell_{\max}} \sum_{m=-m}^m f_{\ell m} Y_{\ell m}(\hat{\mathbf{n}}). \quad (\text{C2})$$

The covariance matrix of the observed \tilde{T} fields is

$$\tilde{\mathcal{C}}(\hat{\mathbf{n}}, \hat{\mathbf{m}}) \equiv [1 + f(\hat{\mathbf{n}})] \mathcal{C}(\hat{\mathbf{n}}, \hat{\mathbf{m}}) [1 + f(\hat{\mathbf{m}})] \quad (\text{C3})$$

where C is the covariance matrix of the isotropic field T :

$$\mathcal{C}(\hat{\mathbf{n}}, \hat{\mathbf{m}}) = \sum_{\ell} \frac{2\ell + 1}{4\pi} C_{\ell} P_{\ell}(\hat{\mathbf{n}} \cdot \hat{\mathbf{m}}). \quad (\text{C4})$$

The likelihood function of $\tilde{T}(\hat{\mathbf{n}})$ given C_ℓ 's and $f_{\ell m}$'s can then be written as follows:

$$\mathcal{L}(\tilde{T} | f_{\ell m}, C_{\ell}) \propto \frac{1}{\sqrt{\det \tilde{\mathcal{C}}}} \exp \left[-\frac{1}{2} \frac{\tilde{T}(\hat{\mathbf{n}})}{1 + f(\hat{\mathbf{n}})} \mathcal{C}^{-1}(\hat{\mathbf{n}}, \hat{\mathbf{m}}) \frac{\tilde{T}(\hat{\mathbf{m}})}{1 + f(\hat{\mathbf{m}})} \right], \quad (\text{C5})$$

where N is the number of pixels considered and

$$\det \tilde{\mathcal{C}} = \det \mathcal{C} \left(\prod_{i=1}^N (1 + f(\hat{\mathbf{n}}_i)) \right)^2. \quad (\text{C6})$$

In practice, we compute $\ln \mathcal{L}$ exactly at $\text{res} 3$ ($N_{\text{side}} = 8$) restricting ourselves to pixels outside the Kp2 region. We checked that it was equivalent to marginalizing over the non-observed pixels. The degradation and masking are performed as described in the appendix of Hinshaw et al. (2006). In solving for the maximum likelihood with a MCMC solver, we fix the C_ℓ 's for ℓ greater than 10 to their ML values obtained in Hinshaw et al. (2006) and vary simultaneously $C_{\ell=0, \dots, 10}$ and the $f_{\ell m}$ imposing the reality condition, $f_{\ell m}^* = f_{\ell - m}$.

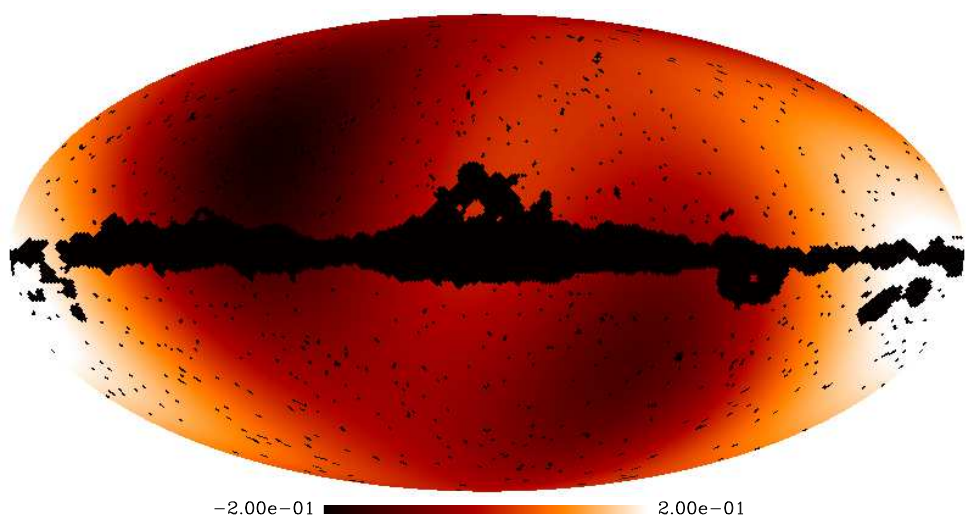


Fig. 26.— The best-fit large-scale field modulating the temperature fluctuations, $f(\hat{n})$ for $l_{max} = 2$.

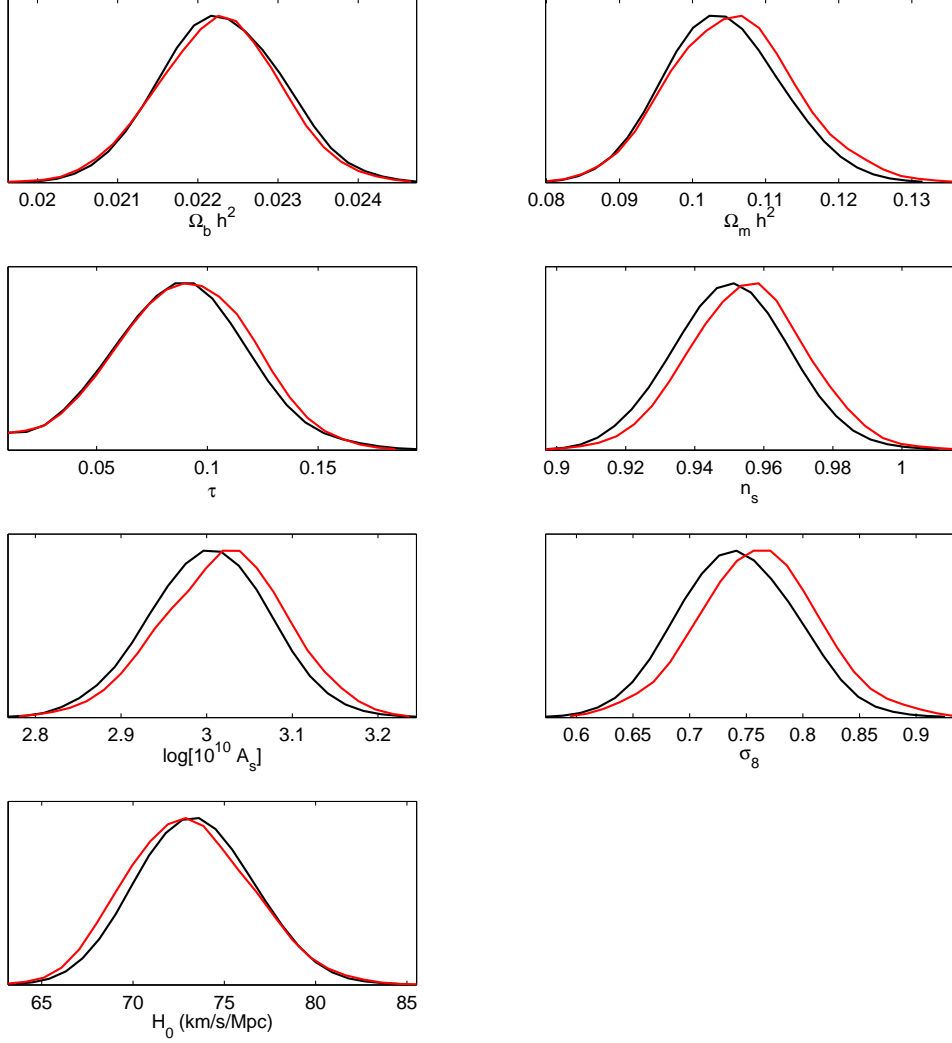


Fig. 27.— The effect of SZ marginalization on the likelihood function. The red curve is the likelihood surface for the three-year WMAP data for the power-law Λ CDM model with $A_{SZ} = 0$. The black curve is the likelihood surface after marginalizing over the amplitude of the SZ contribution.

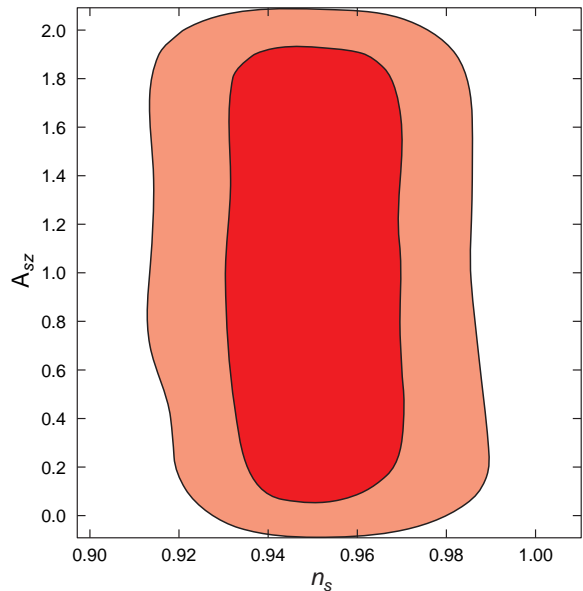


Fig. 28.— The likelihood surface for (n, A_{SZ}) for the power-law Λ CDM model and WMAP data.